Lamont et al.
Thermal evolution of Naxos, Greece, from the timing of high-pressure metamorphism
Roberts[ID]https://orcid.org/ 0000-0001-8272-5432
†thomas.lamont@bristol.ac.uk
GSA Bulletin; Month/Month 2022; v. 134; no. X/X; p. 000–000;
https://doi.org/10.1130/B36332.1; 14 figures; 1 tables; 2 supplemental file.
[1]Supplemental Material. Further method details of U–(Th)–Pb geochronology and thermal modelling and complete U–(Th)–Pb analyses. Please visit https://doi.org/10.1130/GSAB.S.XXXX to access the supplemental material, and contact editing@geosociety.org with any questions.
SCIENCE EDITOR: ROB STRACHAN
ASSOCIATE EDITOR: KATHRYN CUTTS
MANUSCRIPT RECEIVED 11 SEPTEMBER 2021
REVISED MANUSCRIPT RECEIVED 30 MAY 2022
MANUSCRIPT ACCEPTED ___ MONTH 2022
Printed in the USA

Constraints on the thermal evolution of metamorphic core complexes from the timing of high-pressure metamorphism on Naxos, Greece

Thomas N Lamont[1,2,5*,†], Andrew J Smye[3], Nick M W Roberts[4], Michael P Searle[2], David J Waters[2], and Richard W White[1]

1. School of Earth and Environmental Sciences, University of St Andrews, St Andrews, KY169AL, UK
2. Department Earth Sciences, University of Oxford, South Parks Road, Oxford, OX1 3AN, UK
3. Department of Geosciences, The Pennsylvania State University, University Park, PA 16802, USA
4. Geochronology and Tracers Facility, British Geological Survey, Environmental Science Centre, Nottingham, NG12 5GG, UK
5. Now at: School of Earth Sciences, University of Bristol, Wills Memorial Building, Queens Road, Bristol, BS8 1RJ, UK.

ABSTRACT

Metamorphic core complexes (MCCs) are classically interpreted to form during crustal extension, although many also occur in compressional environments. New U–(Th)–Pb allanite and xenotime geochronology from the structurally highest Zas Unit (Cycladic Blueschist Unit) of the Naxos MCC, Greece, integrated with pressure–temperature–time (*P*–*T*–*t*) histories are incorporated into a thermal model to test the role of crustal thickening and extension in forming MCCs. Metamorphism on Naxos is diachronous, with peak metamorphic conditions propagating down structural section over a ~30–35 Myr period, from ca. 50–15 Ma. The Zas Unit at the highest structural level records blueschist facies metamorphism (~14.5–19 kbar, 470–570 °C) at ca. 50 Ma, during northeast-directed subduction of the Adriatic continental margin. The Zas Unit was subsequently extruded toward the SW and thrust over more proximal continental margin and basement rocks (Koronos, Core Units). This contractional episode resulted in crustal thickening and Barrovian metamorphism from ca. 40 Ma and reached peak kyanite-sillimanite grade conditions of ~10–5 kbar and 600–730 °C at 20–15 Ma. Model *P*–*T*–*t* paths assuming conductive

relaxation of isotherms following overthrusting are consistent with the clockwise *P–T–t* evolution. In contrast, extension results in exhumation and cooling of the crust, inconsistent with key components of the thermal evolution. Barrovian metamorphism on Naxos is therefore interpreted to result from crustal thickening over a ~30–35 Myr time-period prior to extension, normal faulting, and rapid exhumation after a thermal climax at ca. 15 Ma.

1. INTRODUCTION

Profound uncertainty remains over the heat sources and transfer mechanisms responsible for the characteristic Barrovian metamorphism observed globally in metamorphic core complexes (MCCs; Platt et al., 2015) (Fig. 1). Metamorphic core complexes have classically been regarded to form in extensional tectonic settings, including the Basin and Range Province (Coney, 1980; Wernicke, 1981, 1985; Armstrong, 1982; Fletcher and Hallet, 1983; Buck, 1988, Yin, 1991, Teyssier and Whitney, 2002) and the Aegean Sea (Lister et al., 1984; Kruckenberg et al., 2011; Platt et al., 2015; Rey et al., 2017), due to increased basal heating of the crust in response to lithospheric thinning (Fig. 1a). However, numerous MCCs have also been identified in collisional settings associated with crustal thickening, such as the North Himalayan gneiss domes (e.g., Burg et al., 1984; Lee et al., 2000, 2004, 2006; Searle and Lamont, 2020; Fig. 1b), creating a paradox to the classical MCC model and the sources of heat responsible for metamorphism.

Insight into the sources of heating and therefore discrimination of MCC models can be gleaned by considering pressure-temperature-time (*P–T–t*) paths from crust undergoing extension versus thickening. Pure shear, uniform (with depth) lithospheric extension increases the crustal geotherm at the rate of conductive heat loss due to exhumation of rock at all crustal levels (e.g., Ruppel et al., 1988). This does not cause any net-heating of rock, but rather cooling of rock or delayed cooling during exhumation, depending on the magnitudes and rates of extension. Depth-dependent extension with small magnitudes of crustal extension (β) and large degrees of mantle extension (γ) results in deep crustal heating (e.g, Royden and Keen, 1980; Royden, 1996). Depth-dependent extension has been proposed to cause granulite facies metamorphism due to increased asthenosphere heating, and maybe associated with crustal and/or mantle melting assuming low exhumation rates (Wells, 1980; Sandiford and Powell 1986; Bohlen, 1987; Ruppel et al., 1988; Waters, 1990; Smye et al., 2019). Despite this, crustal extension cannot explain the burial history of rock or clockwise prograde *P–T–t* paths associated with kyanite-grade metamorphism recorded in some MCCs which require compression and crustal thickening (Searle and Lamont, 2020). During crustal thickening, an elevated geotherm develops due to the conductive relaxation of isotherms and an increase in crustal radiogenic heat production. Progressive overthrusting causes diachronous attainment of peak metamorphic conditions as rocks are buried, heated, and later exhumed over a ca. 30–50 Myr cycle. This results in the highest-grade and youngest metamorphic rocks at the deepest structural levels, whereas rocks that attained their peak metamorphic conditions earlier in the orogenic history are preserved at structurally higher levels (Bickle et al., 1975; England and Richardson, 1977; England and Thompson, 1984; Jamieson and Beaumont, 1998, 2013). Nevertheless, in some regional metamorphic terranes, geochronology has shown there to be a disparity between predicted timescales of heating and observed thermal length scales, which necessitates additional mechanisms on top of conductive heating from overthrusting (Ague and Baxter, 2007; Baxter et al., 2002; Smye et al., 2011). These include: (i) increased radiogenic heat production (Huerta et al., 1999; Jamieson et al., 1998), (ii) shear heating (Molnar and England, 1990), (iii) magmatism (Lyubetskaya and Ague, 2010), (iv) advective transport of heat by fluids (Bickle and McKenzie, 1987), (v) tectonic advection of heat (Burg and Gerya, 2005; Smye et al., 2011; Grujic et al., 1996; Whittington et al., 2009), and (vi) elevated mantle heat flow due to lithospheric extension/removal (Oxburgh and Turcotte, 1974; Bird, 1979; Stüwe and Sandiford, 1995; Ryan and Dewey, 2019).

The Naxos MCC at the center of the Attico Cycladic Massif (ACM), Greece, provides an opportunity to investigate the thermal consequences of crustal thickening and extension. This is because Naxos has been regarded an archetypal example of an MCC formed during Cenozoic extension of the ACM (Lister et al., 1984; Buick, 1991a,b; Urai et al., 1990, John and Howard, 1995, Jolivet et al., 2010; Kruckenberg et al., 2011). The island comprises tectonic components that are common to MCCs: a high-grade metamorphic footwall including a migmatite dome, separated from a non-metamorphosed hanging-wall by a NE-dipping low angle brittle-ductile normal fault, the Naxos-Paros Detachment System (NPDS) (Buick, 1991b; Cao et al., 2013, 2017, Lamont et al., 2019). Recently however, Lamont et al., (2019) and Searle and Lamont, (2020, 2022) favored a compressional MCC model and presented evidence for contrasting clockwise *P–T* histories from all structural levels on Naxos explained by thrusting and imbrication of different tectono-stratigraphic nappes that experienced contrasting thermal histories, and argued that the MCC preserves many features similar to the Tauern Window in the Austrian Alps (Smye et al., 2011), a classic overthrust terrane.

In this contribution we provide the first U–(Th)–Pb allanite and xenotime ages from Naxos that directly constrain the timing of high-pressure low-temperature (*HP–LT*) metamorphism (M_1), and overthrusting of the Cycladic Blueschist Unit (CBU). We then show that the predicted timescale and magnitude of Barrovian heating to reach a thermal climax (M_2–M_3) at the deepest levels of the MCC is consistent with predictions from simple thermal overthrust models, critically, without the requirement for asthenospheric mantle heat input from depth-dependent extension.

2. GEOLOGY AND GEOCHRONOLOGY OF NAXOS

The Naxos MCC belongs to the ACM, located in a back-arc position to the north of the Hellenic subduction zone (Fig. 2). Although lithospheric extension has undoubtedly affected the ACM since ca. 10 Ma, the timing of when extension started remains debated. The classic geodynamic framework of the ACM involves an Eocene *HP–LT* metamorphic event (M_1) affecting the CBU in a subduction setting, followed by extension commencing during the Oligocene to early Miocene (30–20 Ma) due to roll-back of the Hellenic subduction zone. Asthenospheric heating associated with ACM extension has been classically interpreted to have caused Barrovian metamorphism (M_2–M_3) and to have formed a series of MCCs and low angle normal faults (North Cycladic Detachment System (NCDS) - the Naxos-Paros Detachment System (NPDS) and the West Cycladic Detachment System (WCDS)) (Figs. 2–3; Lister et al., 1984; Jolivet and Brun, 2010; Jolivet et al., 2004, 2010; Graseman et al., 2012; Menant et al., 2013). In contrast, or in addition to slab rollback, we note that it is possible that Aegean extension arises from gradients of gravitational potential energy arising from variations in crustal thickness; England et al., (2016) indicate that the tractions applied to the base of the lithosphere due to slab rollback are insignificant compared to stresses induced due to gravity.

Despite extension affecting all structural levels, the Naxos MCC reveals the most complete cross section through the ACM, (Dürr et al., 1978). The island exposes a sequence of stacked nappes, each with distinct tectono-metamorphic histories that document an entire mountain building cycle (the ‘Aegean Orogeny’) spanning between ca. 75–15 Ma (Lamont et al., 2019; Searle and Lamont, 2020; Jansen and Schuiling, 1976; Papanikolaou, 1984) associated with the collision of Greater Adria with Eurasia (Van Hinsbergen et al., 2020). This suggests the MCC has a compressional origin and represents a tectonic window into the thermal evolution of the Aegean Orogeny. With increasing structural depth these nappes and structures include: (1) the Upper Cycladic Nappe representing the hangingwall of the MCC. This is structurally underlaid by (2) the Naxos Paros Detachment (NPDS), which separates it from the metamorphic footwall. Structurally beneath the NPDS, the metamorphic footwall comprises (3) The Zas Unit at high structural levels, which represents retrogressed (M_1) blueschist-facies rocks that are partially overprinted by greenschist-facies assemblages related to the (M_2) Barrovian metamorphic event. This is structurally underlaid by (4) The Koronos and Core Units that expose upper amphibolite-facies Barrovian (M_2) kyanite grade gneisses (Koronos Unit) at intermediate structural levels and (M_3) sillimanite grade gneisses and migmatites (M_3) at the deepest structural levels. Due to this complicated polymetamorphic and deformation history, there are several competing interpretations to the Naxos MCCs evolution, which are discussed and evaluated below.

2.1 Upper Cycladic Nappe

The Upper Cycladic Nappe represents the hangingwall of the MCC (Fig. 3) and comprises the upper plate of the Aegean Orogenic belt. It includes a highly dismembered ophiolite sequence (Stouraiti et al., 2017), which could potentially be comparable to the Tsiknias Ophiolite exposed on Tinos (which formed at ca. 162 Ma, and was obducted at ca. 74 Ma; Lamont et al., 2020a; Katzir et al., 1996; Fig. 4b), as well as pelagic sediments and limestones that are deformed into a mélange, possibly during ophiolite emplacement (Lamont et al., 2019). These highly deformed rocks are unconformably overlaid by Miocene-Pleistocene continental sediments and conglomerates, that have been tilted away from the MCC (Kuhlemann et al., 2004; Lamont et al., 2019).

2.2 The Naxos-Paros Detachment

The Naxos-Paros Detachment System (NPDS) is a NNE-dipping low angle normal fault that separates the Upper Cycladic Nappe from the metamorphic footwall (Lister et al., 1984; Buick, 1991b; Urai et al., 1990; John and Howard, 1995; Fig. 3). Top-to-NNE shearing on the NPDS cuts and telescopes all earlier tectono-metamorphic features within the underlying MCC footwall, producing an apparent field gradient of ~700 °C·km^{-1} on the island's western coastline (Lamont et al., 2019). The NPDS is folded around Naxos (Figs. 2–3), suggesting orthogonal E–W shortening occurred coeval with, or following NNE–SSW extension (Fig. 2; Lamont et al., 2019; Virgo et al., 2018 Koukouvelas, and Kokkalas, 2003). An I-type granodiorite pluton dated at 12.2 Ma (Keay et al., 2001) intrudes the western part of the MCC and is cut by the NPDS, placing a ca. 12 Ma upper bound on extensional deformation. K–Ar thermochronology on fault gauges of the NPDS yield ages of 10.3–9.0 Ma (Mancktelow et al., 2016), whereas apatite fission track ages of 11.0–9.0 Ma (Seward et al., 2009) suggest exhumation of the MCC was well under way by the Late-Miocene.

2.3 Zas Unit

The Zas Unit is exposed at the highest structural levels of the MCC footwall in east and south-east Naxos and is considered part of the CBU (Lamont et al., 2019; Peillod et al., 2017; Fig. 3). It comprises dolomitic and calcite marbles, metavolcanics, conglomerates and distal marine metasediments associated with the rare occurrence of piemontite. The Zas Unit and wider CBU are interpreted to represent the leading edge of the Adriatic continental margin that experienced (M_1) blueschist-facies conditions during attempted NE-directed subduction at *P–T* conditions of ca. 14.5–19 kbar 470–570 °C on Naxos (Figs. 3–4a; Avigad, 1998; Lamont et al., 2019; Peillod et al., 2017, 2021a). This was followed by M_2 greenschist facies retrogression at ca. 4–6 kbar and 400 °C (Peillod et al., 2017; Lamont et al., 2019). Pervasive top-to-NE blueschist-facies 'extensional' shear fabrics (S_1) occur throughout the Zas Unit/CBU and are interpreted to have formed along a passive roof shear zone during SW-directed extrusion of rock from a NE dipping subduction zone. Most interpretations relate extrusion to the positive buoyancy contrast of continental crust compared to mantle, allowing return ductile flow of continental crust in a subduction channel or wedge, prior to being overthrusted toward the SW onto the proximal and less deeply buried Adriatic continental margin and Variscan Basement (Laurent et al., 2016; Peillod et al., 2017; Lamont et al., 2019; Lamont et al., 2020b; Baziotis et al., 2020; Searle and Lamont 2022). This extrusion/overthrust interpretation is supported by the presence of the South Cycladic Thrust that bounds the base of the CBU on Ios (Fig. 2; Huet et al., 2009), and also several SW verging thrusts on Tinos and Syros (Lamont et al., 2020b; Philippon et al., 2011). Beneath the South Cycladic Thrust, metasedimentary and Variscan basement footwall rocks on Ios, and also structurally deeper levels of Naxos (Koronos and Core Units) beyond the biotite in and chloritoid out isograd (Jansen, 1973; Jansen and Schuiling, 1976), do not record petrological features indicative of the *HP* (M_1) event (Fig. 4; Lamont et al., 2019; Peillod et al., 2017). This potentially suggests the structurally deeper M_2 amphibolite-facies rocks and basement were not buried as deeply in Cycladic subduction/accretion complex, and belong to the footwall beneath the overthrusted CBU *HP* nappe. This debate is discussed in detail below.

Despite several detailed Rb–Sr, $^{40}Ar–^{39}Ar$ and K–Ar geochronological studies, the timing of peak *HP* (M_1) conditions at structurally high levels on Naxos remains problematic. White mica Rb–Sr dating on *HP* rocks from SE Naxos by Peillod et al., (2017) yielded dates of 40.5 ± 1.0 Ma and 38.3 ± 0.5 Ma, which were interpreted to constrain blueschist-facies deformation, and ongoing dehydration at or close to peak *HP* (M_1) conditions respectively. However, the uncertainty on these dates only just overlaps with the lower bound of the ca. 50–42 Ma $^{40}Ar–^{39}Ar$ and K–Ar white mica age spectrum, with a single $^{40}Ar–^{39}Ar$ amphibole age of 56 Ma (Altherr, 1979; Andriessen et al., 1987; Wijbrans and McDougall, 1986, 1988), interpreted to broadly constrain M_1. However, Wijbrans and McDougall, (1988) acknowledge partial resetting of the K–Ar system has occurred, and this, combined with the low closure temperature for argon in phengites, lead them to interpret the oldest $^{40}Ar–^{39}Ar$ and K–Ar dates (ca. 50 Ma) as representing a minimum age for peak *HP* (M_1) conditions on Naxos and the younger tail (ca. <44 Ma) as representing cooling and retrogression while potentially still under blueschist-facies conditions (Wijbrans and McDougall, 1988). Additionally, the Rb–Sr white mica dates from Naxos are not consistent with the timing of 'peak' blueschist-eclogite facies dates from the CBU on other islands (Syros, Tinos, Sifnos) which span ca. 53–45 Ma, determined by Lu–Hf and Sm–Nd garnet, U–Pb zircon, and the upper range of K–Ar, $^{40}Ar–^{39}Ar$ and Rb–Sr geochronology (e.g., Lagos et al., 2007; Tomaschek et al., 2003; Bulle et al., 2010; Dragovic et al. 2012; Cliff et al., 2017; Gorce et al., 2021). Based on Rb–Sr from Syros, this 'peak' *HP* metamorphism (M_1) was followed by retrogression from the blueschist-facies between ca. 42–30 Ma (Cliff et al., 2017). On Naxos, greenschist-facies retrogression (M_2) is dated between ca. 32–27 Ma by Rb–Sr on white mica (Peillod et al., 2017), although $^{40}Ar–^{39}Ar$ and K–Ar data suggest the M_2 retrograde overprint is younger than ca. 27–20 Ma (Wijbrans and McDougall, 1988). This uncertainty in the timing of peak M_1 conditions and the longevity of the M_2 event at high structural levels on Naxos (Zas Unit) is a key issue we aim to address in this study.

At intermediate structural levels of the MCC, Lamont et al., (2019) mapped the Zas Shear Zone (ZSZ; Fig. 3), a greenschist-facies structure associated with top-to-NNE kinematics that closely corresponds with the biotite-in and chloritoid-out isograds (Jansen, 1973). They proposed this structure represents a major metamorphic discontinuity which separates the retrogressed *HP* (M_1) blueschist-facies rocks of the Zas Unit from the underlying (M_2) amphibolite-facies Barrovian rocks of the Koronos and Core Units. Peillod et al., (2021b) questioned this interpretation, and argued the ZSZ was not associated with significant displacements as similar lithologies occur on both sides of the shear zone, and interpreted the Eocene (ca. 40 Ma) U–Pb zircon rim dates reported from the structurally deeper footwall rocks (Koronos Unit; Martin et al., 2006; Bolhar et al., 2017), as evidence that the deeper levels of the MCC also experienced *HP* metamorphism (M_1) (Fig. 8a). However, it is unclear what these Eocene zircon rim dates represent as they have not been demonstrably linked to a specific *P–T* stage.

Irrespective of whatever the Eocene U–Pb dates represent, Lamont et al., (2019) noted several key observations that suggest ZSZ was responsible for the juxtaposition of two distinct tectono-metamorphic units originally sitting at very different crustal levels at the time of the M_2 event: (1) highly penetrative greenschist-facies top-to-NNE shearing (S_3) on the structure suggesting high strains; (2) a complete lack of (M_1) *HP* relict assemblages in the structurally deeper levels of the MCC; (3) a sharp decrease in metamorphic grade and calculated Barrovian (M_2) pressures and temperatures across the structure, which correspond to the sharp decrease in M_2 Barrovian isograds that are aligned parallel with top-to-NNE (S_3) shear fabrics, with a drop off length-scale in metamorphic grade from the second sillimanite isograd (>700 ºC) to the biotite out isograd (<450 ºC) over a structural depth of ~4 km on the eastern side of the MCC (Fig. 3), an order of magnitude less than the thermal length-scales predicted by conductive heating (England and Richardson, 1977; England and Thompson, 1984); and (4) contrasting $^{40}Ar–^{39}Ar$ and K–Ar cooling ages of rocks across the structure (Wijbrans and McDougall, 1988), suggesting the retrogressed blueschists in the hangingwall remained at a much higher crustal level to not be overprinted during M_2. Lamont et al., (2019) rectified these observations by interpreting the ZSZ to be a passive roof normal fault (Means, 1989) responsible for the juxtaposition of two very different crustal levels during the end of the Barrovian event (M_2–M_3). To explain the early *HP* (M_1) history and incomplete Barrovian (M_2) overprint of rocks in the hangingwall of the structure (Zas Unit), Lamont et al., (2019) argued that the Zas Unit was extruded from the subduction zone and emplaced at much shallower crustal depths compared to the underlying ca. 10 kbar amphibolite-facies (M_2) kyanite-sillimanite grade rocks (Fig. 8b). Lamont et al., also argue the ZSZ cuts out or overprints the South Cycladic Thrust or the thrust defining the base of the CBU to explain the difference in metamorphic histories. We believe these thermal and microstructural arguments, suggest that the ZSZ is an important structure that telescoped the Barrovian isograds, and that this shearing must pre-date the NPDS that cuts the ZSZ and the metamorphic stratigraphy in west Naxos (Figs. 3–4). We therefore interpret the Naxos MCC to not represent a single coherent package of rocks, but a sequence of rocks that were located at different crustal levels during the M_2–M_3 event that and have been tectonically juxtaposed during exhumation.

2.4 Koronos Unit and Core Units

The Koronos and Core Units (Fig. 3) are exposed structurally beneath the ZSZ at intermediate and deep levels of the MCC, respectively. These units represent the proximal shelf sediments and basement of the Adriatic continental margin and experienced kyanite-grade Barrovian metamorphism (M_2) that involved a clockwise prograde *P–T* loop (Lamont et al., 2019), involving burial from ca. 6 kbar and 550 °C to 10 kbar and 600–730 °C (M_2). At the deepest levels, (M_2) kyanite grade rocks experienced water saturated melting, isothermal decompression and muscovite dehydration melting at sillimanite-grade conditions (M_3) of ca. 5–6 kbar and 700–730 °C (Fig. 4a; Lamont et al., 2019). Migmatites, leucogranites, and meta-sediments are intercalated with overthrusted and structurally repeated slices of Variscan granite basement and are reworked into a migmatite dome and second order sub-domes (Fig. 3; Kruckenberg et al., 2010, 2011; Vanderhaeghe, 2004, Vanderhaeghe and Teyssier, 2001).

The Koronos Shear Zone (KSZ) separates the Koronos Unit from the underlying Core Unit and displays top-to-NNE kinematics (Fig. 3). The KSZ wraps around the Core Unit, which comprises a 4 km wide by 8 km long migmatite dome, that is also highly controversial. A combination of buoyancy driven, and isostasy driven flow of lower crustal inflowing migmatites during crustal extension has been proposed to form the dome and contractional features within it (Kruckenberg et al., 2011; Rey et al., 2009, 2011, 2017). This extensional MCC/migmatite dome model predicts divergent radial shear senses along the dome margins due to decoupling of the rheologically weaker inflowing migmatites below an extending upper crust. However, this model is inconsistent with the overall low melt fractions within the migmatites and Variscan granite basement (Lamont et al., 2019), unidirectional top-to-NNE shear on all dome margins, and that upright NNE–SSW trending isoclinal folding is continuous across the KSZ and ZSZ (Lamont et al., 2019). These observations suggest the KSZ and ZSZ are associated with unidirectional NNE–SSW directed ductile flow, and that the structurally deeper migmatite dome was not decoupled from the overlying units (Koronos and Zas Units) at the time of upright folding and doming. At the center of the migmatite dome, kyanite and sillimanite grade assemblages are deformed by NNE–SSW and E–W trending upright isoclinal folds that are subsequently affected by vertical boudinage associated with a constrictional stress field. These upright folds and vertical boudinage are overprinted by horizontal NNE–SSW boudinage, suggesting a switch from compressional to extensional stresses during the M_3 event as the migmatite dome formed (Lamont et al., 2019; Virgo et al., 2018; Von Hagke et al., 2018). Top-to-NNE shear fabrics on the KSZ and ZSZ are folded about the migmatite dome (Core Unit), and are cross-cut by leucogranites, suggesting that top-to-NNE shearing on the KSZ pre-dates migmatite doming and muscovite-dehydration melting. These deeper MCC structures are also cut by the NPDS (the low angle normal fault responsible for final exhumation of the MCC) (Fig. 3), particularly on the western side of the island. Such cross-cutting relationships indicate that the KSZ and ZSZ pre-date migmatite doming, regional extension and final exhumation of the MCC. Lamont et al., (2019) proposed that the KSZ and ZSZ represent passive roof ductile shear zones (Means et al., 1989) bounding the top of a SW-directed syn-orogenic extruding ductile wedge of migmatites and gneisses that accommodated exhumation of the deepest levels of the MCC from ~35–17 km depth, where they were juxtaposed against the retrograde *HP* rocks sitting at much shallower crustal depths (Zas Unit), in many ways comparable to the ‘extensional’ S–C’ fabrics observed on South Tibetan Detachment that bounds the top of the Greater Himalayan Sequence (Searle, 2010).

U–Pb zircon geochronology show that migmatites and gneisses experienced a thermal climax between ca. 24–15 Ma (Vanderhaeghe et al., 2018) with partial melting occurring between 20.7 and 16.8 Ma (Keay et al., 2001). Ring et al. (2018) presented Rb–Sr ages spanning ca. 14.3–11 Ma and interpreted these dates to represent cooling and recrystallization of migmatites and leucogranites. At the top of the Koronos Unit, immediately beneath the ZSZ, Rb–Sr dates span from 29.3 to 5.2 Ma (Duchêne et al., 2006), consistent with ^{40}Ar–^{39}Ar dates

~30–20 Ma at a similar structural level beyond the biotite-in and chloritoid-out isograds (Wijbrans and McDougall, 1986), suggesting that Barrovian metamorphism was protracted and propagated down structural level with time.

U–Pb zircon dating of the Koronos Unit by Martin et al., (2006), show metamorphic zircon growth stages at ca. 69–40 Ma and 19–16 Ma, whereas Bolhar et al., (2017) report zircon growth at ca. 700–550 Ma (extending to 2046 Ma), ca. 262–220 Ma, ca. 47–38 Ma and ca. 15–14 Ma (Fig. 4), with most Eocene zircon rims clustering around ca. 40 Ma. The interpretation of these Eocene dates is highly contentious, as it is unclear whether the Koronos/Core units experienced an early M_1 *HP* history. This is because there is no documented petrological evidence in the mineralogy, microstructures, or mineral chemistry that indicate these rocks experienced the M_1 event.

Furthermore, Bolhar et al., (2017) cannot decipher if the zircon grew in situ or represent xenocrystic cores, whereas Martin et al., (2006) show the Eocene zircon rims have similar $\delta^{18}O$ composition as a garnet rim (ca. 11 ‰) in a calcsilicate and a garnet core (ca. 14 ‰) in a metapelite, indicating Eocene zircon grew in equilibrium with garnet. However, no rigorous thermobarometric calculations were provided to link these zircon dates to a specific *P–T* stage associated with garnet growth. Despite this, both studies still interpret the zircon rims to constrain the *HP* M_1 event at intermediate to deep levels of the MCC (Koronos Unit; Martin et al., 2006; Bolhar et al., 2017; Peillod et al. 2017; 2021a,b). This interpretation is largely based on the overlapping distribution of M_1 dates elsewhere in the CBU, and the assumption that the rocks on Naxos are a homogeneous package; the authors therefore extrapolate the *HP* rocks exposed at structurally high levels of Naxos (Zas Unit) to deeper levels of the MCC (Martin et al., 2006; Figure 3. P. 179), as was originally proposed by Avigad, (1998). However, the complete lack of petrographic or thermobarometric evidence for *HP* metamorphism at intermediate and deep levels of Naxos (Koronos and Core Units; Lamont et al., 2019; Peillod et al., 2021a**)**, and thermal and petrological arguments for contrasting metamorphic *P–T* loops and cooling histories between different structural levels, suggest the MCC is composed of geologically distinct units (Zas Unit vs Koronos/ Core Unit). Crucially, this invalidates the homogenous rock sequence assumption, and therefore the extrapolation of the *HP* (M_1) event into the deeper levels of the MCC is unjustified.

Despite the above arguments, Peillod et al., (2017, 2021a,b) favored the *HP* interpretation for the Eocene zircon rim dates and proposed the entire shelf carbonate sequence (Koronos and Zas Units) belong to the CBU and experienced an M_1*HP* history, with both Koronos and Zas Units being thrust over the basement (Core Unit) that did not experience *HP*. This interpretation is fundamentally similar to the model proposed by Lamont et al., (2019), involving overthrusting of the CBU nappe onto Cycladic Basement in the footwall; however, the key difference being the structural position of the base of the CBU. Peillod et al., (2021a,b) interpret the Koronos Shear Zone that represents the basement/shelf contact as the base of the CBU and they propose the M_2 kyanite grade metamorphism in the Koronos Unit occurred following decompression from an earlier *HP* stage. However, this explanation is not consistent with the M_2 prograde thermobarometric data presented by Lamont et al., (2019) which show that the Koronos Unit garnet growth occurred during increasing M_2 pressures and temperatures from ca. 6 kbar and 550 ºC to ca. 10 kbar and 680 ºC (sample TL67). This decompression/ thermal overprint model also fails to explain extremely short drop-off length scales of Barrovian isograds (~4 km), sharply contrasting M_2 pressures, and strikingly contrasting cooling histories with structural depth within the MCC, as discussed above. Alternatively, according to Lamont et al., (2019), the base of the

CBU corresponds to the ZSZ, that approximates the biotite-in, chloritoid-out isograd and the last appearance of glaucophane in thin section. In this model, the ZSZ overprints or cuts out the thrust responsible for overthusting the CBU/ Zas Unit and therefore the Koronos and Core Units are located in the footwall beneath the overthrusted CBU nappe, and therefore underwent a completely separate metamorphic history. This can explain the contrasting clockwise metamorphic *P–T* paths between the older retrogressed blueschists at high structural levels and younger kyanite-sillimanite grade rocks at deep structural levels of the MCC. Since the structurally deepest rocks in the ACM are only exposed at the deep levels of Naxos, an alternative explanation to the Eocene zircon rim dates could reflect the start of Barrovian heating or another cryptic metamorphic event that has not been documented elsewhere.

Although the Eocene zircon rim dates could relate to an early metamorphic event at intermediate structural levels of Naxos (Koronos Unit), this cannot be assumed equivalent to the M_1 event exposed at structurally high levels of the MCC (Zas Unit). In our opinion, the interpretation to the Eocene U–Pb dates is highly speculative and could represent any metamorphic process which facilitates garnet growth. The new allanite geochronology will provide an independent constraint on the timing of peak M_1 *HP* metamorphism on Naxos and therefore new insight into what these Koronos Unit zircon rim dates represent.

Irrespective of whether the Koronos Unit experienced an early *HP* history or not, thermobarometry and equilibrium phase diagram modeling demonstrate that both intermediate and deep levels of the MCC (Koronos and Core Units) experienced a clockwise prograde M_2–M_3 *P–T* loop with increasing temperature and pressure along a Barrovian-type geotherm ~20–25 °C.km^{-1} (Lamont et al., 2019). If the Koronos Unit did experience an earlier M_1 *HP* history, the M_2–M_3 Barrovian *P–T* loop must completely overprint it, and the M_2 cycle must be associated with another phase of re-burial and compression at much deeper crustal levels than the Zas Unit, after any hypothetical exhumation from *HP*.

3. U–(TH)–PB GEOCHRONOLOGY

Discrimination between the effects of compressional and extensional tectonics on the thermal budget of the Naxos MCC requires precise constraints on the timescales of heating. As discussed above, the existing geochronology is widely debated, with several interpretations of dates spanning ca. 50–30 Ma in terms of their correlation to the M_1 or M_2 pressure-temperature paths. As such, a more robust geochronological framework would be beneficial to constrain the timing of peak *HP* (M_1) conditions and overthrusting of the Zas Unit/CBU and subsequent Barrovian metamorphism (M_2) on Naxos.

Allanite is a useful petrochronometer in *HP–LT* terranes because: (1) it is the dominant carrier of light rare earth elements (LREE's) in subducted crust (Hermann 2002); (2) it may grow early, before garnet, during the prograde metamorphic cycle and yet retains radiogenic Pb to >800 °C (Smye et al., 2011; Smye et al., 2014; Oberli et al., 2004); (3) its growth can be linked to rock-forming phases due to its chemical flexibility (owing to an expanded solid solution relative to most other minerals); (4) it is (relatively) resistant to high-grade deformation (Corti et al., 2020). In rocks of sufficient CaO and LREEs, allanite forms at the expense of authigenic, detrital or low-grade metamorphic monazite under 350–450 °C (Wing et al., 2003; Janots et al., 2007, 2008, 2009; Spear, 2010) and breaks down close to the staurolite isograd (Janots et al., 2008, 2009). Allanite can also become isolated from the reacting matrix, allowing evidence of former metamorphic events to be preserved, even if matrix crystals are partially reset during subsequent metamorphism (Montel, 2000). Allanite is therefore well suited to constrain the timing of M_1 metamorphism. Xenotime growth can be complex and affected by retrograde fluids, therefore it is potentially useful for dating the M_2 metasomatic overprint (Gysi and Harlov, 2021).

New U–(Th)–Pb dates were measured in the Geochronology and Tracers Facility at the British Geological Survey, Nottingham, UK. The method follows that described by Smye et al. (2014), and a full description of the analytical procedures is presented in the supplementary material and summary results, with comparison to existing geochronology and thermobarometry presented in Table 1. The ages are quoted with 95% confidence limits as α/β, where these exclude and include the systematic uncertainties respectively (following Horstwood et al., 2016). Since all of the samples were measured during a single session, the allanite dates can be compared against each other at the α uncertainty level, but should be compared against existing geochronology at the β uncertainty level.

4. ZAS UNIT PETROGRAPHY

Petrographic and microstructural observations of the Zas Unit/CBU are documented here (Fig. 5) to link *P–T* evolution with reported allanite and xenotime dates (Fig. 6). For a complete description of thermobarometry and mineral chemistry we point the reader to Lamont et al., (2019) and Peillod et al., (2017, 2021a). Zas Unit rocks display partially preserved blueschist-facies paragenesis (M_1) overprinted by greenschist-facies assemblages (M_2), with retrograde replacement spatially concentrated along shear zones associated with retrograde fluids (Fig. 5). *HP* (M_1) phases occur as relict, matrix grains or as inclusions trapped inside (M_2) greenschist-facies porphyroblasts. Three fabric elements can be identified that reflect the transition from blueschist-greenschist facies paragenesis.

The S_1 fabric is defined by a pervasive top-to-NE S–C' shear fabric that is associated with a NE–SW trending lineation (L1; Figure 5a–c; sample TLN54; Figure 5k; Sample TLN30) defined by M_1 *HP* phases including glaucophane porphyroblasts, phengite (white mica Si per formula unit (pfu) >3.4), paragonite (Na white mica with Si pfu<3.1), rutile and quartz. Glaucophane, paragonite and rutile also occur as prismatic inclusions in retrograde epidote-clinozoisite grains (TLN25 and TLN30). In samples TLN54 allanite occurs as matrix porphyroblasts aligned with the S_1 fabric (TLN54) or within cores of clinozoisite/epidote (TLN30) aligned with S_1. The S_1 fabric is folded into crenulations and variably overprinted by an axial planar fabric penetrative fabric (S_2) (Fig. 5a, l). The S_2 fabric is characterized by the development of crenulation cleavages and also centimeter- meter scale isoclinal folding of both *HP* (M_1) blueschist facies matrix phases (rutile, phengite and paragonite), and overprinting M_2 greenschist facies phases including muscovite (K white mica with Si per formula unit <3.2), biotite, actinolite, epidote and chlorite and albite (Fig. 5b, f, h, j, m). The S_1 and S_2 fabrics can also be traced by *HP* inclusion trails (rutile, glaucophane and phengite) throughout crosscutting epidote-clinozoisite porphyroblasts in some samples (Fig. 5l), suggesting epidote-clinozoisite and S_2 formed at or shortly following peak M_1 pressures and during the decompression from blueschist-greenschist facies conditions (Fig. 4a). Epidote/clinozoisite grains are also rimmed by retrograde albite and chlorite (Fig. 5 g–h), potentially indicating epidote formed at elevated pressure beyond the albite stability field but after peak M_1 pressures. Allanite in TLN26 is aligned with the variably folded S_2 fabric defined by greenschist facies assemblages. The S_3 fabric cuts both S_1 and S_2 crenulations and M_1 and M_2 phases and is characterized by a penetrative greenschist facies top-to-NNE (S–C′) shear (Fig. 5l). S_3 is localized along discrete shear zones including the ZSZ and has an NNE–SSW trending lineation (L_2) defined by actinolite, chlorite, albite and quartz. Xenotime occurs in dilatational strain zones around magnetite crystals and quartz or calcite veins and often chlorite-quartz intergrowths that are interpreted to represent healed fluid veins, that are affected by the S_3 shear. Xenotime is therefore interpreted constrain greenschist-facies retrogression (M_2) and pre-dates S_3 shearing related to final exhumation through the brittle-ductile transition (Buick and Holland, 1989; Urai et al., 1990; Avigad, 1998; Lamont et al., 2019).

4.1 TLN54: Glaucophane-Phengite Schist

Allanite is idioblastic (Fig. 5b–c) and aligned with the blueschist-facies S_1 fabric defined by phengite, glaucophane, rutile and epidote/clinozoisite. Petrological modeling suggest the M_1 assemblage equilibrated at 14.5 ± 0.5 kbar and 470 ± 30 °C along the epidote-lawsonite transition, whereas THERMOCALC AV–PT calculations suggest 12.6 ± 0.8 kbar and 483 ± 13 °C (Lamont et al., 2019) in the presence of retrograde epidote and albite. In contrast, xenotime is poorly formed and occurs along healed fluid fractures, associated with retrograde quartz/chlorite intergrowths along the edge of a 5 mm retrograde magnetite crystal (Fig. 5b) that cross cuts the S_1 and S_2 fabrics. Xenotime is therefore interpreted to be a retrograde phase associated with metasomatism during M_2.

4.2 TLN26: Actinolite-Epidote-Phengite Schist

Allanite is aligned with the retrograde transitional blueschist to greenschist-facies S_2 fabric defined by phengite, actinolite, chlorite, biotite, albite, epidote and titanite (Fig. 5f–h, m). THERMOCALC AV–PT calculations including albite suggest 11.6 ± 2.2 kbar and 483 ± 35 °C (Lamont et al., 2019). This result is consistent with the growth of epidote/clinozoisite (a retrograde mineral after lawsonite; Lamont et al., 2019), signifying the assemblage equilibrated after attaining peak M_1 pressures and during exhumation through the lower blueschist to upper facies. Because allanite is an integral part of the retrograde S_2 fabric (Fig. 5 g), we interpret allanite to have also crystallized after the rock attained its peak M_1 pressures. In contrast, xenotime occurs adjacent to quartz/ calcite veins and fractures, suggesting it grew during retrograde metasomatism.

4.3 TLN30 Phengite-Clinozoisite Schist

TLN30 comprises >50% clinozoisite with interstitial quartz, phengite, chlorite and rutile rich domains. Clinozoisite traps glaucophane and rutile inclusions and is interpreted to be retrograde after lawsonite, the latter of which are predicted to be stable at peak M_1 pressures (Fig. 4a, 5k, n). Allanite occurs within the cores of clinozoisite, and are associated with faint alteration zones that define its presence (Fig. 5n), allanite is therefore interpreted to pre-date clinozoisite and formed at, or close to peak M_1 pressures.

5. U–(TH)–PB RESULTS

5.1 TLN54: Glaucophane-Phengite Schist

The allanite analyses contained a uniformly high abundance of common Pb. A Tera-Wasserburg regression (Fig. 6a) using the combined U–(Th)–Pb measurements (Vermeesch, 2018, 2020) yields a lower intercept age of 50.35 ± 5.16/5.47 Ma (MSWD = 0.88; n = 20). The measured xenotime has variable amounts of common-Pb, with a regression of the data providing a lower intercept age of 21.70 ± 0.59/1.31 Ma (MSWD = 0.73, n = 7; Fig. 6b).

5.2 TLN26: Actinolite-Epidote-Phengite Schist

Allanite yielded a high abundance of common Pb and provides a U–(Th)–Pb lower intercept age of 40.52 ± 2.30/2.72 Ma (MSWD = 2, n = 12), (Fig. 6c). The analyzed xenotime is aligned subparallel to veining fractures and yields a lower intercept age of 30.61 ± 0.39/0.52 Ma (MSWD = 1.3, n = 6; Fig. 6d).

5.3 TLN30 Phengite-Clinozoisite Schist

DOI:10.1130/B36332.1

Allanite is characterized again by high amounts of common Pb, with regression of the data providing a lower intercept age of 49.42 ± 4.69/5.02 Ma (MSWD = 0.43, n = 16; Fig. 6e).

6. TECTONIC IMPLICATIONS

The new Zas Unit allanite U–(Th)–Pb dates span ca. 55–38 Ma, and xenotime dates range from ca. 32–20 Ma (Fig. 7a). Idioblastic allanite in TLN54, aligned with the glaucophane bearing top-to-NE S_1 shear fabric, is an integral part of the M_1 assemblage, and therefore considered to constrain peak M_1 pressures. Textural consideration of allanite rimmed by clinozoisite, alongside glaucophane inclusions trapped in epidote in TLN30, suggests that allanite grew in the presence of glaucophane and prior to clinozoisite during prograde or peak M_1 conditions or immediately following peak pressures. This is because clinozoisite is a retrograde phase, whereas lawsonite would have been stable with allanite at peak pressures of ca. 14.5 kbar and 470 ºC (pseudosection) and 12.3 ± 0.8 kbar and 483 ± 13 °C by AV–PT (Fig. 4a). U–(Th)–Pb dates from TLN54 and TLN30 of 50.4 ± 5.5 and 49.4 ± 5.0 Ma, respectively, are therefore interpreted to represent the timing of peak blueschist-facies (M_1) metamorphism on Naxos. Despite the large uncertainties, inherent from the low concentrations of radiogenic lead, the low MSWD suggest single age populations. These ca. 50 Ma allanite dates overlap with the upper range of the K–Ar and ^{40}Ar–^{39}Ar M_1 age spectrum (ca. 50–42 Ma; Andriessen et al., 1979, 1987; Wijbrans and McDougall, 1986, 1988), and coincide with the 'peak' M_1 age of ca. 50 Ma determined by ^{40}Ar–^{39}Ar (Wijbrans and McDougall, 1988). However, the ca. 50 Ma allanite dates are up to ca. 10 Myr older than the 40 ± 1 and 38.5 ± 1 Ma dates derived from Rb–Sr on white mica (Peillod et al., 2017), which were interpreted as dating blueschist-facies shearing and prograde dehydration at or near peak (M_1) blueschist-facies conditions respectively.

TLN26 allanite records a distinctly younger date of 40.5 ± 2.7 Ma. Because allanite is an integral part of the retrograde assemblage that equilibrated at 11.6 ± 2.2 kbar and 483 ± 35 °C (Lamont et al., 2019) in the presence of albite, (i.e., lower pressure than sample TLN54), we interpret the date as constraining retrograde blueschist to upper greenschist-facies conditions as the rock was being exhumed from subduction depths. This date is consistent with the ca. 40 Ma Rb–Sr white mica date for blueschist-facies shearing (Peillod et al., 2017), the and the lower end of ^{40}Ar–^{39}Ar and Rb–Sr dates from the CBU on Syros, Sifnos, Ios and Tinos (Bröcker et al., 1993, 2004, 2013; Putlitz et al., 2005; Cliff et al., 2017; Forster and Lister, 2016) Interestingly, it also overlaps the ca. 40 Ma U–Pb zircon dates from the structurally deeper Koronos Unit (Martin et al., 2006; Bolhar et al., 2017).

We interpret our new allanite dates as constraining two different points on a single *P*–*T* loop, with peak (M_1) blueschist facies conditions of ca. 14.5 kbar, 470 ºC at ca. 50 Ma, followed by exhumation to lower pressure/retrograde blueschist-facies to upper greenschist-facies conditions of ca. 11.6 kbar and 480 ºC. Although our two different allanite dates (ca. 50 Ma and ca. 40 Ma) could be interpreted to represent two distinct *HP* events within the CBU, this hypothesis is not supported by several arguments: (1) Samples TLN54, TLN30 and TLN26 are located at similar structural positions on Naxos, suggesting they are part of the same nappe, and therefore likely reached *HP* conditions at the same time. (2) The spectrum of Rb–Sr white mica dates from several Cycladic Islands span ca. 53–30 Ma suggesting the CBU was continuously exhumed over this ca. 20 Myr period, and therefore that older dates likely represent prograde/peak conditions and younger dates represent retrogression during exhumation. (3) Allanite in TLN26 (ca. 40 Ma) is an integral part of the retrograde assemblage. (4) A retrograde origin of the Naxos ca. 40–38.5 Ma Rb–Sr dates and ca. 40 Ma allanite is consistent with recent findings by Gorce et al., (2021), who show that prograde and peak blueschist-eclogite facies conditions of ca. 21 kbar and 560 °C on Syros occurred at or prior to ca. 45 Ma, whereas ca. 40 Ma younger garnet rim dates record garnet growth during exhumation from the subduction zone at ca. 16 kbar and 550 °C. For these reasons, we suggest that the Rb–Sr system and the allanite in sample TLN26 is recording retrogression during the exhumation of the CBU/Zas Unit from subduction zone depths, although possibly still at blueschist-facies conditions, before incorporation into the mid-crust.

Although the CBU comprises geologically distinct tectono-stratigraphic subunits that appear to have attained their peak conditions at slightly different times (Gorce et al., 2021), the new ca. 50 Ma allanite dates also confirm that the Zas Unit (the proximal Adriatic continental margin) was buried down the NE-dipping subduction zone and experienced its maximum depths (peak M_1) at approximately the same time as the rest of the CBU on Syros, Sifnos and Tinos (ca. 53–45 Ma) (Fig. 4b and Figure 7a; Tomaschek et al. 2003; Lagos et al., 2007; Dragovic et al., 2012; Bulle et al., 2010; Bröcker and Enders, 1999; Gorce et al., 2021, Uunk et al., 2022), based on the ability of Lu–Hf and Sm–Nd garnet geochronology to constrain approximately peak eclogite facies conditions, which overlap with U–Pb zircon dates from similar eclogite or blueschist-facies rocks at similar structural subunits of the CBU.

The new allanite geochronology unfortunately does not shed new light on the elusive Eocene U–Pb zircon rim dates from the Koronos Unit (Martin et al., 2006; Bolhar et al., 2017). Despite the ca. 50 Ma allanite dates being potentially older than the main ca. 40 Ma zircon rim age population, single spot zircon analyses range from ca. 69–40 Ma (Martin et al., 2006) and ca. 47–38 Ma (Bolhar et al., 2017), overlapping with both ca. 50 Ma and 40 Ma allanite dates. However, given the complete lack of *HP* assemblages or relicts in Koronos Unit rocks, and the fact that the Eocene zircon dates cannot be demonstrably linked to specific *P*–*T* conditions, we remain highly speculative on what these zircon dates represent. One possibility is the Eocene zircon rims constrain the start of Barrovian heating (M_2) related to overthrusting of the *HP* CBU/ Zas Unit rocks. This scenario is subsequently discussed with regards to competing thermal models for Naxos (Fig. 8). Further detailed geochronological investigation would be required to entirely resolve this debate, which is unfortunately beyond the scope of this study, although we can test the feasibility of current interpretations in our thermal model (Figs. 9–11).

Xenotime dates of ca. 30–21 Ma (Fig. 6b, d and Fig. 7a) overlap with M_2 Rb–Sr white mica dates of ca. 32–27 Ma (Fig. 7a; Peillod et al., 2017), and the broad range of M_2 ^{40}Ar–^{40}Ar dates between ca. 27–20 Ma for the high structural levels of the MCC (Zas Unit/ Zones 1–3; Wijbrans and McDougall, 1988), indicating that the Zas Unit/CBU was incorporated into the mid-crust (~6 kbar, 400 °C) structurally above the present day Koronos/Core Unit by ca. 30 Ma, ~20 Myrs after reaching the peak subduction depths during M_1. Because xenotime has an irregular habit and is distributed along fractures and veins, we interpret the xenotime dates as representing retrograde metasomatism; this likely resulted in breakdown of allanite or garnet liberating Y into the surrounding rock. Interestingly TLN54 xenotime may record a slightly younger date of ca. 21 Ma given its slightly deeper structural position in the MCC, which is consistent with experiencing more prolonged Barrovian heating. The range of xenotime dates therefore represent a protracted period of M_2 Barrovian heating and fluid-flow that pre-dates and overlaps with M_2 zircon dates of ca. 24–15 Ma from structurally deeper levels (Koronos/ Core Unit). These dates suggest that the thermal climax in the Zas Unit occurred ca. 5–15 Myr before peak M_2 Barrovian conditions were attained at structurally deeper levels of the MCC.

Insight into the exhumation and cooling history of the MCC can be gleaned by incorporating our new U–Pb data with existing thermochronology including K–Ar and ^{40}Ar–^{39}Ar of hornblende, white mica and biotite (representing closure temperatures of ~550–450 °C, ~500–450 °C and ~400–300 °C respectively; Harrison et al., 1985; Wijbrans and McDougall., 1986; 1988; Harrison et al., 2009; Warren et al., 2012), combined with zircon and apatite fission track data (closure temperatures of ~300–200 °C and 110–60 °C respectively; Kumar et al., 1995; Chew and Spikings, 2015; Figure 7b–g). Assuming the youngest age cluster as the most reliable due to Ar loss and excess Ar (Kelley, 2002; Warren et al., 2012), a step function trend can be established (Fig. 7b–f). The structurally highest levels of the MCC (Zas Unit/CBU) experienced cooling of ~3 $°C·Myr^{-1}$ through these closure temperatures between ca. 40–15 Ma (Fig. 7b), consistent with exhumation being erosion-driven and not requiring tectonic denudation. Slow cooling in the Zas Unit/CBU also pre-dates peak M_2 zircon ages of the underlying Koronos/Core Units of ca. 24–15 Ma (Fig. 7d–e). These contrasting thermal histories, as firstly pointed out by Wijbrans and McDougall, (1988), further support the hypothesis that the Zas Unit/CBU was exhumed to much shallower crustal depths and emplaced structurally 10's km above deeper levels of the MCC (Koronos/Core Units). This occurred while the structurally deeper levels of the MCC were experiencing prograde M_2 amphibolite-facies Barrovian heating and dehydration reactions, that potentially hydrated the overlying upper crustal CBU/Zas Unit rocks (Fig. 7b–f). After ca. 15 Ma, all structural levels experience rapid cooling of ca. 60–90 $°C·Myr^{-1}$ (Ryb et al., 2017). The timing of cooling and exhumation coincides with the initiation of extensional structures, including the NPDS at ca. 11–9 Ma (Mancktelow et al., 2016; Seward et al., 2009) that crosscuts and telescopes the previously 'frozen in' metamorphic stratigraphy. Interestingly, this timing overlaps with a twofold decrease in the Eurasia–Nubia convergence rate at ca. 18–13 Ma (DeMets et al., 2015).

In summary, the new allanite and xenotime data, in combination with existing geochronology and thermobarometry, support the hypothesis that Barrovian metamorphism on Naxos was diachronous, and that the MCC represents two distinct tectono-metamorphic units that attained their peak M_2 conditions at different times and have been tectonically juxtaposed against each other (Lamont et al., 2019; Fig. 8b). This requires that the Zas Unit/CBU which records an M_1 *HP* history, to have been extruded toward the SW from the NE-dipping subduction zone, and emplaced structurally above the Koronos/Core Units (Fig. 8b, 9a). Overthrusting of *HP* rock requires: (1) a mechanism to exhume the Zas Unit/CBU from ~50–70 km to 20 km depth between ca. 50 Ma, and (2) the onset of Barrovian heating (M_2) by ca. 40 Ma, assuming a Barrovian origin to the elusive zircon rim dates, or certainly by ca. 30 Ma. Rapid exhumation of the Zas Unit/CBU from the subduction zone would have occurred within a subduction channel or as an extruding wedge (Platt, 1993), and would be facilitated by a buoyancy contrast between the subducted crustal material and surrounding mantle ($\Delta\rho = 300$ $kg.m^{-3}$, England and Holland, 1979) following detachment from the subducting slab (Laurent et al., 2018; Lamont et al., 2020b). Evidence for diverse CBU *P–T–t* paths across the Cyclades suggests that the CBU was exhumed as several discrete but coherent subunits (Lamont et al., 2020b). Return flow of low viscosity continental margin material within a confined subduction channel or wedge could account for the exhumation of *HP* rocks (Cloos, 1982; Platt, 1993; Stöckhert et al., 1997; Stöckhert, 2002; Gerya and Stöckhert, 2006; Gerya et al., 2002; Warren et al., 2008). The CBU and its internal subunits are structurally bounded by shear zones at the top and bottom consistent with this extrusion mechanism (Huet et al., 2009; Laurent et al., 2016; Peillod et al., 2017; Lamont et al., 2019; Ring et al., 2020). Broadly speaking, the Vari Detachment bounds the top of the CBU on Syros and this, or an earlier and deeper structure acted as a passive roof fault during syn-orogenic extrusion of the CBU from subduction depths associated with extensive top-to-NE shear (S_1) (Fig. 8a, b stage 1, Figure 9b and Fig. 14a) throughout the CBU. The South Cycladic Thrust exposed on Ios (Huet et al., 2009), bounds the bottom of the CBU, and is associated with top-to-SW kinematics and places the CBU onto Variscan basement and amphibolite facies sedimentary cover that did not experience *HP* (Vanderberg and Lister, 1996). Several other top-to-SW thrust faults have been identified throughout the CBU (e.g., Kionnia Thrust and Sostis Thrust on Tinos and Kastri Basal fault on Syros), which appear to be synchronous with top-to-NE normal sensed shear zones at structurally higher levels (Lamont et al., 2020b; Ring et al., 2020; Philippon et al., 2011). Although we interpret the greenschist-facies ZSZ to define the base of the Zas Unit/CBU on Naxos (following Lamont et al., 2019), this is demonstrated to be a late structure, and must cut out or overprint the earlier Eocene aged thrust responsible for the emplacement of the Zas Unit/CBU to explain the contrasting tectono-thermal histories (Figs. 4a and 8). The high strain on the South Cycladic Thrust must have accommodated ~30–50 km of vertical displacement during exhumation of the CBU, prior to insertion between the upper plate (Upper Cycladic Nappe) and the structurally deeper Koronos/Core Units.

7. THERMAL MODEL

Using the new geochronological constraints on the timing of M_1 metamorphism and overthrusting on Naxos at ca. 50 Ma, we seek to understand the relative importance of crustal thickening and lithospheric extension in the thermal evolution of the Naxos MCC. We therefore investigate the range of overthrust parameters, including radiogenic heat production drop-off length scale (D), mantle heat flow (q_m), erosion (V_{er}) and thrust sheet thickness (*Thr*) that closely reproduce peak Barrovian *P–T–t* constraints within ~30–35 Myrs of overthrusting. We then investigate how a scenario of depth dependant lithospheric extension with crustal thinning (β) and mantle thinning (γ) factors that are varied in duration and magnitude commencing at ca. 25–15 Ma effect the thermal evolution.

We utilize a 1-D thermal model using a Crank-Nicolson finite difference scheme to solve the advective diffusion equation with radiogenic heating and depth dependent extension, following the approaches of England and Thompson (1984) and Bown and White (1995):

$$\frac{dT}{dt} = \kappa \frac{d^2T}{dZ^2} - \left\{ [V_e(Z,t)] \left[\frac{dT}{dZ} + h_a \right] \right\} + A_r\{Z - [V_e(Z,t)]t\}$$

Where T is temperature, Z is depth, t is time, κ is thermal diffusivity, V_{er} is erosion, ha is mantle adiabatic gradient, and A_r is radiogenic heating. For a complete description of the thermal model refer to the supplementary text S1. The overthrust model setup is shown in Figure 9 with an investigation of parameter space results in Figure 10, synthrust heating calculations are presented in Figure 11 and the depth-dependent extensional model set up in Figure 12 and parameter space investigation in Figure 13. We assume a surface temperature of 0 °C, and constant heat flow at the base of the lithosphere (125 km depth) throughout the model. We assume an initial condition that involves a single thrust sheet with a basal temperature varied between 500 and 570 °C and instantaneous thrusting, creating a sawtooth geotherm (Fig. 9a). The hangingwall of the overthrust sheet represents the position of the Zas Unit/CBU at 50 Ma, immediately following overthrusting of the CBU from ~50–70 km depth (ca. 14–19 kbar and 470–570 °C) to ~20–30 km depth (6–8 kbar, 450–570 °C), although we acknowledge that the exact timing of thrusting maybe a few Myrs younger than 50 Ma. The footwall rocks comprise the proximal Adriatic continental margin and Variscan Basement, (Koronos/Core Units) that experienced ca. 10–5 kbar and 650–730 °C during a thermal climax (M_2–M_3) at ca. 20–15 Ma. Successful solutions are considered to satisfy footwall (Koronos/Core Unit) *P–T–t* constraints.

The mantle adiabatic gradient (h_a) of 0.4 °C.km^{-1} is included in thinning calculations. The modeled 1-D crustal section represents the position where maximal crustal thickening occurred, facilitating investigation of the thermal evolution after the overthrusted CBU/Zas Unit experienced its peak pressure. We then consider the effect of syn-thrust heating, involving tectonic replenishment of heat from the overthrusted CBU/Zas Unit, following the approaches of Smye et al., (2011) and early ophiolite obduction of the Tsiknias Ophiolite at ca. 75 Ma (see supplementary text S1).

8. THERMAL MODEL RESULTS

8.1 Crustal Thickening and Overthrusting of the CBU at 50 Ma

Overthrust calculations show that the magnitude and time scales of Barrovian heating are dependent on the combination of model parameters (*Ve*, *Thr*, *D* and q_m; Figures 9–10). Under constant q_m the distribution of radiogenic material and erosion rates have the greatest influence (Fig. 10; England, 1978; Jaupart et al., 2016). When erosion rates are relatively low (*Ve* <0.5 km·Myr^{-1}), the thermal climax is predicted at ca. 20–15 Ma, ~30–35 Myrs after overthrusting of the CBU/ Zas Unit (Figs. 9–10). When V_{er} is >0.5 km·Myr^{-1}, there is increased exhumation and conductive cooling at all crustal levels, ultimately limiting peak Barrovian temperatures and shortening the duration of the metamorphism (Fig. 10c; e.g., England and Richardson, 1977). For thin thrust sheets (*Thr* <25 km), model Barrovian conditions fall short of the *P–T* constraints as footwall rocks are not buried to sufficient depths, whereas thick thrust sheets (*Thr* >35 km) overpredict M_2 pressures and do not cause as much heating for the investigated time-scales (Fig. 10a). Thrust sheets ~30 km thick satisfy peak Barrovian pressures of ca. 10 kbar, and were used for further calculations. When *D* >12 km, peak Barrovian temperatures of 650–730 °C are well satisfied, and the model reproduces a clockwise *P–T–t* path with the crustal geotherm evolving from ~10 °C.km^{-1} to ~25 °C.km^{-1} over a ~35 Myr time interval (Figs. 9 and 10). The Zas Unit/CBU are also incorporated into the Barrovian tectono-metamorphic cycle, undergoing near isobaric heating of ~50 °C to peak Barrovian temperatures of ~550 °C and ~7–10 kbar at 30–20 Ma, which is also observed on Syros and Tinos (Lamont et al., 2020b; Parra et al., 2002; Avigad and Garfunkel, 1991; Laurent et al., 2018; Naxos; Lamont et al., 2019; Peillod et al., 2017, 2021a). Although *D* ~12 km is greater than the global average ~10 km (Jaupart et al., 2016), this could be explained by the structural repetition from thrusting (Lamont et al., 2019) and the potentially highly radiogenic Variscan granitic basement. Another consideration is that Aegean crust may not conform to the exponential distribution of radiogenic heat production with depth. The thermal model also does not reproduce well the lower pressure sillimanite-grade M_3 conditions recorded in the migmatite dome, without necessitating rapid erosion from ~20 Ma. However, this decompression is isothermal and can be explained by extrusion of the footwall beneath the KSZ and ZSZ (Lamont et al., 2019), therefore does not require further heating mechanisms.

8.2 Syn-Thrust Heating between 50 and 40 Ma Followed by Conductive Relaxation

Because the CBU is exposed >100 km across strike in present day coordinates and experienced vertical displacements of ~30–50 km during exhumation from subduction depths (Huet et al., 2009), it is likely that the South Cycladic Thrust accommodated at least 60–100 km of convergence assuming a dip on the thrust of ~30°. If the maximum duration of thrusting is 10 Myr (50–40 Ma), then thrust sheet emplacement of the CBU occurred at rates of 6–10 km·My^{-1}, similar to plate convergence rates. At high thrusting rates, the footwall Koronos/Core Units experience rapid heating due to the constant replenishment of heat by the overthrusted CBU nappe, which would effectively maintain a constant thermal gradient, analogous to a hot iron

(Fig. 11a; Smye et al., 2011). For this scenario to be plausible, the Koronos/Core Units must be located proximal to the inception of thrusting to limit conductive cooling of the Zas Unit/CBU thrust sheet. Figure 11 shows the thermal evolution of a crustal pile undergoing syn-thrusting heating for a thrusting rate of 10 km·Myr^{-1}. Syn-thrusting heating forms inverted isotherms within the footwall during early stages of thrusting. With subsequent conductive relaxation and radiogenic heating, footwall isotherms are smoothed and attain similar values to the base of the overthrust CBU within ca. 10 Myr (Fig. 11a–b). Syn-thrust heating may also explain the elusive Eocene zircon rim dates in the footwall Koronos Unit rocks as the start of significant Barrovian metamorphism (M_2) (Martin et al., 2006; Bolhar et al., 2017; Figure 11c, d). Syn thrust heating would also be consistent with kyanite grade isoclinal folding within the Koronos Unit (Lamont et al., 2019; Urai et al., 1990; Buick, 1991a,b). The temperature of the base of the CBU thrust sheet is varied from 500 °C to 570 °C, and the model geotherm and *P–T–t* paths are displayed in figure 11h–k and has little effect on the subsequent temperatures. Therefore, after thrusting seizes, the thermal evolution of the MCC is controlled primarily by the parameters discussed above, chiefly radiogenic heating, erosion rates and the timing and magnitude of depth-dependent extension.

8.3 Overthrusting Followed by Extension at 25 Ma

The onset of lithospheric extension at ca. 25 Ma represents the classical geodynamic model for Aegean MCC formation and the cause of Barrovian metamorphism (Figs. 1a and 12–13; Lister et al., 1984; Buick and Holland, 1989; Ring et al., 2003**;** Jolivet and Brun, 2010; Jolivet et al., 2004; 2010). For reasonable crustal and mantle thinning factors (β = 1.2–3; γ = 1.1–3), calculations suggest that rocks at mid-crustal levels experience no or very limited net heating, and in scenarios when β >1.2, rocks cool during extension of already thickened and thermally relaxed crust. This is because when β >1.2 or when $\beta \sim\gamma$ (i.e., pure shear extension) the crustal geotherm increases at the rate of conductive heat loss due to exhumation of rock at all crustal levels (Ruppel et al., 1988). The predicted *P–T–t* paths of rock display a kink to greater exhumation rates coinciding with the onset of extension (Figs. 12j and 13a–e, g), and do not increase in temperature during their exhumation (Fig. 12 and Figure 13a–e). This significant cooling and exhumation of rock during lithospheric extension is incompatible with *P–T–t* constraints which show further heating occurred on Naxos after 25 Ma (Fig. 12 g–h). In depth-dependent extension scenarios with limited crustal extension (β <1.2) and extensive mantle thinning (γ >>5), ~50–100 °C of near isobaric heating of the mid-crust (ca. 5–12 kbar) is predicted (Fig. 12c–d and Figure 13a–d, j–m). This is due to increased basal heating from the upwelling hotter asthenosphere in the absence of crustal exhumation. In this scenario, the crust essentially represents a stagnant lid, limiting conductive heat loss due to uplift of rock. Although possible, this model may only occur as a transient and isostatically unstable geodynamic scenario, such as immediately prior to the onset of large magnitude crustal extension, following convective removal of lithospheric mantle (England and Houseman, 1989; England, 1993; Platt and England, 1994). However, as discussed above, the magnitude of mid-crust heating (representing the position of Naxos MCCs) is severely limited, due to the great Moho depth from previous crustal thickening (>50 km) and may only be important if the crust was not previously thickened and had relatively low concentrations of radiogenic elements (*D* <8 km). Extreme depth-dependent extension also requires significant decoupling between the crust and mantle at the Moho (Huismans and Beaumont, 2014), which may not be geologically realistic. We therefore argue that depth-dependant extension cannot explain significant Barrovian heating on Naxos, and our results suggest it may not be an important heating mechanism in MCCs that expose mid-crustal rocks like Naxos. We acknowledge however, that depth-dependant extension during a lithospheric mantle delamination event may explain short and longer time-scale lower crustal temperature excursions >200 °C in granulite facies metamorphic terranes that were once in close proximity to the pre-extensional Moho immediately prior to any significant crustal extension (Smye et al., 2019) (Fig. 12k, Figure 13a–e, 13k–m and supplementary text S1).

9. DISCUSSION

A maximum time interval of ~30–35 Myrs separates peak (M_1) *HP–LT* metamorphism of the Zas Unit/CBU at ca. 50 Ma and thermal climax (M_2–M_3) at ca. 20–15 Ma on Naxos. This is consistent with the time scales of conductive heating driven by relaxation of isotherms in regions of over-thickened crust (Oxburgh and Turcotte, 1974; Bickle et al., 1975; England and Richardson, 1977; England, 1978; England and Thompson, 1984; Spear and Peacock, 1989). Overthrusting of the Zas Unit/CBU onto the more proximal Adriatic continental margin between ca. 50 and 40 Ma would result in crustal thickening. M_2 kyanite-grade gneisses in the Koronos/Core Unit record pressures of ca. 10–11 kbar, requiring an overburden ~35 km thick. Assuming ~25 km of crust underlaid these rocks during M_2 based on the present-day Moho depth ~25 km (Tirel et al., 2004; Cossette et al., 2016), the ACM crust must have been ~60 km thick at the time of peak (M_2–M_3) Barrovian conditions at ca. 20–15 Ma. In such a scenario, the Koronos/Core Unit must have represented the mid-lower crust, and this implies the ACM crust must have thinned by at least a factor of two (β = 2) since the Late-Miocene. Although it has been argued the entire sequence of rocks on Naxos represents a homogeneous package of rocks that experienced an early *HP* (M_1) event followed by (M_2) Barrovian heating (e.g., Avigad, 1998; Katzir et al., 1999; Martin et al., 2006; Bolhar et al., 2017; Peillod et al., 2021a,b), this interpretation is unsupported by: (1) The lack of any evidence for *HP* (M_1) assemblages or relicts within the Koronos and Core Units. (2) The spatial and temporal diachroneity of M_2 conditions with depth into the MCC, as M_2 U–Pb xenotime and Rb–Sr white mica ages of ca. 30–20 Ma from high structural levels (Zas Unit) pre-date thermal climax (M_2–M_3) in the core at ca. 20–15 Ma by 5–15 Myrs. (3) The short (~4 km) length scale drop-off in M_2 Barrovian isograds and sharply contrasting Barrovian pressures and temperatures with structural depth into the MCC is inconsistent with thermal model results of conductive heating, which necessitates thermal length scales (structural thickness) >15 km to explain such temperature differences (Figs. 8–11). (4) Contrasting cooling histories between structurally high and intermediate/deep levels of the MCC. (5) The penetrative top-to-NNE shear on the ZSZ and KSZ that cross-cuts the earlier compressional structures. All of the above features suggest that Barrovian metamorphism (M_2–M_3) on Naxos was diachronous and propagated down structural level with time. The original M_2–M_3 metamorphic sequence has also been telescoped by top-to-NNE shearing on firstly, the ZSZ, that juxtaposes the *HP–LT* CBU rocks of the Zas Unit against the structurally deeper Barrovian-facies rocks (Koronos and Core Units); and secondly, by shearing on the NPDS, which post-dates peak metamorphism and migmatite doming as it cuts the metamorphic stratigraphy and the ZSZ.

The thermal model results of Zas Unit/CBU overthrusting, and especially when considering syn-thrust heating (Fig. 11a–b), reproduce the clockwise *P–T–t* path and kyanite-grade M_2 conditions (Figs. 9f–i, 10 g–h, k–l, 11c, k, l), assuming low erosion rates (<0.5 km·Myr^{-1}), ~30 km thrust sheet thickness (overburden) and a slightly greater than average radiogenic crust (*D* ~10–15 km). When *D* is <10 km, model temperatures fall ~100 °C short of peak Barrovian temperatures (Fig. 10a, c); however, this degree of heating is still greater than that predicted during reasonable extensional scenarios (i.e., β >1.2). Like many mountain belts, in the absence of highly radiogenic crust, additional heating mechanisms are required to attain anatectic conditions (Jamieson et al., 1998). This problem is further amplified when the latent heat of fusion is taken into consideration. Syn-thrust heating during emplacement of the CBU can potentially explain rapid footwall heating. This could provide a possible explanation for the Eocene U–Pb zircon rim dates (Martin et al., 2006; Bolhar et al., 2017) as being related to the onset of Barrovian heating rather than *HP* conditions. However, a combination of highly radiogenic crust and low erosion rates are still required to maintain and increase Barrovian temperatures over the following 20–25 Myrs in order to reach a thermal climax at ca. 20–15 Ma (Fig. 11a–c). Shear heating could also locally increase temperatures near major fault zones (Molnar and England, 1990; England and Molnar, 1993a,b), and has been shown to be important heating component in subduction zone *HP–LT* rocks (e.g., Kohn et al., 2018). Although we neglect shear heating in our calculations for simplicity and the lack of available physical constraints, we acknowledge shear heating may be required to raise Barrovian temperatures by 50–100 ºC to reproduce anatectic conditions in the core of Naxos.

Extension calculations suggest that isobaric heating of the mid-crust only occurs in scenarios with significant mantle thinning ($\gamma >>5$) and minimal crustal thinning ($\beta <1.2$), although this heating is limited due to the great Moho depth of previously thickened crust. Elevated mantle heat flow from removal or thinning of the lithospheric mantle may explain the increased geotherm of the lower crust for short time intervals but lacks supporting geochemical or magmatic evidence on Naxos and the ACM. The age of Cycladic I-type intrusions spans ca. 14.6–11 Ma (Keay et al., 2001; Iglseder et al., 2009; Bolhar et al., 2010), which post-dates peak Barrovian metamorphism, and there is no evidence for mantle melting or magmatism prior to this date. Such extreme depth-dependent extension scenarios also require significant decoupling of the crust and lithospheric mantle at the Moho, which may be tectonically unreasonable. Isobaric heating is also not compatible with the *P–T–t* path, which suggests prograde heating involved burial and was followed by isothermal decompression (Lamont et al., 2019; Figure 3a, Fig. 13e).

Crustal extension ($\beta >1.2$) causes cooling and exhumation of rocks for all timescales of extension, with the amount of cooling dependant on the magnitude and mode of thinning. This suggests that normal faulting and exhumation on Naxos did not occur prior to ca. 15 Ma due to persistence of Barrovian temperatures >600 °C and leucogranite intrusions at this time (Ring et al., 2018, Fig. 13e). Thermal models of normal fault footwalls also predict cooling and migration of the brittle-ductile transition upon the onset of extension (e.g., England and Jackson, 1987). Geological evidence from Naxos and other Cycladic islands suggests that rapid cooling and exhumation affected all structural levels after ca. 15 Ma (Fig. 7b–f, Fig. 13e), associated with the development of the NPDS and other extensional structures (e.g., NCDS and WCDS) that cross-cut the previously ‘frozen in’ metamorphic stratigraphy; coincidentally, the timing overlaps with a twofold decrease in the Nubia–Eurasia convergence rate (DeMets et al., 2015; Figure 14s tectonic model stage 6, d).

10. CONCLUSIONS

1. We present the first U–(Th)–Pb age of M_1 blueschist-facies metamorphism within the Zas Unit (CBU) on Naxos. Allanite grew at ca. 50 Ma during peak *HP* conditions, of ca. 14.5 kbar and 470 °C, and overlap with ca. 53–45 Ma dates for peak blueschist-eclogite conditions of the CBU elsewhere in the Aegean Sea. The ca. 50 Ma allanite dates are ~10 Myr older than ca. 40 Ma Rb–Sr white mica dates previously interpreted to represent the timing of peak *HP* metamorphism on Naxos and constrain a ~30–35 Myr time interval between (M_1) *HP–LT*

metamorphism of the Zas Unit/CBU and the thermal climax (M_2–M_3) in the structurally deeper Barrovian rocks at ca. 20–15 Ma.

2. Retrograde allanite and xenotime M_2 dates of ca. 40–20 Ma impose a ~10–20 Myr period for the CBU to be extruded toward the SW from subduction zone depths of ca. 50–70 km to crustal depths of ca. 20 km at rates of ~6–10 km·Myr^{-1} (Fig. 11a–b). The ca. 40 Ma allanite and existing Rb–Sr dates are interpreted to represent a retrograde blueschist-facies metamorphic stage during exhumation of the Zas Unit/CBU from the subduction zone. In contrast, previous Eocene U–Pb zircon rim dates in the Koronos Unit do not necessarily relate to *HP* metamorphism, due to the complete lack of petrographic evidence for *HP*, contrasting *P–T* paths, and overwhelming thermal arguments suggesting that the Naxos MCC does not represent a homogeneous package of rocks.

3. The ~30–35 Myr timescale of Barrovian heating prior to the M_2–M_3 thermal climax at ca. 20–15 Ma is consistent with thermal model results of crustal thickening, assuming relatively low erosion rates and slightly greater than average radiogenic crust. In this model, rapid Barrovian heating following overthrusting of the Zas Unit/CBU may explain the enigmatic Eocene U–Pb zircon rim dates at intermediate structural levels of the MCC (Koronos Unit) and occurs in timescales <10 Myr with continual replenishment of heat from the overthrusted Zas Unit/CBU.

4. The thermal model results tied to geochronological constraints are consistent with formation of the Naxos MCC in a compressional tectonic environment (Fig. 14a tectonic model stages 1–4 and 14b–c), prior to the onset of Aegean extension commencing at ca. 15 Ma, which was associated with the initiation of extensive normal faulting, rapid exhumation and cooling (Fig. 13e and Figure 14a tectonic model stages 5–6 and 14d).

5. The thermal model results suggest that the onset of crustal extension on Naxos (ca. 15 Ma) occurred during the climax of Barrovian metamorphism. Extension at reasonable crustal and mantle extension factors and rates causes rapid exhumation and cooling of the MCC after ca. 15 Ma. Only under extreme depth-dependant extension scenarios, such as the initial stages of a lithospheric foundering or a delamination event (β <1.2, γ >>5), does the mid-crust experience small degrees of isobaric heating (~50 °C). However, the magnitude of heating is limited by the great Moho depth (~60 km) of previously thickened crust. Such a scenario would also be expected to generate extensive mantle melting, evidence for which is not observed in the Aegean prior to ca. 15 Ma.

ACKNOWLEDGEMENTS

This work forms part of T.N. Lamont's doctoral project which is funded by the Natural Environment Research Council (Grant No. NE/L0021612/1) Analytical work at the NERC Isotope Geosciences Laboratory was funded by NIGFSC grant IP-1597–1115. We thank Philip England, Richard Palin, Brendan Dyck, Owen Weller, Phillip Gopon, Marc St-Onge, Andrew Parsons, Tony Watts, Dave Wallis, Lars Hansen, Tyler Ambrose and Frances Cooper for thought-provoking and critical discussion. We extend thanks to Callum Higgins, William Nash, and Anna Bidgood, for assistance in the field, Owen Green and Jonathan Wells for thin section preparation, and Gren Turner, Jeremy Rushton and Jon Wade for analytical assistance and Liam Smith for coding advise. Finally, we are greatly indebted to very helpful and critical reviews by Samuele Papeschi and Michael Bröcker that greatly improved the quality of the manuscript, and we thank Rob Strachan and Kathryn Cutts for their careful editorial handling.

REFERENCES CITED

Ague, J., and Baxter, E., 2007, Brief thermal pulses during mountain building recorded by sr diffusion in apatite and multicomponent diffusion in garnet: Earth and Planetary Science Letters, v. 261, p. 500–516, https://doi.org/10.1016/j.epsl.2007.07.017.

Altherr, R., Schliestedt, M., Okrusch, M., et al., 1979, Geochronology of high-pressure rocks on Sifnos (Cyclades, Greece): Contributions to Mineralogy and Petrology, v. 70, p. 245–255, https://doi.org/10.1007/BF00375354.

Andriessen, P.A.M., Boelrijk, N.A.I.M., Hebeda, E.H., Priem, H.N.A., Verdurmen, E.A.T., and Verschure, R.H., 1979, Dating the events of metamorphism and granitic magmatism in the Alpine orogen of Naxos (Cyclades, Greece): Contributions to Mineralogy and Petrology, v. 69, p. 215–225, https://doi.org/10.1007/BF00372323.

Andriessen, P.A.M., Banga, G., and Hebeda, E.H., 1987, Isotopic age study of pre-Alpine rocks in the basal units on Naxos, Sikinos and Ios, Greek Cyclades: Geologieen Mijnbouw, v. 66, p. 3–14.

Armstrong, R.L., 1982, Cordilleran metamorphic core complexes from Arizona to southern Canada: Annual Review of Earth and Planetary Sciences , v. 10, p. 129–154, https://doi.org/10.1146/annurev.ea.10.050182.001021.

Avigad, D., 1998, High-pressure metamorphism and cooling on SE Naxos (Cyclades, Greece): European Journal of Mineralogy, v. 10, p. 1309–1320, https://doi.org/10.1127/ejm/10/6/1309.

Avigad, D., and Garfunkel, Z., 1991, Uplift and exhumation of high-pressure metamorphic terrains: The example of the Cycladic blueschist belt (Aegean Sea): Tectonophysics, v. 188, p. 357–372, https://doi.org/10.1016/0040-1951(91)90464-4.

Baxter, E., Ague, J., and Depaolo, D., 2002, Prograde temperature–time evolution in the Barrovian type-locality constrained by Sm/Nd garnet ages from Glen Clova, Scotland: Journal of the Geological Society, v. 159, p. 71, https://doi.org/10.1144/0016-76901013.

Baziotis, I., Mposkos, E., Windley, B.F., and Lamont, T.N., (2020). Exhumation of Attica high-pressure rocks in a subduction channel: New metamorphic PT constraints from Attica, NW Cyclades, Greece. *Lithos*

Bickle, M.J., Hawkesworth, C., England, P.C., and Athey, D., 1975, A preliminary thermal model for regional metamorphism in the eastern Alps: Earth and Planetary Science Letters, v. 26, p. 13–28, https://doi.org/10.1016/0012-821X(75)90173-9.

Bickle, M., and McKenzie, D., 1987, The transport of heat and matter by fluids during metamorphism: Contributions to Mineralogy and Petrology, v. 95, p. 384–392, https://doi.org/10.1007/BF00371852.

Bird, P., 1979, Continental delamination and the Colorado Plateau: Journal of Geophysical Research. Solid Earth, v. 84, B13, p. 7561–7571, https://doi.org/10.1029/JB084iB13p07561.

Bohlen, S.R., 1987, Pressure-temperature-time paths and a tectonic model for the evolution of granulites: The Journal of Geology, v. 95, p. 617–632, https://doi.org/10.1086/629159.

Bolhar, R., Ring, U., and Allen, C.M., 2010, An integrated zircon geochronological and geochemical investigation into the Miocene plutonic evolution of the Cyclades, Aegean Sea, Greece: Part 1: Geochronology: Contributions to Mineralogy and Petrology, v. 160, p. 719–742, https://doi.org/10.1007/s00410-010-0504-4.

Bolhar, R., Ring, U., and Ireland, T.R., 2017, Zircon in amphibolites from Naxos, Aegean Sea, Greece: origin, significance and tectonic setting: Journal of Metamorphic Geology, v. 35, p. 413–434, https://doi.org/10.1111/jmg.12238.

Bown, J.W., and White, R.S., 1995, Effect of finite extension rate on melt generation at rifted continental margins: Journal of Geophysical Research, v. 100, B9, p. 18011–18029, https://doi.org/10.1029/94JB01478.

Bröcker, M., and Enders, M., 1999, U–Pb zircon geochronology of unusual eclogite-facies rocks from Syros and Tinos (Cyclades, Greece): Geological Magazine, v. 136, p. 111–118, https://doi.org/10.1017/S0016756899002320.

Bröcker, M., and Franz, L., 2006, Dating metamorphism and tectonic juxtaposition on Andros Island (Cyclades, Greece): results of a Rb–Sr study: Geological Magazine, v. 143, no. 5, p. 609–620, https://doi.org/10.1017/S001675680600241X.

Bröcker, M., Kreuzer, A., Matthews, A., and Okrusch, M., 1993, ^{40}Ar/^{39}Ar and oxygen isotope studies of poly-metamorphism from Tinos Island, Cycladic blueschist belt, Greece: Journal of Metamorphic Geology, v. 11, p. 223–240, https://doi.org/10.1111/j.1525-1314.1993.tb00144.x.

Bröcker, M., Bieling, D., Hacker, B., and Gans, P., 2004, High-Si phengite records the time of greenschist facies overprinting: Implications for models suggesting mega-detachments in the Aegean Sea: Journal of Metamorphic Geology, v. 22, no. 5, p. 427–442, https://doi.org/10.1111/j.1525-1314.2004.00524.x.

Bröcker, M., Baldwin, S., and Arkudas, R., 2013, The geological significance of ^{40}Ar/^{39}Ar and Rb–Sr white mica ages from Syros and Sifnos, Greece: a record of continuous (re)crystallization during exhumation?: Journal of Metamorphic Geology, v. 31, p. 629–646, https://doi.org/10.1111/jmg.12037.

Brichau, S., Ring, U., Ketcham, R.A., and Carter, A., 2006. Constraining the long-term evolution of the slip rate for a major extensional fault system in the central Aegean, Greece, using thermochronology: Earth and Planetary Science Letters, v. 241, p. 293–306. ISSN 0012–821X.

Brichau, S., Ring, U., Carter, A., Monie, P., Bolhar, R., Stockli, D., and Brunel, M., 2007, Extensional faulting on Tinos Island, Aegean Sea, Greece: How many detachments?: Tectonics, v. 26, p. TC4009, https://doi.org/10.1029/2006TC001969.

Brichau, S., Ring, U., Carter, A., Bolhar, R., Monié, P., Stockli, D., and Brunel, M., 2008, Timing, slip rate, displacement and cooling history of the Mykonos detachment footwall, Cyclades, Greece, and implications for the opening of the Aegean Sea basin: Journal of the Geological Society, v. 165, p. 263–277, https://doi.org/10.1144/0016-76492006-145.

Buck, W.R., 1988, Flexural rotation of normal faults: Tectonics, v. 7, p. 959–973, https://doi.org/10.1029/TC007i005p00959.

Buick, I.S., 1991a, Mylonite fabric development on Naxos, Greece: Journal of Structural Geology, v. 13, p. 643–655, https://doi.org/10.1016/0191-8141(91)90027-G.

Buick, I.S., 1991b, The late Alpine evolution of an exten- sional shear zone, Naxos, Greece [London]: Journal of the Geological Society, v. 148, p. 93–103, https://doi.org/10.1144/gsjgs.148.1.0093.

Buick, I.S., and Holland, T.J.B., 1989. The *P-T-t* path associated with crustal extension, *in* Daly, J.S., Cliff, R.A., and Yardley, W.D., eds., Evolution of Metamorphic Belts: Geological Society of London Special Publication v. 43, p. 365–369.

Bulle, F., Bröcker, M., Gärtner, C., and Keasling, A., 2010, Geochemistry and geochronology of HP mélanges from Tinos and Andros, Cycladic blueschist belt, Greece: Lithos, v. 117, no. 1–4, p. 61–81, https://doi.org/10.1016/j.lithos.2010.02.004.

Burg, J.P., and Gerya, T.V., 2005. The role of viscous heating in Barrovian metamorphism of collisional orogens: thermomechanical models and application to the Lepontine Dome in the Central Alps: Journal of Metamorphic Geology, v. 23, p. 75–95, https://doi.org/10.1111/j.1525-1314.2005.00563.x.

Burg, J.P., Guiraud, M., Chen, G.M., and Li, G.C., 1984, Himalayan metamorphism and deformations in the North Himalayan Belt (southern Tibet, China): Earth and Planetary Science Letters, v. 69, no. 2, p. 391–400, https://doi.org/10.1016/0012-821X(84)90197-3..

Cao, S., Neubauer, F., Bernroider, M., and Liu, J., 2013, The lateral boundary of a metamorphic core complex: The Moutsounas shear zone on Naxos, Cyclades, Greece: Journal of Structural Geology, v. 54, p. 103–128, https://doi.org/10.1016/j.jsg.2013.07.002.

Cao, S., Neubauer, F., Bernroider, M., Genser, G., Liu, J., and Friedl, G., 2017, Low-grade retrogression of a high-temperature metamorphic core complex: Naxos, Cyclades, Greece: Geological Society of America Bulletin, v. 129, p. 93–117, https://doi.org/10.1130/B31502.1.

Chew, D.M., and Spikings, R.A., 2015, Geochronology and thermochronology using apatite: time and temperature, lower crust to surface: Elements (Midland), v. 11, no. 3, p. 189–194, https://doi.org/10.2113/gselements.11.3.189.

Cloos, M., 1982, Flow melanges: Numerical modeling and geologic constraints on their origin in the Franciscan subduction complex, California: Geological Society of America Bulletin, v. 93, no. 4, p. 330–345, https://doi.org/10.1130/0016-7606(1982)93<330:FMNMAG>2.0.CO;2.

Cliff, R.A., Bond, C.E., Butler, R.W.H., and Dixon, J.E., 2017, Geochronological challenges posed by continuously developing tectonometamorphic systems: insights from Rb–Sr mica ages from the Cycladic Blueschist Belt, Syros (Greece): Journal of Metamorphic Geology, v. 35, p. 197–211, https://doi.org/10.1111/jmg.12228.

Coney, P.J., 1980, Cordilleran metamorphic core complexes: An overview, in Crittenden, M.D., Jr., Coney, P.J., and Davis, G.H., eds., Cordilleran Metamorphic Core Complexes : Geological Society of America Memoir 153, p. 7–34, https://doi.org/10.1130/MEM153-p7.

Corti, L., Zanoni, D., Gatta, G., and Zucali, M., 2020, Strain partitioning in host rock controls light rare earth element release from allanite-(Ce) in subduction zones: Mineralogical Magazine, v. 84, no. 1, p. 93–108, https://doi.org/10.1180/mgm.2020.4.

Cossette, É., Audet, P., Schneider, D., and Grasemann, B., 2016, Structure and anisotropy of the crust in the Cyclades, Greece, using receiver functions constrained by in situ rock textural data: Journal of Geophysical Research. Solid Earth, v. 121, p. 2661–2678, https://doi.org/10.1002/2015JB012460.

DeMets, C., Iaffaldano, G., and Merkouriev, S., 2015, High-resolution Neogene and Quaternary estimates of Nubia-Eurasia-North America Plate motion: Geophysical Journal International, v. 203, p. 416–427, https://doi.org/10.1093/gji/ggv277.

Dragovic, B., Baxter, E.F., and Caddick, M.J., 2015, Pulsed dehydration and garnet growth during subduction revealed by zoned garnet geochronology and thermodynamic modeling, Sifnos, Greece: Earth and Planetary Science Letters, v. 413, p. 111–122, https://doi.org/10.1016/j.epsl.2014.12.024.

Dragovic, B., Samanta, L.M., Baxter, E.F., and Selverstone, J., 2012, Using garnet to constrain the duration and rate of water-releasing metamorphic reactions during subduction: An example from Sifnos, Greece: Chemical Geology, v. 314-317, p. 9–22, https://doi.org/10.1016/j.chemgeo.2012.04.016.

DOI:10.1130/B36332.1

Duchêne, S., Aissa, R., and Vanderhaeghe, O., 2006, Pressure-temperature-time evolution of metamorphic rocks from Naxos (Cyclades, Greece): Constraints from thermobarometry and Rb/Sr dating: Geodinamica Acta, v. 19, no. 5, p. 301–321, https://doi.org/10.3166/ga.19.301-321.

Dürr, S., Altherr, R., Keller, J., Okrusch, M., and Seidel, E., (1978). The median Aegean crystalline belt: stratigraphy, structure, metamorphism, magmatism, *in* Cloos, H., Roeder, D., and Schmidt, K., eds., Alps, Apennines, Hellenides: *Schweizerbart, Stuttgart*, p. 455–476.

England, P.C., 1978, Some thermal considerations of the Alpine metamorphism, past, present and future: Tectonophysics, v. 46, p. 21–40, https://doi.org/10.1016/0040-1951(78)90103-8.

England, P.C., 1993, Convective removal of thermal boundary layer of thickened continental lithosphere: A brief summary of causes and consequences with special reference to the Cenozoic tectonics of the Tibetan Plateau and surrounding regions: Tectonophysics, v. 223, p. 67–73, https://doi.org/10.1016/0040-1951(93)90158-G.

England, P.C., and Holland, T.J.B., 1979, Archimedes and the Tauern eclogites: The role of buoyancy in the preservation of exotic eclogite blocks: Earth and Planetary Science Letters, v. 44, p. 287–294, https://doi.org/10.1016/0012-821X(79)90177-8.

England, P.C., and Jackson, J., 1987, Migration of the seismic-aseismic transition during uniform and non- uniform extension of the continental lithosphere: Geology, v. 15, p. 291–294, https://doi.org/10.1130/0091-7613(1987)15<291:MOTSTD>2.0.CO;2.

England, P.C., and Richardson, S.W., 1977, The influence of erosion upon the mineral facies of rocks from different metamorphic environments: Journal of the Geological Society, v. 134, p. 201–213, https://doi.org/10.1144/gsjgs.134.2.0201.

England, P.C., and Thompson, A.B., 1984, Pressure–temperature–time paths of regional metamorphism I. Heat transfer during the evolution of regions of thickened continental crust: Journal of Petrology, v. 25, p. 894–928, https://doi.org/10.1093/petrology/25.4.894.

England, P.C., and Houseman, G., 1989, Extension during continental convergence, with application to the Tibetan Plateau: Journal of Geophysical Research, v. 94, B12, p. 17,561–17,579, https://doi.org/10.1029/JB094iB12p17561.

England, P.C., and Molnar, P., 1993a, Cause and effect among thrust and normal faulting, anatectic melting and exhumation in the Himalaya: Geological Society of London, Special Publications, v. 74, p. 401–411, https://doi.org/10.1144/GSL.SP.1993.074.01.27.

England, P.C., and Molnar, P., 1993b. The interpretation of inverted metamorphic isograds using simple physical calculations: Tectonics, v. 12, no. 1, p. 145–157, https://doi.org/10.1029/92TC00850.

England, P.C., Houseman, G., and Nocquet, J.M., 2016. Constraints from GPS measurements on the dynamics of deformation in Anatolia and the Aegean: Journal of Geophysical Research. Solid Earth, v. 121, p. 8888–8916, https://doi.org/10.1002/2016JB013382.

Fletcher, R.C., and Hallet, B., 1983, Unstable extension of the lithosphere: A mechanical model for Basin-and-Range structure: Journal of Geophysical Research, v. 88, p. 7457–7466, https://doi.org/10.1029/JB088iB09p07457.

Forster, M.A., and Lister, G.S., 2005, Several distinct tectono-metamorphic slices in the Cycladic eclogite–blueschist belt, Greece: Contributions to Mineralogy and Petrology, v. 150, no. 5, p. 523–545, https://doi.org/10.1007/s00410-005-0032-9.

Gerya, T., and Stöckhert, B., 2006, Two-dimensional numerical modeling of tectonic and metamorphic histories at active continental margins: International Journal of Earth Sciences, v. 95, p. 250–274, https://doi.org/10.1007/s00531-005-0035-9.

Gerya, T., Stöckhert, B., and Perchuk, A., 2002, Exhumation of high-pressure metamorphic rocks in a subduction channel: a numerical simulation: Tectonics, v. 21, p. 1-19, https://doi.org/10.1029/2002TC001406.

Gorce, J. S., Caddick, M. J., Baxter, E. F., Dragovic, B., Schumacher, J. C., Bodnar, R. J., and Kendall, J. F. (2021). Insight into the early exhumation of the Cycladic Blueschist Unit, Syros, Greece: Combined application of zoned garnet geochronology, thermodynamic modeling, and quartz elastic barometry: Geochemistry, Geophysics, Geosystems, v. 22, e2021GC009716. https://doi.org/10.1029/2021GC009716

Grasemann, B., Schneider, D.A., Stöckli, D.F., and Iglseder, C., 2012, Miocene bivergent crustal extension in the Aegean: Evidence from the western Cyclades (Greece): Lithosphere, v. 4, no. 1, p. 23–39, https://doi.org/10.1130/L164.1.

Grujic, D., Casey, M., Davidson, C., Hollister, L., Kündig, R., Pavlis, T., and Schmid, S., 1996, Ductile extrusion of the higher Himalayan crystalline in Bhutan: evidence from quartz microfabrics: Tectonophysics, v. 260, p. 21–43, https://doi.org/10.1016/0040-1951(96)00074-1.

Gysi, A.P., and Harlov, D., 2021, Hydrothermal solubility of $TbPO_4$, $HoPO_4$, $TmPO_4$, and $LuPO_4$ xenotime endmembers at pH of 2 and temperatures between 100 and 250 °C: Chemical Geology, v. 567, p. 120072, https://doi.org/10.1016/j.chemgeo.2021.120072.

Harrison, T.M., Duncan, I., and McDougall, I., 1985. Diffusion of ^{40}Ar in biotite: temperature, pressure and compositional effects: Geochimica et Cosmochimica Acta, v. 49, p. 2461–2468, https://doi.org/10.1016/0016-7037(85)90246-7.

Harrison, T.M., Célérier, J., Aikman, A.B., Hermann, J., and Heizler, M.T., 2009, Diffusion of ^{40}Ar in muscovite: Geochimica et Cosmochimica Acta, v. 73, p. 1039–1051, https://doi.org/10.1016/j.gca.2008.09.038.

Hermann, J, 2002. Allanite: thorium and light rare earth element carrier in subducted crust. Chemical Geology, v. 192, p. 289–306

Horstwood, M.S.A., Košler, J., Gehrels, G., Jackson, S.E., McLean, N.M., Paton, C., Pearson, N.J., Sircombe, K., Sylvester, P., Vermeesch, P., Bowring, J.F., Condon, D.J., and Schoene, B., 2016, Community-Derived Standards for LA-ICP-MS U-(Th-)Pb Geochronology – Uncertainty Propagation, Age Interpretation and Data Reporting: Geostandards and Geoanalytical Research, v. 40, p. 311–332, https://doi.org/10.1111/j.1751-908X.2016.00379.x.

Huerta, A., Royden, L., and Hodges, K., 1999, The effects of accretion, erosion and radiogenic heat on the metamorphic evolution of collisional orogens: Journal of Metamorphic Geology, v. 17, p. 349–366, https://doi.org/10.1046/j.1525-1314.1999.00204.x.

Huet, B., Labrousse, L., and Jolivet, L., 2009, Thrust or detachment? Exhumation processes in the Aegean: Insight from a field study on Ios (Cyclades, Greece): Tectonics, v. 28, p. TC3007, https://doi.org/10.1029/2008TC002397.

Huet, B., Labrosse, L., Monié, P., Malvoisin, B., and Jolivet, L., 2015, Coupled phengite ^{40}Ar-^{39}Ar geochronology and thermobarometry: PTt evolution of Andros Island (Cyclades, Greece): Geological Magazine, v. 152, no. 4, p. 711, https://doi.org/10.1017/S0016756814000661.

DOI:10.1130/B36332.1

Huismans, R.S., and Beaumont, C., 2014, Rifted continental margins: The case for depth-dependent extension: Earth and Planetary Science Letters, v. 407, p. 148–162, https://doi.org/10.1016/j.epsl.2014.09.032.

Huyskens, M.H., and Bröcker, M., 2014, The status of the Makrotantalon Unit (Andros, Greece) within the structural framework of the Attic-Cycladic Crystalline Belt: Geological Magazine, v. 151, no. 3, p. 430–446, https://doi.org/10.1017/S0016756813000307.

Iglseder, C., Grasemann, B., Schneider, D.A., Petrakakis, K., Miller, C., Klötzli, U.S., et al., 2009, I and S-type plutonism on Serifos (W-Cyclades, Greece): Tectonophysics, v. 473, no. 1–2, p. 69–83, https://doi.org/10.1016/j.tecto.2008.09.021.

Jamieson, R., Beaumont, C., Fullsack, P., and Lee, B., 1998, Barrovian metamorphism: where's the heat?: Geological Society of London Special Publication, v. 138, p. 23–51, https://doi.org/10.1144/GSL.SP.1996.138.01.03.

Jamieson, R.A. and Beaumont, C., 2013. On the origin of orogens. Geological Society of America Bulletin, v. 125(11-12), p.1671-1702.

Janots, E., Brunet, F., Goffé, B., Poinssot, C., Burchard, M., and Cemič, L., 2007, Thermochemistry of monazite-(La) and dissakisite-(La): implications for monazite and allanite stability in metapelites: Contributions to Mineralogy and Petrology, v. 154, p. 1–14, https://doi.org/10.1007/s00410-006-0176-2.

Janots, E., Engi, M., Berger, A., Allaz, J., Schwarz, J.O., and Spandler, C., 2008, Prograde metamorphic sequence of REE minerals in pelitic rocks of the Central Alps: implications for allanite–monazite–xenotime phase relations from 250 to 610 °C: Journal of Metamorphic Geology, v. 26, p. 509–526, https://doi.org/10.1111/j.1525-1314.2008.00774.x.

Janots, E., Engi, M., Rubatto, D., Berger, A., Gregory, C., and Rahn, M., 2009, Metamorphic rates in collisional orogeny from in situ allanite and monazite dating: Geology, v. 37, p. 11–14, https://doi.org/10.1130/G25192A.1.

Jansen, J.B.H., 1973. Geological Map of Greece, Island of Naxos: Athens, Greece, Institute for Geology and Mineral Resources.

Jansen, J.B.H., and Schuiling, R.D., 1976, Metamorphism on Naxos: Petrology and geothermal gradients: American Journal of Science, v. 276, p. 1225–1253, https://doi.org/10.2475/ajs.276.10.1225.

Jaupart, C., Mareschal, J.C., and Iarotsky, L., 2016, Radiogenic heat production in the continental crust: Lithos, v. 262, p. 398–427, https://doi.org/10.1016/j.lithos.2016.07.017.

John, B.E., and Howard, K.A., 1995, Rapid extension recorded by cooling age pattern and brittle deformation, Naxos, Greece: Journal of Geophysical Research, v. 100, p. 9969–9979, https://doi.org/10.1029/95JB00665.

Jolivet, L., and Brun, J.P., 2010, Cenozoic geodynamic evolution of the Aegean region: International Journal of Earth Sciences, v. 99, p. 109–138, https://doi.org/10.1007/s00531-008-0366-4.

Jolivet, L., Famin, V., Mehl, C., Parra, T., Aubourg, C., Hébert, R., and Philippot, P., 2004, Strain localization during crustal-scale boudinage to form extensional metamorphic domes in the Aegean Sea: Geological Society of America. Special Paper, v. 380, p. 185–210, https://doi.org/10.1130/0-8137-2380-9.185.

Jolivet, L., Lecomte, E., Huet, B., Denèle, Y., Lacombe, O., Labrousse, L., Le Pourhiet, L., and Mehl, C., 2010, The north cycladic detachment system: Earth and Planetary Science Letters, v. 289, p. 87–104, https://doi.org/10.1016/j.epsl.2009.10.032.

Katzir, Y., Matthews, A., Garfunkel, Z., Schliestedt, M., and Avigad, D., 1996, The tectono-metamorphic evolution of a dismembered ophiolite (Tinos, Cyclades, Greece): Geological Magazine, v. 133, p. 237–254, https://doi.org/10.1017/S0016756800008992.

Katzir, Y., Avigad, D., Matthews, A., Garfunkel, Z., and Evans, B.W., 1999, Origin and metamorphism of ultrabasic rocks associated with a subducted continental margin, Naxos (Cyclades, Greece): Journal of Metamorphic Geology, v. 17, p. 301–318, https://doi.org/10.1046/j.1525-1314.1999.00197.x.

Keay, S., Lister, G., and Buick, I.S., 2001, The timing of partial melting, Barrovian metamorphism and granite intrusion in the Naxos metamorphic core complex, Cyclades, Aegean Sea, Greece: Tectonophysics, v. 342, p. 275–312, https://doi.org/10.1016/S0040-1951(01)00168-8.

Kelley, S., 2002, Excess argon in K–Ar and Ar–Ar geochronology: Chemical Geology, v. 188, p. 1–22, https://doi.org/10.1016/S0009-2541(02)00064-5.

Kohn, M.J., Castro, A.E., Kerswell, B.C., Ranero, C.R., and Spear, F.S., 2018, Shear heating reconciles thermal models with the metamorphic rock record of subduction: Proceedings of the National Academy of Sciences of the United States of America, v. 115, no. 46, p. 11706–11711, https://doi.org/10.1073/pnas.1809962115.

Koukouvelas, I.K., and Kokkalas, S., 2003, Emplacement of the Miocene west Naxos pluton (Aegean Sea, Greece): A structural study: Geological Magazine, v. 140, p. 45–61, https://doi.org/10.1017/S0016756802007094.

Kruckenberg, S.C., Ferré, E.C., Teyssier, C., Vanderhaeghe, O., Whitney, D.L., Seaton, N.C.A., and Skord, J.A., 2010, Viscoplastic flow in migmatites deduced from fabric anisotropy: an example from the Naxos dome, Greece: Journal of Geophysical Research. Solid Earth, v. 115, p. B09401, https://doi.org/10.1029/2009JB007012.

Kruckenberg, S.C., Vanderhaeghe, O., Ferré, E.C., Teyssier, C., and Whitney, D.L., 2011, Flow of partially molten crust and the internal dynamics of a migmatite dome, Naxos, Greece: Tectonics, v. 30, p. TC3001, https://doi.org/10.1029/2010TC002751.

Kuhlemann, J., Frisch, W., Dunkl, I., Kázmér, M., and Schmiedl, G., 2004, Miocene siliciclastic deposits of Naxos Island: geodynamic and environmental implications for the evolution of the southern Aegean Sea (Greece): Geological Society of America. Special Paper, v. 378, p. 51–65, https://doi.org/10.1130/0-8137-2378-7.51.

Kumar, A., Lal, N., Jain, A.K., and Sorkhabi, R.B., 1995, Late Cenozoic-Quarternary thermo-tectonic history of Higher Himalaya Crystalline (HHC) in Kishtwar-Padar-Zanskar region, NW Himalaya: evidence from fission track ages: Journal of the Geological Society of India, v. 45, p. 375–391.

Lagos, M., Scherer, E.E., Tomaschek, F., Münker, C., Keiter, M., Berndt, J., and Ballhaus, C., 2007, High precision Lu-Hf geochronology of Eocene eclogite-facies rocks from Syros, Cyclades, Greece: Chemical Geology, v. 243, p. 16–35, https://doi.org/10.1016/j.chemgeo.2007.04.008.

Lamont, T.N., (2018). Unravelling the structural, metamorphic and strain history of the" Aegean Orogeny", Southern Greece with a combined structural, petrographic and geochronological approach. *D.Phil Thesis*, University of Oxford.

Lamont, T.N., Searle, M.P., Waters, D.J., Roberts, N.M., Palin, R.M., Smye, A., Dyck, B., Weller, O.M., and St-Onge, M.R., 2019, Compressional origin of the Naxos metamorphic core complex, Greece: Structure, petrography, and thermobarometry: Geological Society of America Bulletin, v. 132, no. 1–2, p. 149–197.

Lamont, T. N., Roberts, N. M., Searle, M. P., Gopon, P., Waters, D. J., and Millar, I. (2020a). The age, origin, and emplacement of the Tsiknias Ophiolite, Tinos, Greece: Tectonics, v. *39*(1), e2019TC005677.

Lamont, T. N., Searle, M. P., Gopon, P., Roberts, N. M., Wade, J., Palin, R. M., and Waters, D. J. (2020b). The Cycladic Blueschist Unit on Tinos, Greece: Cold NE-subduction and SW-directed extrusion of the Cycladic continental margin under the Tsiknias Ophiolite: Tectonics, v. *39*(9), e2019TC005890.

Laurent, V., Jolivet, L., Roche, V., Augier, R., Scaillet, S., Cardello, G.L., et al., 2016, Strain localization in a fossilized subduction channel: Insights from the Cycladic Blueschist Unit (Syros, Greece): Tectonophysics, v. 672–673, p. 150–169, https://doi.org/10.1016/j.tecto.2016.01.036.

Laurent, V., Lanari, P., Naïr, I., Augier, R., Lah'd, A., and Jolivet, L., 2018, Exhumation of eclogite and blueschist (Cyclades, Greece): Pressure–temperature evolution determined by thermobarometry and garnet equilibrium modelling. *Journal of Metamorphic Geology*,

Lee, J., Hacker, B.R., Dinklage, W.S., Wang, Y., Gans, P., Calvert, A., Wan, J., Chen, W., Blythe, A.E., and McClelland, W., 2000. Evolution of the Kangmar Dome, southern Tibet: Structural, petrologic, and thermochronologic constraints: Tectonics, v. 19, no. 5, p. 872–895.

Lee, J., Hacker, B., and Wang, Y., 2004, Evolution of North Himalayan gneiss domes: structural and metamorphic studies in Mabja Dome, southern Tibet: Journal of Structural Geology, v. 26, no. 12, p. 2297–2316, https://doi.org/10.1016/j.jsg.2004.02.013.

Lee, J., McClelland, W., Wang, Y., Blythe, A., and McWilliams, M., 2006, Oligocene-Miocene middle crustal flow in southern Tibet: geochronology of Mabja Dome: Geological Society of London, Special Publications, v. 268, no. 1, p. 445–469, https://doi.org/10.1144/GSL.SP.2006.268.01.21.

Lister, G.S., and Forster, M.A., 2016, White mica ^{40}Ar/^{39}Ar age spectra and the timing of multiple episodes of high-*P* metamorphic mineral growth in the Cycladic eclogite–blueschist belt, Syros, Aegean Sea, Greece: Journal of Metamorphic Geology, v. 34, p. 401–421, https://doi.org/10.1111/jmg.12178.

Lister, G.S., Banga, G., and Feenstra, A., (1984). Metamorphic core complexes of cordilleran type in the Cyclades, Aegean Sea, Greece: Geology, v. 12, p. 221–225, https://doi.org/10.1130/0091-7613(1984)12<221:MCCOCT>2.0.CO;2.

Lyubetskaya, T., and Ague, J., 2010, Modeling metamorphism in collisional orogens intruded by magmas: I. Thermal evolution: American Journal of Science, v. 310, p. 427, https://doi.org/10.2475/06.2010.01.

Maluski, H., Bonneau, M., and Kienast, J.R., 1987, Dating the metamorphic events in the Cycladic area: ^{39}Ar/^{40}Ar data from metamorphic rocks of the island of Syros (Greece): Bulletin de la Société Géologique de France, v. III(5), p. 833–842, https://doi.org/10.2113/gssgfbull.III.5.833.

Mancktelow, N., Zwingmann, H., and Mulch, A., 2016, Timing and conditions of clay fault gouge formation on the Naxos detachment (Cyclades, Greece): Tectonics, v. 35, p. 2334–2344, https://doi.org/10.1002/2016TC004251.

Martin, L., Duchêne, S., Deloule, E., and Vanderhaeghe, O., 2006, The isotopic composition of zircon and garnet: A record of the metamorphic history of Naxos, Greece: Lithos, v. 87, p. 174–192, https://doi.org/10.1016/j.lithos.2005.06.016.

Means, W.D., (1989). Stretching faults: Geology, v. 17, p. 893–896, https://doi.org/10.1130/0091-7613(1989)017<0893:SF>2.3.CO;2

Menant, A., Jolivet, L., Augier, R., and Skarpelis, N., 2013, The North Cycladic Detachment System and associated mineralization, Mykonos, Greece: Insights on the evolution of the Aegean domain: Tectonics, v. 32, p. 433–452, https://doi.org/10.1002/tect.20037.

Molnar, P., and England, P., 1990, Temperatures, heat flux, and frictional stress near major thrust faults: Journal of Geophysical Research. Solid Earth, v. 95, B4, p. 4833–4856, https://doi.org/10.1029/JB095iB04p04833.

Montel, J.M., 2000. Preservation of old U-Th-Pb ages in shielded monazite; example from the Beni Bousera Hercynian kinzigites (Morocco). Journal of metamorphic geology., v. 18, p. 335-342.

Oberli F, Meier M, Berger A, Rosenberg C, Gieré R, 2004. U-Th-Pb and 230Th/238U disequilibrium isotope systematics: precise accessory mineral chronology and melt evolution tracing in the Alpine Bergell intrusion. Geochemica Cosmochimca Acta

Oxburgh, E., and Turcotte, D., 1974, Thermal gradients and regional metamorphism in overthrust terrains with special reference to the Eastern Alps. Schweiz. Mineral. Patrogr. Mitt.; Schweiz; v. 54, p. 642–662.

Parra, T., Vidal, O., and Jolivet, L., 2002. Relation between the intensity of deformation and retrogression in blueschist metapelites of Tinos Island (Greece) evidenced by chlorite–mica local equilibria: Lithos, v. 63, p. 41–66, https://doi.org/10.1016/S0024-4937(02)00115-9.

Patzak, M., Okrusch, M., and Kreuzer, H., 1994, The Akrotiri unit on the island of Tinos, Cyclades, Greece: witness to a lost terrane of Late Cretaceous age: Neues Jahrbuch für Geologie und Paläontologie. Abhandlungen, v. 194, p. 211–252, https://doi.org/10.1127/njgpa/194/1994/211.

Papanikolaou, D.J., 1984, The three metamorphic belts of the Hellenides: a review and a kinematic interpretation: Geological Society of London, Special Publications, v. 17, no. 1, p. 551–561, https://doi.org/10.1144/GSL.SP.1984.017.01.42.

Peillod, A., Ring, U., Glodny, J., and Skelton, A., 2017, An Eocene/Oligocene blueschist/greenschist-facies *P-T* loop from the Cycladic Blueschist Unit on Naxos Island, Greece: Deformation-related reequilibration vs thermal relaxation: Journal of Metamorphic Geology, v. 35, p. 805–830, https://doi.org/10.1111/jmg.12256.

Peillod, A., Majka, J., Ring, U., Drüppel, K., Patten, C., Karlsson, A., Włodek, A., and Tehler, E., 2021a, Differences in decompression of a high-pressure unit: A case study from the Cycladic Blueschist Unit on Naxos Island, Greece: Lithos, v. 386-387, p. 106043, https://doi.org/10.1016/j.lithos.2021.106043.

Peillod, A., Tehler, E., and Ring, U., 2021b, Quo vadis Zeus-Is there a Zas shear zone on Naxos Island, Aegean Sea, Greece? A review of metamorphic history and new kinematic data: Journal of the Geological Society, v. 178, https://doi.org/10.1144/jgs2020-217.

Philippon, M., Brun, J.-P., and Gueydan, F., 2011, Tectonics of the Syros blueschists (Cyclades, Greece): From subduction to Aegean extension: Tectonics, v. 30, p. TC4001, https://doi.org/10.1029/2010TC002810.

Platt, J.P., 1993. Exhumation of high-pressure rocks: A review of concepts and processes. Terra nova, v. 5(2), p.119-133.

Platt, J. and England, P., 1994. Convective removal of lithosphere beneath mountain belts-Thermal and mechanical consequences. American Journal of Science, v. 294(3).

DOI:10.1130/B36332.1

Platt, J.P., Behr, W., and Cooper, F.J., 2015, Metamorphic core complexes: Windows into the mechanics and rheology of the crust [London]: Journal of the Geological Society, v. 172, p. 9–27, https://doi.org/10.1144/jgs2014-036.

Putlitz, B., Cosca, M.A., and Schumacher, J.C., 2005, Prograde mica $^{40}Ar/^{39}Ar$ growth ages recorded in high pressure rocks (Syros, Cyclades, Greece): Chemical Geology, v. 214, p. 79–98, https://doi.org/10.1016/j.chemgeo.2004.08.056.

Rey, P.F., Mondy, L., Duclaux, G., Teyssier, C., Whitney, D.L., Bocher, M., and Prigent, C., 2017, The origin of contractional structures in extensional gneiss domes: Geology, v. 45, p. 263–266, https://doi.org/10.1130/G38595.1.

Rey, P., Teyssier, C., and Whitney, D.L., 2009. The role of partial melting and extensional strain rates in the development of metamorphic core complexes: Tectonophysics, v. 477, p. 135–144, 10.1016/j.tecto.2009. 03.010.

Rey, P.F., Teyssier, C., Kruckenberg, S.C., and Whitney, D.L., 2011, Viscous collision in channel explains double domes in metamorphic core complexes: Geology, v. 39, p. 387–390, https://doi.org/10.1130/G31587.1.

Ring, U., and Layer, P. W., 2003. High-pressure metamorphism in the Aegean, eastern Mediterranean: Underplating and exhumation from the Late Cretaceous until the Miocene to Recent above the retreating Hellenic subduction zone: Tectonics, v. 22, p. 1022, doi:https://doi.org/10.1029/2001TC001350, 3.

Ring, U., Thomson, S.N., and Bröcker, M., 2003, Fast extension but little exhumation: the Vari detachment in the Cyclades, Greece: Geological Magazine, v. 140, no. 3, p. 245–252, https://doi.org/10.1017/S0016756803007799.

Ring, U., Glodny, J., Will, T.M. and Thomson, S., 2011. Normal faulting on Sifnos and the south cycladic detachment system, Aegean Sea, Greece. Journal of the Geological Society, v. 168(3), p. 751–768.

Ring, U., Glodny, J., Peillod, A., and Skelton, A., 2018. The timing of high-temperature conditions and ductile shearing in the footwall of the Naxos extensional fault system, Aegean Sea, Greece: Tectonophysics, v. 745, p. 366–381, https://doi.org/10.1016/j.tecto.2018.09.001.

Ring, U., Pantazides, H., Glodny, J., and Skelton, A., 2020. Forced return flow deep in the subduction channel, Syros, Greece: *Tectonics*, v. 39, e2019TC005768. https://doi.org/10.1029/2019TC005768

Royden, L., 1996. Coupling and decoupling of crust and mantle in convergent orogens: Implications for strain partitioning in the crust: Journal of Geophysical Research, v. 101, B8, p. 17679–17705, https://doi.org/10.1029/96JB00951.

Royden, L., and Keen, C.E., 1980, Rifting process and thermal evolution of the continental margin of eastern Canada determined from subsidence curves: Earth and Planetary Science Letters, v. 51, no. 2, p. 343–361, https://doi.org/10.1016/0012-821X(80)90216-2.

Ruppel, C., Royden, L., and Hodges, K.V., 1988. Thermal modeling of extensional tectonics: Application to pressure-temperature-time histories of metamorphic rocks: Tectonics, v. 7, p. 947–957, https://doi.org/10.1029/TC007i005p00947.

Ryan, P.D., and Dewey, J.F., 2019, The sources of metamorphic heat during collisional orogeny: the Barrovian enigma: Canadian Journal of Earth Sciences, v. 56, no. 12, p. 1309–1317, https://doi.org/10.1139/cjes-2018-0182.

Ryb, U., Lloyd, M.K., Stolper, D.A., and Eiler, J.M., 2017, The clumped-isotope geochemistry of exhumed marbles from Naxos, Greece: Earth and Planetary Science Letters, v. 470, p. 1–12, https://doi.org/10.1016/j.epsl.2017.04.026.

Sandiford, M., and Powell, R., 1986, Deep crustal metamorphism during continental extension: modern and ancient examples: Earth and Planetary Science Letters, v. 79, p. 151–158, https://doi.org/10.1016/0012-821X(86)90048-8.

Searle, M.P., 2010, Low-angle normal faults in the compressional Himalayan orogen; Evidence from the Annapurna–Dhaulagiri Himalaya, Nepal: Geosphere, v. 6, p. 296–315, https://doi.org/10.1130/GES00549.1.

Searle, M.P., and Lamont, T.N., 2020, Compressional metamorphic core complexes, low-angle normal faults and extensional fabrics in compressional tectonic settings: Geological Magazine, v. 157, no. 1, p. 101–118, https://doi.org/10.1017/S0016756819000207.

Searle, M.P., and Lamont, T.N., 2022, Compressional origin of the Aegean Orogeny, Greece: Geoscience Frontiers, https://doi.org/10.1016/j.gsf.2020.07.008.

Seward, D., Vanderhaeghe, O., Siebenaller, L., Thomson, S., Hibsch, C., Zingg, A., et al., (2009). Cenozoic tectonic evolution of Naxos Island through a multi-faceted approach of fission-track analysis. The Geological Society of London, Special Publications, v. 312, p. 179–196.

Skelton, A., Peillod, A., Glodny, J., Klonowska, I., Månbro, C., Lodin, K., and Ring, U., 2019, Preservation of high-P rocks coupled to rock composition and the absence of metamorphic fluids: Journal of Metamorphic Geology, v. 37, p. 359–381, https://doi.org/10.1111/jmg.12466.

Smye, A.J., Roberts, N.M.W., Condon, D.J., Horstwood, M.S.A., and Parrish, R.R., 2014, Characterising the U–Th–Pb systematics of allanite by ID and LA-ICPMS: Implications for geochronology: Geochimica et Cosmochimica Acta, v. 135, p. 1–28, https://doi.org/10.1016/j.gca.2014.03.021.

Smye, A.J., Bickle, M.J., Holland, T.J.M., Parrish, R.R., and Condon, D.J., 2011, Rapid formation and exhumation of the youngest Alpine eclogites: A thermal conundrum to Barrovian metamorphism: Earth and Planetary Science Letters, v. 306, p. 193–204, https://doi.org/10.1016/j.epsl.2011.03.037.

Smye, A.J., Lavier, L.L., Zack, Z., and Stockli, D.F., 2019, Episodic heating of continental lower crust during extension: A thermal modeling investigation of the Ivrea-Verbano Zone: Earth and Planetary Science Letters, v. 521, p. 158–168, https://doi.org/10.1016/j.epsl.2019.06.015.

Soukis, K., and Stockli, D.F., 2013, Structural and thermochronometric evidence for multi-stage exhumation of southern Syros, Cycladic, islands, Greece: Tectonophysics, v. 595–596, p. 148–164, https://doi.org/10.1016/j.tecto.2012.05.017.

Spear, F.S., 2010. Monazite–allanite phase relations in metapelites: Chemical Geology, v. 279.1–2, p. 55–62.

Spear, F.S., and Peacock, S.M., 1989. Thermal Modeling of Metamorphic Pressure-Temperature-Time Paths: a Forward Approach. *in* Metamorphic Pressure-Temperature-Time Paths (eds F.S. Spear and S.M. Peacock). https://doi.org/10.1029/SC007p0001

Stöckhert, B., 2002. Stress and deformation in subduction zones: insight from the record of exhumed metamorphic rocks. In: De Meer, S., Drury, M.R., De Bresser, J.H.P., Pennock, G.M. (Eds.), Current issues and new developments in deformation mechanisms, rheology

DOI:10.1130/B36332.1

and tectonics, Geological Society London Special Publication, London, v. 200, https://doi.org/10.1144/GSL.SP.2001.200.01.15.

Stöckhert, B., Massonne, H., and Nowlan, E., 1997, Low differential stress during high- pressure metapelite from the Eclogite Zone, Tauern Window, Eastern Alps: Lithos, v. 41, p. 103–118, https://doi.org/10.1016/S0024-4937(97)82007-5.

Stouraiti, C., Pantziris, I., Vasilatos, C., Kanellopoulos, C.P., Mitropoulos, P., Pomonis, P., Moritz, R., and Chiaradia, M., 2017, Ophiolitic Remnants from the Upper and Intermediate Structural Unit of the Attic-Cycladic Crystalline Belt (Aegean, Greece): Fingerprinting Geochemical Affinities of Magmatic Precursors: Geosciences, v. 7, p. 14, https://doi.org/10.3390/geosciences7010014.

Stüwe, K., and Sandiford, M., 1995, Mantle-lithospheric deformation and crustal metamorphism with some speculations on the thermal and mechanical significance of the Tauern Event, Eastern Alps: Tectonophysics, v. 242, p. 115–132, https://doi.org/10.1016/0040-1951(94)00156-4.

Teyssier, C. and Whitney D.L. (2002). Gneiss domes and orogeny: Geology, v. 30, p. 1139–1142, https://doi.org/10.1130/0091-7613(2002)030<1139:GDAO>2.0.CO;2.

Tirel, C., Gueydan, F., Tiberi, C., and Brun, J.P., 2004, Aegean crustal thickness inferred from gravity inversion. Geodynamical implications: Earth and Planetary Science Letters, v. 228, no. 3–4, p. 267–280, https://doi.org/10.1016/j.epsl.2004.10.023.

Tomaschek, F., Kennedy, A.K., Villa, I.M., Lagos, M., and Ballhaus, C., 2003, Zircons from Syros, Cyclades, Greece—Recrystallization and Mobilization of Zircon During High-Pressure Metamorphism: Journal of Petrology, v. 44, p. 1977–2002, https://doi.org/10.1093/petrology/egg067.

Urai, J.L., Schuiling, R.D., and Jansen, J.B.H., (1990). Alpine deformation on Naxos (Greece), *in* Knipe, R.J., and Rutter, E.H., eds., Deformation Mechanisms, Rheology and Tectonics: Geological Society of London Special Publication, v. 54, p. 509–522.

Uunk, B., Brouwer, F., Paz-Álvarez, M., van Zuilen, K., Huybens, R., van ’t Veer, R., and Wijbrans, J., 2022, Consistent detachment of supracrustal rocks from a fixed subduction depth in the Cyclades: Earth and Planetary Science Letters, v. 584, p. 117479, https://doi.org/10.1016/j.epsl.2022.117479.

Vandenberg, L.C. and Lister, G.S., 1996. Structural analysis of basement tectonites from the Aegean metamorphic core complex of Ios, Cyclades, Greece. Journal of Structural Geology, v. 18(12), p.1437-1454.

Vanderhaeghe, O., 2004, Structural development of the Naxos migmatite dome: Geological Society of America. Special Paper, v. 380, p. 211–227, https://doi.org/10.1130/0-8137-2380-9.211.

Vanderhaeghe, O., and Teyssier, C., 2001, Partial melting and flow of orogens: Tectonophysics, v. 342, p. 451–472, https://doi.org/10.1016/S0040-1951(01)00175-5.

Vanderhaeghe, O., Kruckenberg, S.C., Gerbault, M., Martin, L., Duchêne, S., and Deloule, E., 2018, Crustal-scale convection and diapiric upwelling of a partially molten orogenic root (Naxos dome, Greece): Tectonophysics, v. 746, p. 459–469, https://doi.org/10.1016/j.tecto.2018.03.007.

Van Hinsbergen, D.J., Torsvik, T.H., Schmid, S.M., Maţenco, L.C., Maffione, M., Vissers, R.L., Gürer, D. and Spakman, W., 2020. Orogenic architecture of the Mediterranean region and kinematic reconstruction of its tectonic evolution since the Triassic. Gondwana Research, 81, p.79-229.

Vermeesch, P., 2018, IsoplotR: a free and open toolbox for geochronology: Geoscience Frontiers, v. 9, p. 1479–1493, https://doi.org/10.1016/j.gsf.2018.04.001.

Vermeesch, P., 2020, Unifying the U–Pb and Th–Pb methods: joint isochron regression and common Pb correction: Geochronology, v. 2, p. 119–131, https://doi.org/10.5194/gchron-2-119-2020.

Virgo, S., von Hagke, C., and Urai, J.L., 2018, Multiphase boudinage: A case study of amphibolites in marble in the Naxos migmatite core: Solid Earth, v. 9, p. 91–113, https://doi.org/10.5194/se-9-91-2018.

von Hagke, C., Bamberg, B., Virgo, S., and Urai, J.L., 2018, Outcrop-scale tomography: Insights into the 3D structure of multiphase boudins: Journal of Structural Geology, v. 115, p. 311–317, https://doi.org/10.1016/j.jsg.2018.02.014.

Warren, C., Beaumont, C., and Jamieson, R., 2008, Deep subduction and rapid exhumation: role of crustal strength and strain weakening in continental subduction and ultrahigh-pressure rock exhumation: Tectonics, v. 27, p. 28, https://doi.org/10.1029/2008TC002292.

Warren, C.J., Hanke, F., and Kelley, S.P., 2012, When can muscovite $^{40}Ar/^{39}Ar$ dating constrain the timing of metamorphic exhumation?: Chemical Geology, v. 291, p. 79–86, https://doi.org/10.1016/j.chemgeo.2011.09.017.

Waters, D.J., 1990. Thermal history and tectonic setting of the Namaqualand granulites, southern Africa: clues to Proterozoic crustal development. In Granulites and Crustal evolution (p. 243-256). Springer, Dordrecht.

Weller, O.M., St-Onge, M.R., Waters, D.J., Rayner, N., Searle, M.P., Chung, S.-L., Palin, R.M., Lee, Y.-H., and Xu, X., 2013, Quantifying Barrovian metamorphism in the Danba Structural Culmination of eastern Tibet: Journal of Metamorphic Geology, v. 31, p. 909–935, https://doi.org/10.1111/jmg.12050.

Wells, P.R.A., 1980, Thermal models for the magmatic accretion and subsequent metamorphism of continental crust: Earth and Planetary Science Letters, v. 46, p. 253–265, https://doi.org/10.1016/0012-821X(80)90011-4.

Wernicke, B., 1981, Low-angle normal faults in the Basin and Range Province: Nappe tectonics in an extending orogeny: Nature, v. 291, p. 645–648, https://doi.org/10.1038/291645a0.

Wernicke, B., 1985, Uniform normal-sense simple shear of the continental lithosphere: Canadian Journal of Earth Sciences, v. 22, p. 108–125, https://doi.org/10.1139/e85-009.

Whittington, A., Hofmeister, A., and Nabelek, P., 2009, Temperature-dependent thermal diffusivity of the Earth's crust and implications for magmatism: Nature, v. 458, p. 319–321, https://doi.org/10.1038/nature07818.

Wijbrans, J.R., and McDougall, I., 1986, $^{40}Ar/^{39}Ar$ dating of white micas from an Alpine high-pressure metamorphic belt on Naxos (Greece): the resetting of the argon isotopic system: Contributions to Mineralogy and Petrology, v. 93, no. 2, p. 187–194, https://doi.org/10.1007/BF00371320.

Wijbrans, J.R., and McDougall, I., 1988, Metamorphic evolution of the Attic Cycladic Metamorphic Belt on Naxos (Cyclades, Greece) utilizing 40Ar/39Ar age spectrum measurements: Journal of Metamorphic Geology, v. 6, no. 5, p. 571–594, https://doi.org/10.1111/j.1525-1314.1988.tb00441.x.

Wijbrans, J.R., Schliestedt, M., and York, D., 1990, Single grain argon laser probe dating of phengites from the blueschist to greenschist transition on Sifnos (Cyclades Greece): Contributions to Mineralogy and Petrology, v. 104, p. 582–593, https://doi.org/10.1007/BF00306666.

DOI:10.1130/B36332.1

Wing, B., Ferry, J.M, Harrison, T.M, 2003. Prograde destruction and formation of monazite and allanite during contact and regional metamorphism of pelites: petrology and geochronology. Contributions to Mineralogy and Petrology, v. 145, p. 228–250.

Yin, A., 1991. Mechanisms for the formation of domal and basinal detachment faults: A three-dimensional analysis. Journal of Geophysical Research: Solid Earth, v. 96(B9), p.14577–14594.

FIGURES AND TABLES

Figure 1. Schematic cartoons illustrating various tectonic models and pressure-temperature-time (*P–T–t*) paths associated with the formation of metamorphic core complexes (MCCs) (after Lamont et al., 2019; Weller et al., 2013). The cogenetic suite of *P–T–t* paths is shown for three samples (A, B, and C), where the *P–T* loci of their respective *T*-max positions define the metamorphic field gradient, which is typically concave to the *T*-axis, polychronic, and at a steep angle to the *P–T* paths of an individual sample (England and Richardson, 1977; England and Thompson, 1984; Spear and Peacock, 1989): (A) Classical cordilleran-style MCC formed by simple shear extreme depth-dependent extension of the entire continental lithosphere and unroofing under a low-angle normal fault (e.g., Basin and Range). Predicted *P–T–t* path follows an isobaric heating excursion due to increased asthenospheric heating and minimal exhumation. BDT—brittle-ductile transition. (B) Compressional-type MCCs formed by doming above a thrust ramp at depth coeval with exhumation under a passive-roof normal fault (e.g., North Himalayan gneiss domes), associated with a clockwise Barrovian type *P–T–t* path due to conductive relaxation of isotherms following overthrusting.

Figure 2. Tectonic map of the Attic-Cycladic Massif (ACM) showing the distribution of geological units on each Cycladic Island and summary of geochronology (after Lamont et al., 2020b). NCDS = North Cycladic Detachment System, NPDS = Naxos-Paros Detachment System and WCDS = West Cycladic Detachment System. Geochronology data from: (1) Bolhar et al., (2010); (2) Brichau et al., (2008); (3) Keay et al., (2001); (4) Brichau et al., (2007); (5) Iglseder et al., (2009); (6) Matsuda et al., (1999; ^{40}Ar–^{39}Ar volcanics), (7) Beauodin et al., 2015; (9) Lamont, (2018); (10) Lamont et al., (2020a); (11) Huet et al., 2015; (12) Lagos et al., (2007); (13) Tomaschek et al., (2003); (14) Bulle et al., (2010); (15) Bröcker et al., (1993); (17) Dragovic et al., (2012); (16) Peillod et al., (2017); (17) Dragovic et al., (2012); (18) Bröcker et al., (2013); (19) Lister and Forster, 2016); (20) Gorce et al., (2021).

Figure 3. Geological map of Naxos metamorphic core complex and cross sections after Lamont et al., (2019), showing sample locations and available geochronology from this study and the literature. Data from (1) Peillod et al., (2017) (Rb–Sr); (2) Duchêne et al., (2006) (Rb–Sr); (3) Bolhar et al., (2017), (U–Pb); (4) Keay et al., (2001) (U–Pb); (5) Ring et al., (2018), (Rb–Sr); (6) Seward et al., (2009) (Zircon and Apatite fission track); (7) Martin et al., (2006), (U–Pb); Vanderhaeghe et al., (2018), (U–Pb).

Figure 4. A) *P–T–t* evolution of Naxos using constraints from Lamont et al., (2019), age distributions with structural depth on Naxos and temperature time evolution for the Zas Unit, Koronos Unit and Core Units. A) *P–T–t* paths of the Naxos metamorphic core complex showing two distinct clockwise *P–T–t* loops; 1) A *HP–LT* loop that is associated with subduction of the leading edge of the continental margin and affects solely the Zas Unit. 2) A Barrovian type clockwise *P–T* loop that requires crustal thickening to cause peak M_2 conditions at 15 Ma, followed by near isothermal decompression to M_3 sillimanite grade conditions and migmatite dome formation. B) Summary time chart integrating the new data with existing geochronology across the Cyclades and time chart summarizing the timing of deformation and metamorphism

DOI:10.1130/B36332.1

within the Naxos MCC. Age data from, (1) Lamont et al., (2020a), (2) Patzak et al., (1994), (3) Bulle et al., 2010; (4) Bröcker and Enders, (1999); (5) Lamont, (2018); (6) Bröcker et al., (1993); (7) Bröcker et al., (2013); (8) Bröcker et al., (2004); (9) Tomaschek et al., (2003); (10) Lagos et al., (2007); (11) Putlitz et al., (2005); (12) (13) Dragovic et al., (2012); (14) Lister and Forster, (2016); (15) Seward et al., (2009); (16) Peillod et al., (2017); (17) Bolhar et al., (2017); (18) Keay et al., (2001); (19) Cliff et al., (2017); (20) Maluski et al., (1987) (21) Andriessen et al., (1979), (22) Wijbrans and McDougall, (1986); (19) Brichau et al., (2006); (24) Bröcker and Franz, (2006); (25) Huyskens and Bröcker, (2014); (26) Huet et al., (2015); (27) Skelton et al., (2019); (28) Ring et al., (2018) Altherr et al., 1979; (29) Wijbrans et al., (1990); (30) Forster and Lister (2005); (31) Ring et al., (2011); (32) Ring and Layer, (2003); (33) Soukis and Stockli, (2013); (34) Dragovic et al., (2015); (35) Gorce et al., (2021); (36) Uunk et al., (2022).

Figure 5. Photomicrographs of Zas Unit samples showing key microstructures and M_1 blueschist and M_2 greenschist-facies assemblages, and backscattered electron (BSE) imagining of allanite. A) TLN54 plane polarized light (PPL) image showing glaucophane, phengite and rutile defining L_1 and are aligned with the S_1 fabric that is partially folded in matrix domains by S_2. B) TLN54 BSE image showing Allanites aligned with S_1 that is affected by S_2, but both of which are cut by a magnetite grain. C–D) BSE image of TLN54 allanite aligned with S_1 in low strained domains defining L_1. E) Retrograde chlorite cross cutting S_1/ L_1 defined by glaucophane in TLN54. F) Greenschist facies S_2 fabric affected by cm-scale folding in TLN26. G–H) Xenotime and allanite aligned with folded greenschist facies S_2 fabric in TLN26. I) S_3 S–C' top-to-NNE shear fabric cross-cutting greenschist-facies assemblages in TLN26. J) Allanite aligned with biotite bearing S_2 foliations in TLN26. K) Allanite cores in clinozoisite in TLN30, aligned with pervasive S_1 fabric. L) Glaucophane, rutile, paragonite inclusion trails in retrograde epidote wrapped by S_3 in TLN26. M) Transitional blueschist-greenschist facies S_1 fabric isoclinally folded around clinozoisite in TLN30 with top-to-NE shearing around clinozoisite in the bottom limb. N) Matrix allanite aligned with pervasive S_1 in TLN30.

Figure 6. U–(Th)–Pb geochronology results from Zas Unit allanite and xenotime, presented on Tera-Wasserburg diagrams. A) TLN54 Allanite, B) inset TLN54 Xenotime, C) TLN26 Allanite, D) inset TLN26 Xenotime, E) TLN30 Allanite.

Figure 7. A) Summary of age distributions with literature from the Zas Unit showing the new M_1 blueschist-facies U–Pb ages are significantly younger than ca. 40.5–38.3 Ma estimate of M_1 from Rb–Sr and a prolonged period of M_2 greenschist conditions. B) Age distributions with approximate depth beneath the NPDS, showing a step function with Oligocene cooling at high structural levels in the Zas Unit and younger late Miocene cooling at deeper levels suggesting the metamorphic sequence is not a continuous succession. C–F) Temperature-time cooling histories for the Zas Unit, Koronos Unit and Core Unit and compilation of data from all three units (F), showing all units experienced accelerated cooling after 15 Ma.

Figure 8. Competing tectonic and thermal models for Naxos MCC. Model 1) Peillod et al., (2021a,b) stage 1) attempted subduction of the CBU at ca. 40 Ma causing M_1affecting both the Zas and Koronos Units followed by extrusion of the CBU toward the SW from the subduction zone and tectonic emplacement above the Core Unit (stage 2). Stages 3 and 4) Onset of extension at ca. 25 Ma resulting in M_2 isobaric heating and formation of the migmatite dome at the deepest levels and passive exhumation of the MCC beneath the NPDS without significant displacements between the different tectono-metamorphic units. Note the Barrovian isograds in this model should have a lengthscale of 10's km. Predicted *P–T–t* path shows both the Koronos and Zas Units undergoing M_1 at ca. 40 Ma before being reincorporated into the Barrovian M_2

cycle following overthrusting above the Core Unit and the onset of extension at ca. 25 Ma causing isobaric heating. Model 2) Lamont et al., (2019), stage 1) attempted subduction of the CBU (only Zas Unit) at ca. 50 Ma causing M1, followed by extrusion toward the SW and overthrusting above the Koronos and Core Units (Stage 2) by ca. 40 Ma. Stage 3) Continued crustal thickening and conductive relaxation of isotherms causing M_2 Barrovian heating in the Koronos and Core Units that reach anatectic conditions at ca. 20 Ma, causing syn-orogenic extrusion of the Koronos and Core Units beneath top-to-NE passive roof shear zones (ZSZ and KSZ) resulting in isothermal decompression and telescoping of M_2 Barrovian isograds. Stage 4) Onset of extension at ca. 15 Ma causing exhumation and cooling of the MCC beneath the NPDS which cuts the previous shear fabrics. Predicted *P–T–t* path shows only the Zas Unit reached HP conditions at ca. 50 Ma and was overthrusted onto the Koronos and Core Units causing the onset of M_2 Barrovian heating between ca. 40–20 Ma. Thermal climax (M_2-M_3 occurs at ca. 20–15 Ma) in the deepest levels (Core Unit) which experience isothermal decompression due to syn-orogenic extrusion before the onset of extension which causes the onset of rapid cooling and exhumation of all structural levels.

Figure 9. Overthrust 1-D thermal model setup, linking tectonic stages and timing of metamorphism using new geochronology constraints to 1-D thermal modeling conditions and model outputs for the geotherm evolution and *P–T–t* paths overlaid on top of existing *P-T* data. A) Schematic carton model showing the tectonic insertion of the CBU (Zas Unit) nappe between the Upper Cycladic Nappe and the proximal Adriatic continental margin (Koronos and Core Units) and location of the modeled 1-D depth section of interest, close to the inception of overthrusting (and representing Naxos MCC). B) Model geotherm evolution assuming instantaneous overthrusting of the CBU nappe at 50 Ma, until 15 Ma. Each line represents a time interval of 5 Myr. C) Geotherm evolution in *P–T* space, with overlayed thermobarometric estimates for M_1, M_2 and M_3 conditions on Naxos (Buick and Holland, 1989; Lamont et al., 2019; Peillod et al., 2017, 2021a). D) Model *P–T–t* path output for present day following overthrusting at 50 Ma for Thr = 30 km, V_{er} = 0.3 km.Myr^{-1} and radiogenic D-spacing of 12 km for samples initially buried at 25–45 km depth. E) Temperature-time thermal evolution for samples in (D) showing the diachronos nature of peak metamorphic conditions being reached at different times. F–I) Model *P–T–t* paths for Naxos MCC for same condition as (D) for time slices at F) 50 Ma, G) 38 Ma, H) 27 Ma and I) 15 Ma, with overlayed thermobarometric and geochronology constraints for M_1, M_2 and M_3.

Figure 10. Overthrust parameter space results. A Box plots showing the temperature obtained at 15 Ma for a sample initially buried to 45 km depth at 50 Ma with variable Thr, radiogenic D-spacing and V_{er}. Thermobarometric constraints are best satisfied for Thr = 30 km and D-spacing of ~12 km at erosion rates <0.3km.Myr^{-1}. B) Parameter space plot showing maximum temperature obtained for a sample initially buried at 40 km depth with varying erosion rates V_{er}. C–D) Temperature-time thermal evolution plots for a sample initially buried at 45 km depth with Thr = 30 km with C) variable radiogenic D-spacing for V_{er} = 0.3 km.Myr^{-1} and D) variable V_{er} for constant D-spacing of 12 km. E–H) Model *P–T–t* paths for rocks initially buried at 25–45 km at a time of 15 Ma for variable radiogenic D-spacing, V_{er} and Thr.

Figure 11. Syn-thrust heating model ran between 50 and 40 Ma. A) Model geotherm evolution for a scenario of synthrust heating analogous to a hot iron, between 50 and 40 Ma for Thr = 30 km, D-spacing of 12 km with no erosion, followed by conductive relaxation after 40 Ma until 15 Ma with an erosion rate of 0.5 km.Myr^{-1}, inset showing subsequent thermal evolution following the end of thrusting after 40 Ma and each line represents the geotherm at a 5 Myr interval. B)

DOI:10.1130/B36332.1

geotherm evolution in *P–T* space with overlaid *P–T* constraints. C) *P–T–t* evolution for synthrust heating (50–40 Ma) followed by thermal relaxation (40 Ma–present), D) Temperature-time thermal evolution plot showing rapid heating and diachronous metamorphism and potentially explaining 40 Ma Koronos Unit zircon rim dates. E–F) Geotherm evolution for D-spacing of 8-km for *Thr* = 30 km, G) Thermal length scale of heating (L_{per}) (depth of heat penetration) vs thrusting rate relationship showing predicted range for footwall Koronos Unit rocks, H–K) Model *P–T–t* paths for scenarios where the temperature at the base of the overthrusted CBU nappe (T_{base}) is varied from 500 to 570 °C, and D-spacing value varied from 8 to 12 km.

Figure 12. Extension model 1-D set up at 25 Ma linking tectonic stage to the thermal model. A) Pre-extensional configuration at 25 Ma following overthrusting of the CBU/Zas Unit with the base of the lithosphere at 125 km depth. B) Uniform extension of the lithosphere (β = 2, γ = 2) configuration at 15 Ma following 10 Myr of extension showing Moho and base of lithosphere depth reduced by a factor of 2. Note the same configuration will occur irrespective of the duration of extension. C–F) Model geotherm evolution following firstly overthrusting from 50 to 25 Ma with *Thr* = 30 km and V_{er} = 0.3 km.Myr^{-1} (C and D) followed by pure shear extension (β = 2, γ = 2) between 25 and 15 Ma (E and F). G–H) Model *P–T–t* evolution outputs for samples initially buried at 25–45 km depth at 15 Ma for D-spacing of 8 km (G) and 12 km (H), note the kink in *P–T–t* path to cooler temperatures coinciding with the onset of extension (H). I–J) Model geotherm evolution for depth-dependent extension (extreme scenario) of β = 1.05, γ = 5. K–L) Model *P–T–t* paths for extreme depth dependent extension for a D-spacing of 8 km (M) and 12 km (N). Note there is only ~100–150 °C isobaric heating excursion at high pressures (>6–8 kbar) even in this extreme scenario.

Figure 13. A Parameter space model outputs for 1-D depth-dependent extension, showing the temperature obtained at 15 Ma for a sample with an initial burial depth of 45 km following extension commencing at 25 Ma. B) Plot showing maximum temperature at 15 Ma for a sample initially buried to 45 km after 10 Myrs of extension with variable extension factors β and γ . C–D) Temperature time plots for a sample initially buried at 45 km depth and extension commencing at 25 Ma for variable extension factors β and γ. C) D = 8 km, D) D = 12 km. E) Temperature-time plot for D = 12 km and extension starting at 15 Ma with β = 2 and $\gamma = 2$ well reproducing themochronological data. F–M) Modeled *P–T–t* results for variable scenarios of depth-dependant extension factors β and γ for a D-spacing 12 km *Thr* = 30 km and V_{er} = 0.3 km.Myr^{-1}.

Figure 14. A) Summary tectonic cartoon showing the tectono-metamorphic evolution of Naxos MCC due to crustal thickening followed by extension. Stage 1) Ophiolite obduction and *HP–LT* M_1 metamorphism of the Cycladic Blueschists (Zas Unit). Stage 2) Crustal thickening and underthrusting of the continental shelf carbonates (Koronos Unit). Stage 3) Continued crustal thickening causing M_2 kyanite grade metamorphism in the Koronos and Core Units and eventual water saturated partial melting. Stage 4) Syn-orogenic extrusion of the Core Unit under the KSZ and later ZSZ causing decompression, muscovite dehydration melting and M_3 Sillimanite-grade metamorphism. Stage 5) Transition from compression to extension, formation of the migmatite dome at mid crustal levels. Stage 6) Onset of extension, cooling, initiation of NPDS and I-type granite intrusion. Right) Thermal model outputs for our preferred scenario involving: B) syn-thrust heating of the CBU/Zas Unit from 50 to 40 Ma modeled as a 30 km thick thrust sheet with a basal temperature of 500 °C and a D-spacing of 10 km with initially no erosion. C) Conductive relaxation of isotherms following overthrusting from 40 to 15 Ma with an erosion rate of 0.5

DOI:10.1130/B36332.1

km.Myr^{-1} and a D-spacing of 10 km. D) Onset of extension at 15 Ma until 5 Ma with erosion rate of 0.3 km.Myr^{-1}, D-spacing of 10 km and extension factors $\beta = 2$ and $\gamma = 2$.

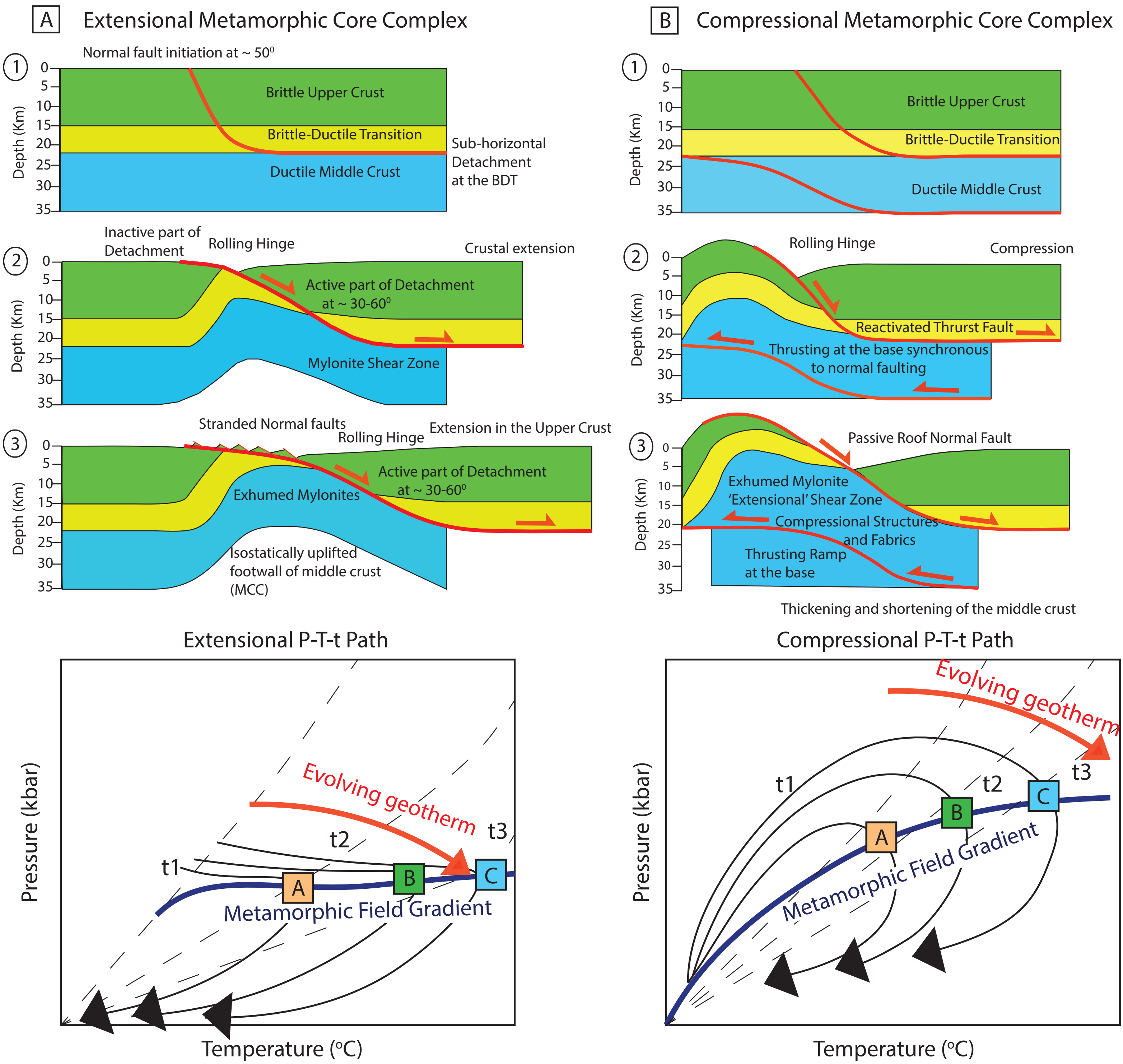

A
Extensional Metamorphic Core Complex
Normal fault initiation at ~ 50⁰
Brittle Upper Crust
Brittle-Ductile Transition
Ductile Middle Crust
Sub-horizontal Detachment at the BDT
Depth (Km)
Inactive part of Detachment
Rolling Hinge
Crustal extension
Active part of Detachment at ~ 30-60⁰
Mylonite Shear Zone
Stranded Normal faults
Rolling Hinge
Extension in the Upper Crust
Active part of Detachment at ~ 30-60⁰
Exhumed Mylonites
Isostatically uplifted footwall of middle crust (MCC)
B
Compressional Metamorphic Core Complex
Brittle Upper Crust
Brittle-Ductile Transition
Ductile Middle Crust
Rolling Hinge
Compression
Reactivated Thrurst Fault
Thrusting at the base synchronous to normal faulting
Passive Roof Normal Fault
Exhumed Mylonite
'Extensional' Shear Zone
Compressional Structures and Fabrics
Thrusting Ramp at the base
Thickening and shortening of the middle crust
Extensional P-T-t Path
Evolving geotherm
t1
t2
t3
A
B
C
Metamorphic Field Gradient
Pressure (kbar)
Temperature (°C)
Compressional P-T-t Path
Evolving geotherm
t1
t2
t3
A
B
C
Metamorphic Field Gradient
Pressure (kbar)
Temperature (°C)

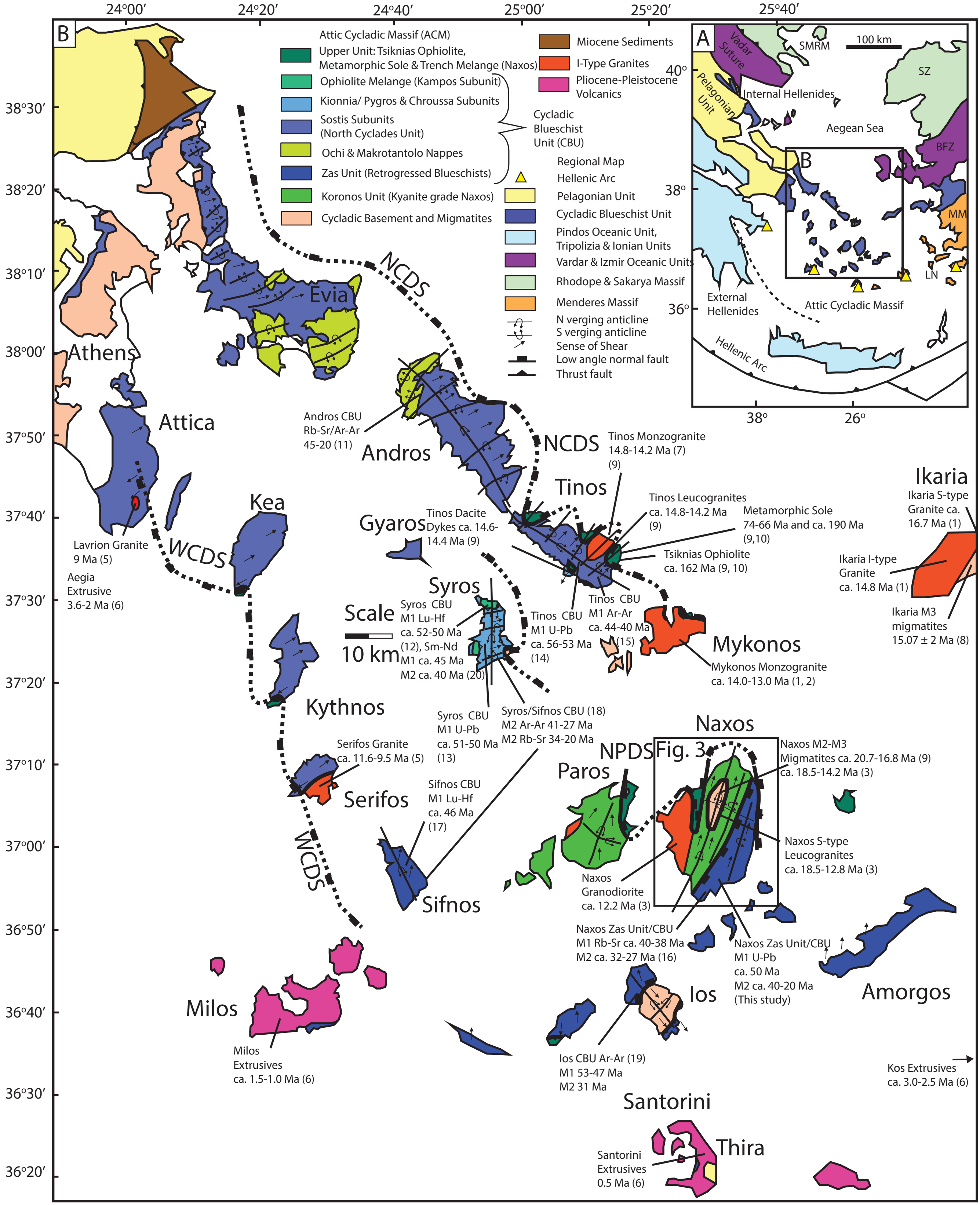

24°00′
24°20′
24°40′
25°00′
25°20′
25°40′
38°30′
38°20′
38°10′
38°00′
37°50′
37°40′
37°30′
37°20′
37°10′
37°00′
36°50′
36°40′
36°30′
36°20′
B
Attic Cycladic Massif (ACM)
Upper Unit: Tsiknias Ophiolite, Metamorphic Sole & Trench Melange (Naxos)
Ophiolite Melange (Kampos Subunit)
Kionnia/ Pygros & Chroussa Subunits
Sostis Subunits (North Cyclades Unit)
Ochi & Makrotantolo Nappes
Zas Unit (Retrogressed Blueschists)
Koronos Unit (Kyanite grade Naxos)
Cycladic Basement and Migmatites
Cycladic Blueschist Unit (CBU)
Miocene Sediments
I-Type Granites
Pliocene-Pleistocene Volcanics
Regional Map
Hellenic Arc
Pelagonian Unit
Cycladic Blueschist Unit
Pindos Oceanic Unit, Tripolizia & Ionian Units
Vardar & Izmir Oceanic Units
Rhodope & Sakarya Massif
Menderes Massif
N verging anticline
S verging anticline
Sense of Shear
Low angle normal fault
Thrust fault
A
Vadar Suture
SMRM
100 km
40°
SZ
Pelagonian Unit
Internal Hellenides
Aegean Sea
BFZ
B
38°
MM
LN
External Hellenides
36°
Attic Cycladic Massif
Hellenic Arc
38°
26°
Evia
NCDS
Athens
Attica
Andros CBU Rb-Sr/Ar-Ar 45-20 (11)
Andros
NCDS
Tinos Monzogranite 14.8-14.2 Ma (7) (9)
Tinos
Kea
Lavrion Granite 9 Ma (5)
WCDS
Aegia Extrusive 3.6-2 Ma (6)
Gyaros
Tinos Dacite Dykes ca. 14.6-14.4 Ma (9)
Tinos Leucogranites ca. 14.8-14.2 Ma (9)
Metamorphic Sole 74-66 Ma and ca. 190 Ma (9,10)
Tsiknias Ophiolite ca. 162 Ma (9, 10)
Ikaria
Ikaria S-type Granite ca. 16.7 Ma (1)
Ikaria I-type Granite ca. 14.8 Ma (1)
Ikaria M3 migmatites 15.07 ± 2 Ma (8)
Syros
Scale
10 km
Syros CBU M1 Lu-Hf ca. 52-50 Ma (12), Sm-Nd M1 ca. 45 Ma M2 ca. 40 Ma (20)
Tinos CBU M1 U-Pb ca. 56-53 Ma (14)
Tinos CBU M1 Ar-Ar ca. 44-40 Ma (15)
Mykonos
Mykonos Monzogranite ca. 14.0-13.0 Ma (1, 2)
Kythnos
Syros CBU M1 U-Pb ca. 51-50 Ma (13)
Syros/Sifnos CBU (18) M2 Ar-Ar 41-27 Ma M2 Rb-Sr 34-20 Ma
Naxos
NPDS
Fig. 3
Naxos M2-M3 Migmatites ca. 20.7-16.8 Ma (9) ca. 18.5-14.2 Ma (3)
Serifos Granite ca. 11.6-9.5 Ma (5)
Paros
Serifos
Sifnos CBU M1 Lu-Hf ca. 46 Ma (17)
WCDS
Naxos S-type Leucogranites ca. 18.5-12.8 Ma (3)
Naxos Granodiorite ca. 12.2 Ma (3)
Sifnos
Naxos Zas Unit/CBU M1 Rb-Sr ca. 40-38 Ma M2 ca. 32-27 Ma (16)
Naxos Zas Unit/CBU M1 U-Pb ca. 50 Ma M2 ca. 40-20 Ma (This study)
Amorgos
Milos
Ios
Milos Extrusives ca. 1.5-1.0 Ma (6)
Ios CBU Ar-Ar (19) M1 53-47 Ma M2 31 Ma
Kos Extrusives ca. 3.0-2.5 Ma (6)
Santorini
Thira
Santorini Extrusives 0.5 Ma (6)

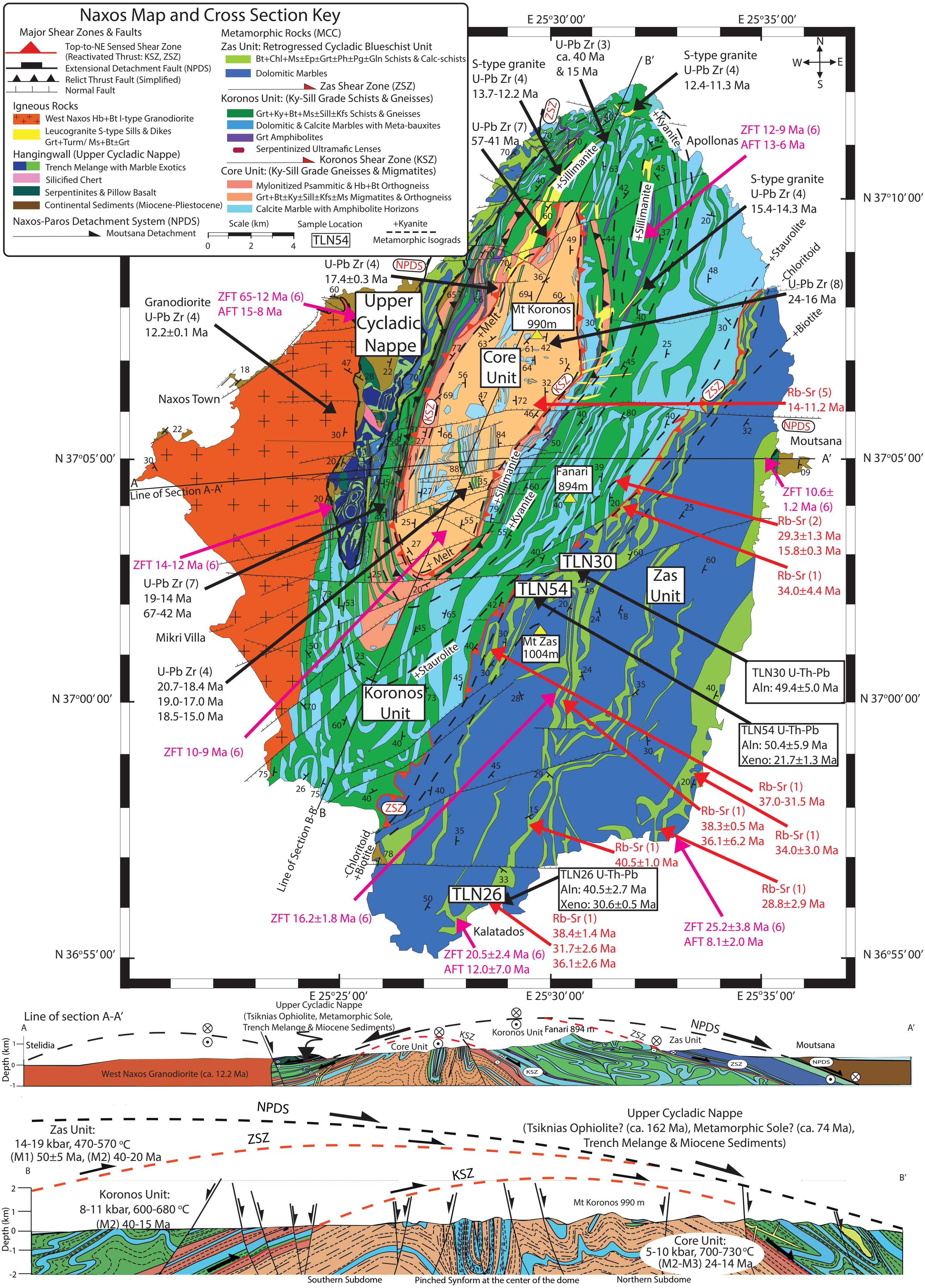
Naxos Map and Cross Section Key
Major Shear Zones & Faults
Top-to-NE Sensed Shear Zone (Reactivated Thrust: KSZ, ZSZ)
Extensional Detachment Fault (NPDS)
Relict Thrust Fault (Simplified)
Normal Fault
Igneous Rocks
West Naxos Hb+Bt I-type Granodiorite
Leucogranite S-type Sills & Dikes Grt+Turm/ Ms+Bt±Grt
Hangingwall (Upper Cycladic Nappe)
Trench Melange with Marble Exotics
Silicified Chert
Serpentinites & Pillow Basalt
Continental Sediments (Miocene-Pliestocene)
Naxos-Paros Detachment System (NPDS)
Moutsana Detachment
Metamorphic Rocks (MCC)
Zas Unit: Retrogressed Cycladic Blueschist Unit
Bt+Chl+Ms+Ep±Grt±Ph±Pg±Gln Schists & Calc-schists
Dolomitic Marbles
Zas Shear Zone (ZSZ)
Koronos Unit: (Ky-Sill Grade Schists & Gneisses)
Grt+Ky+Bt+Ms±Sill±Kfs Schists & Gneisses
Dolomitic & Calcite Marbles with Meta-bauxites
Grt Amphibolites
Serpentinized Ultramafic Lenses
Koronos Shear Zone (KSZ)
Core Unit: (Ky-Sill Grade Gneisses & Migmatites)
Mylonitized Psammitic & Hb+Bt Orthogneiss
Grt+Bt±Ky±Sill±Kfs±Ms Migmatites & Orthogneiss
Calcite Marble with Amphibolite Horizons
Scale (km)
0 2 4
Sample Location
TLN54
+Kyanite
Metamorphic Isograds
E 25°30′00′
E 25°35′00′
N 37°10′00′
N 37°05′00′
N 37°00′00′
N 36°55′00′
E 25°25′00′
S-type granite U-Pb Zr (4) 13.7-12.2 Ma
U-Pb Zr (3) ca. 40 Ma & 15 Ma
S-type granite U-Pb Zr (4) 12.4-11.3 Ma
U-Pb Zr (7) 57-41 Ma
Apollonas
ZFT 12-9 Ma (6)
AFT 13-6 Ma
S-type granite U-Pb Zr (4) 15.4-14.3 Ma
U-Pb Zr (4) 17.4±0.3 Ma
NPDS
Granodiorite U-Pb Zr (4) 12.2±0.1 Ma
ZFT 65-12 Ma (6)
AFT 15-8 Ma
Upper Cycladic Nappe
Mt Koronos 990m
Core Unit
U-Pb Zr (8) 24-16 Ma
Naxos Town
Rb-Sr (5) 14-11.2 Ma
Moutsana
Line of Section A-A′
Fanari 894m
ZFT 10.6± 1.2 Ma (6)
Rb-Sr (2) 29.3±1.3 Ma 15.8±0.3 Ma
ZFT 14-12 Ma (6)
Rb-Sr (1) 34.0±4.4 Ma
U-Pb Zr (7) 19-14 Ma 67-42 Ma
TLN30
TLN54
Zas Unit
Mikri Villa
Mt Zas 1004m
U-Pb Zr (4) 20.7-18.4 Ma 19.0-17.0 Ma 18.5-15.0 Ma
TLN30 U-Th-Pb Aln: 49.4±5.0 Ma
Koronos Unit
TLN54 U-Th-Pb Aln: 50.4±5.9 Ma Xeno: 21.7±1.3 Ma
ZFT 10-9 Ma (6)
Rb-Sr (1) 37.0-31.5 Ma
Rb-Sr (1) 38.3±0.5 Ma 36.1±6.2 Ma
Rb-Sr (1) 34.0±3.0 Ma
Rb-Sr (1) 40.5±1.0 Ma
Line of Section B-B′
ZSZ
KSZ
+Sillimanite
+Staurolite
+Chloritoid
+Biotite
-Chloritoid +Biotite
+Melt
TLN26 U-Th-Pb Aln: 40.5±2.7 Ma Xeno: 30.6±0.5 Ma
TLN26
Rb-Sr (1) 28.8±2.9 Ma
ZFT 16.2±1.8 Ma (6)
Rb-Sr (1) 38.4±1.4 Ma 31.7±2.6 Ma 36.1±2.6 Ma
Kalatados
ZFT 25.2±3.8 Ma (6)
AFT 8.1±2.0 Ma
ZFT 20.5±2.4 Ma (6)
AFT 12.0±7.0 Ma
Line of section A-A′
Stelidia
Upper Cycladic Nappe (Tsiknias Ophiolite, Metamorphic Sole, Trench Melange & Miocene Sediments)
Koronos Unit
Fanari 894 m
Zas Unit
Core Unit
Moutsana
West Naxos Granodiorite (ca. 12.2 Ma)
Depth (km)
NPDS
Zas Unit: 14-19 kbar, 470-570 °C (M1) 50±5 Ma, (M2) 40-20 Ma
Upper Cycladic Nappe (Tsiknias Ophiolite? (ca. 162 Ma), Metamorphic Sole? (ca. 74 Ma), Trench Melange & Miocene Sediments)
Koronos Unit: 8-11 kbar, 600-680 °C (M2) 40-15 Ma
Mt Koronos 990 m
Core Unit: 5-10 kbar, 700-730 °C (M2-M3) 24-14 Ma
Southern Subdome
Pinched Synform at the center of the dome
Northern Subdome

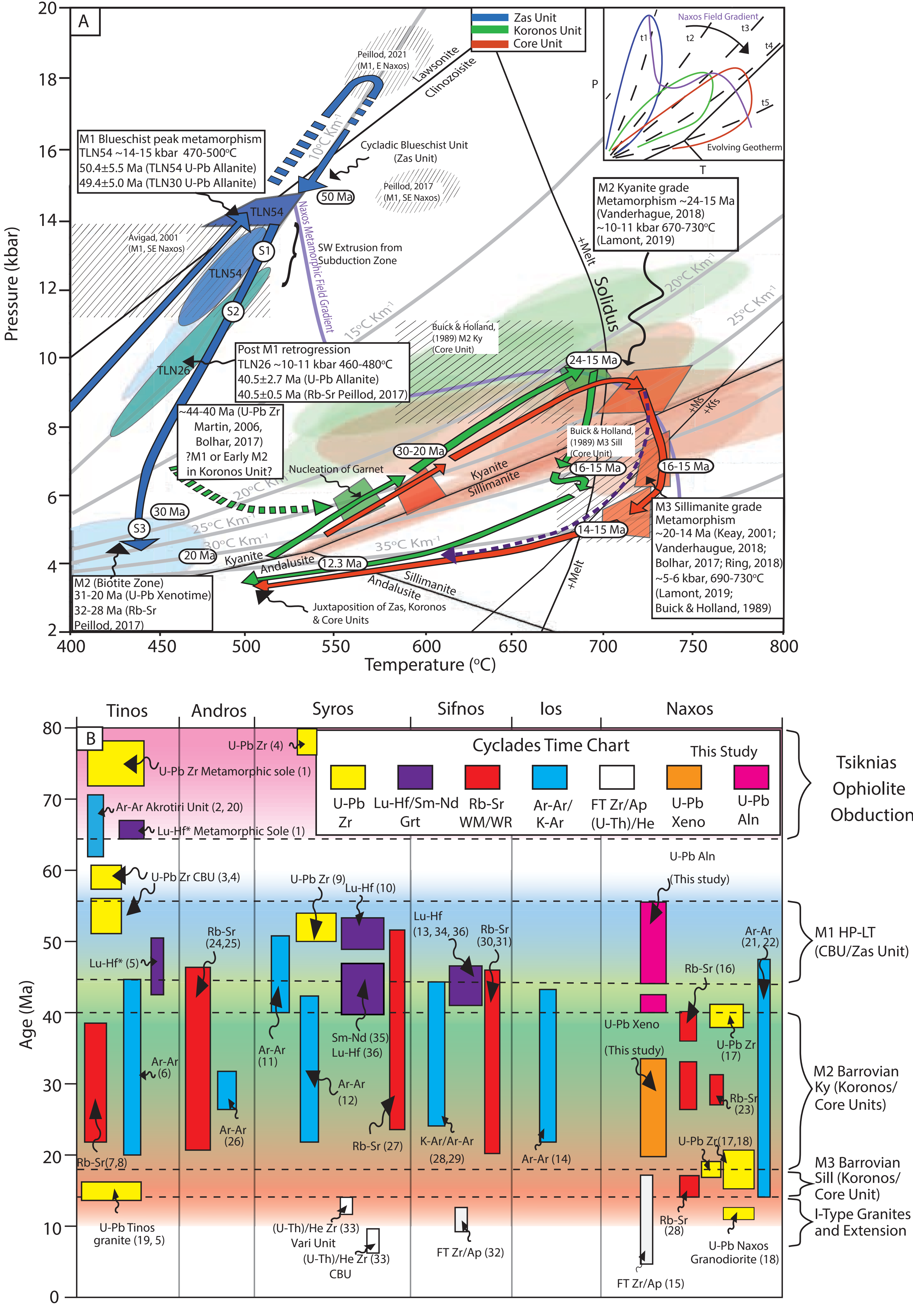

A
Zas Unit
Koronos Unit
Core Unit
Naxos Field Gradient
t1
t2
t3
t4
t5
P
T
Evolving Geotherm
Peillod, 2021
(M1, E Naxos)
Lawsonite
Clinozoisite
M1 Blueschist peak metamorphism
TLN54 ~14-15 kbar 470-500°C
50.4±5.5 Ma (TLN54 U-Pb Allanite)
49.4±5.0 Ma (TLN30 U-Pb Allanite)
10°C Km-1
Cycladic Blueschist Unit
(Zas Unit)
50 Ma
Peillod, 2017
(M1, SE Naxos)
M2 Kyanite grade
Metamorphism ~24-15 Ma
(Vanderhague, 2018)
~10-11 kbar 670-730°C
(Lamont, 2019)
TLN54
Avigad, 2001
(M1, SE Naxos)
S1
SW Extrusion from
Subduction Zone
Naxos Metamorphic Field Gradient
+Melt
Solidus
20°C Km-1
25°C Km-1
TLN54
S2
15°C Km-1
Buick & Holland,
(1989) M2 Ky
(Core Unit)
Post M1 retrogression
TLN26 ~10-11 kbar 460-480°C
40.5±2.7 Ma (U-Pb Allanite)
40.5±0.5 Ma (Rb-Sr Peillod, 2017)
TLN26
24-15 Ma
~44-40 Ma (U-Pb Zr
Martin, 2006,
Bolhar, 2017)
?M1 or Early M2
in Koronos Unit?
+Ms
+Kfs
Buick & Holland,
(1989) M3 Sill
(Core Unit)
30-20 Ma
Nucleation of Garnet
Kyanite
Sillimanite
16-15 Ma
16-15 Ma
20°C Km-1
M3 Sillimanite grade
Metamorphism
~20-14 Ma (Keay, 2001;
Vanderhaugue, 2018;
Bolhar, 2017; Ring, 2018)
~5-6 kbar, 690-730°C
(Lamont, 2019;
Buick & Holland, 1989)
30 Ma
S3
25°C Km-1
30°C Km-1
35°C Km-1
14-15 Ma
20 Ma
Kyanite
Andalusite
12.3 Ma
+Melt
Sillimanite
Andalusite
M2 (Biotite Zone)
31-20 Ma (U-Pb Xenotime)
32-28 Ma (Rb-Sr
Peillod, 2017)
Juxtaposition of Zas, Koronos
& Core Units
Pressure (kbar)
Temperature (°C)
2
4
6
8
10
12
14
16
18
20
400
450
500
550
600
650
700
750
800
B
Tinos
Andros
Syros
Sifnos
Ios
Naxos
Cyclades Time Chart
This Study
U-Pb Zr
Lu-Hf/Sm-Nd Grt
Rb-Sr WM/WR
Ar-Ar/ K-Ar
FT Zr/Ap (U-Th)/He
U-Pb Xeno
U-Pb Aln
Tsiknias Ophiolite Obduction
M1 HP-LT (CBU/Zas Unit)
M2 Barrovian Ky (Koronos/ Core Units)
M3 Barrovian Sill (Koronos/ Core Unit)
I-Type Granites and Extension
U-Pb Zr (4)
U-Pb Zr Metamorphic sole (1)
Ar-Ar Akrotiri Unit (2, 20)
Lu-Hf* Metamorphic Sole (1)
U-Pb Zr CBU (3,4)
U-Pb Zr (9)
Lu-Hf (10)
U-Pb Aln
(This study)
Lu-Hf
(13, 34, 36)
Rb-Sr
(30,31)
Ar-Ar
(21, 22)
Rb-Sr
(24,25)
Lu-Hf* (5)
Rb-Sr (16)
Sm-Nd (35)
Lu-Hf (36)
U-Pb Xeno
(This study)
U-Pb Zr
(17)
Ar-Ar
(6)
Ar-Ar
(11)
Ar-Ar
(12)
Rb-Sr
(23)
Ar-Ar
(26)
Rb-Sr (27)
K-Ar/Ar-Ar
(28,29)
Ar-Ar (14)
U-Pb Zr(17,18)
Rb-Sr(7,8)
U-Pb Tinos
granite (19, 5)
(U-Th)/He Zr (33)
Vari Unit
(U-Th)/He Zr (33)
CBU
FT Zr/Ap (32)
Rb-Sr
(28)
U-Pb Naxos
Granodiorite (18)
FT Zr/Ap (15)
Age (Ma)
0
10
20
30
40
50
60
70
80

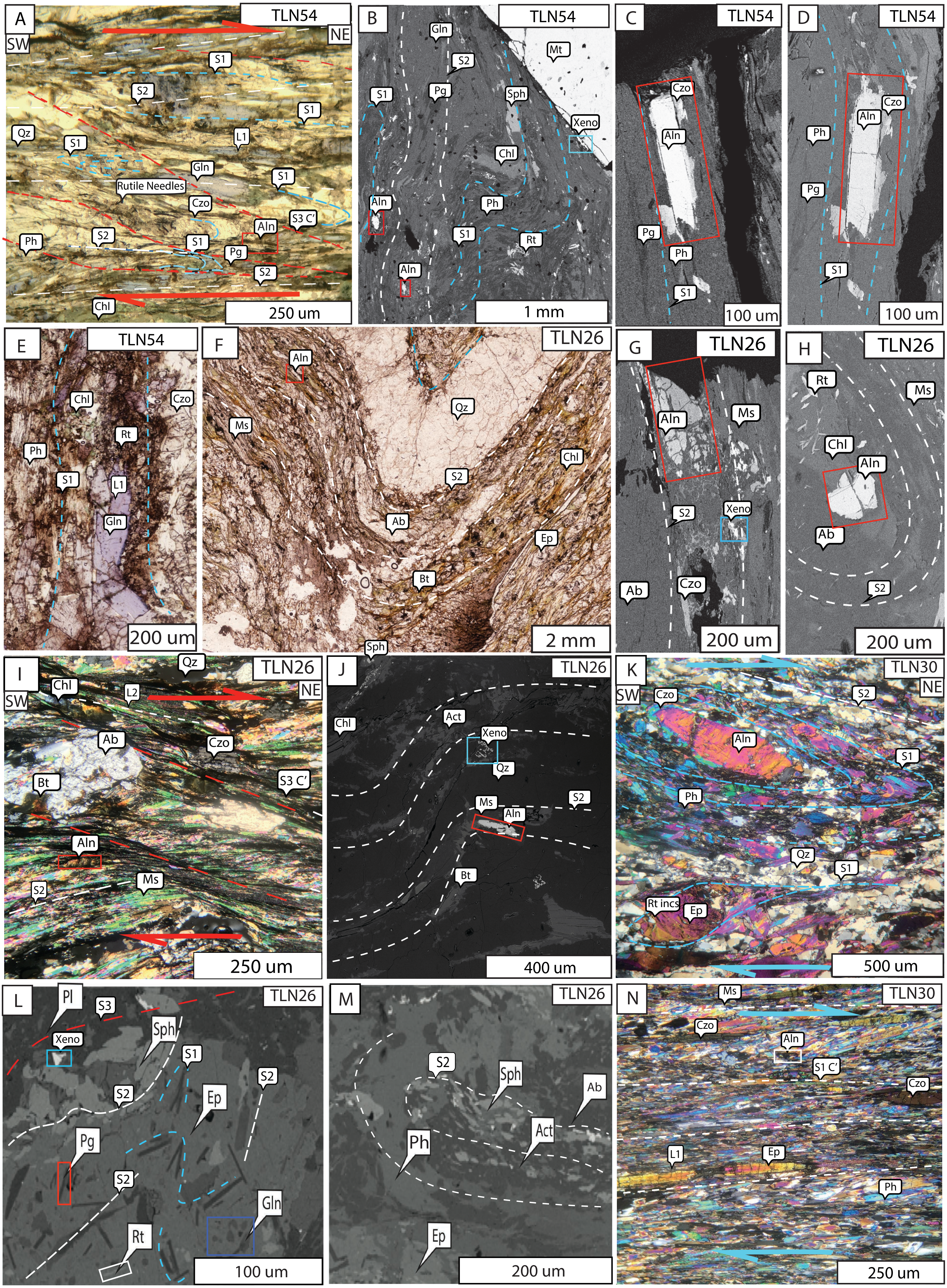

A
TLN54
SW
NE
S1
S2
Qz
L1
Gln
Rutile Needles
Czo
Aln
S3 C'
Ph
Pg
Chl
250 um
B
Mt
Sph
Xeno
Chl
Rt
1 mm
C
D
100 um
E
Czo
Rt
L1
200 um
F
TLN26
Ms
Ab
Bt
Ep
2 mm
G
H
I
L2
J
Act
400 um
K
TLN30
Rt incs
500 um
L
Pl
S3
100 um
M
200 um
N
S1 C'

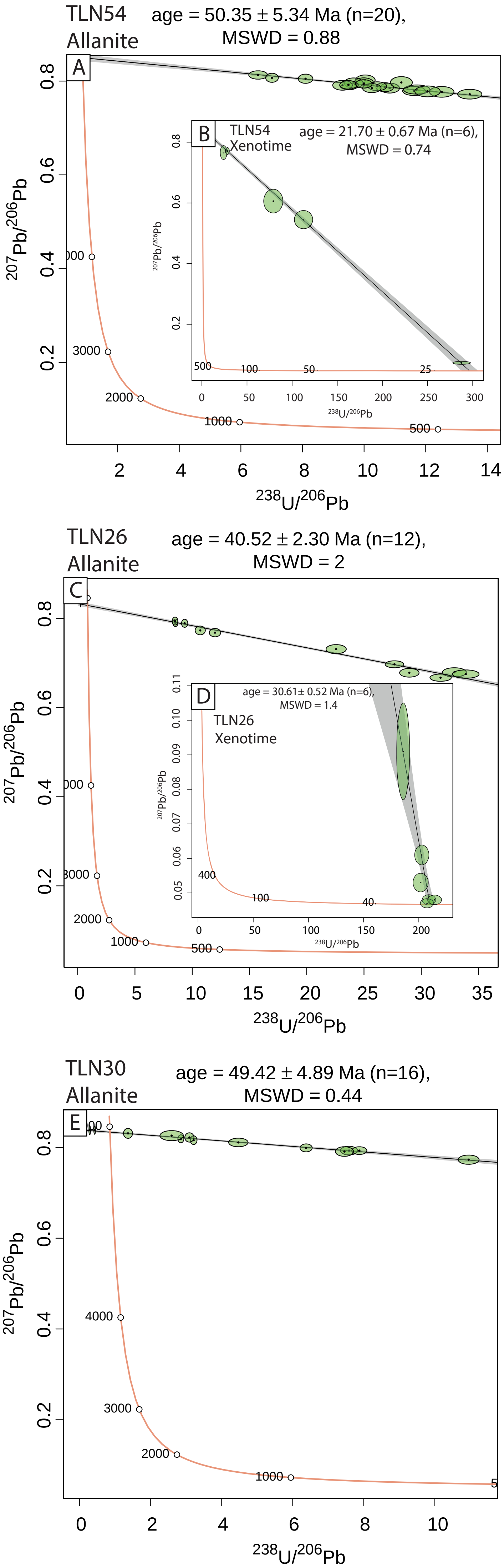

TLN54
Allanite
age = 50.35 ± 5.34 Ma (n=20),
MSWD = 0.88
A
B
TLN54
Xenotime
age = 21.70 ± 0.67 Ma (n=6),
MSWD = 0.74
3000
2000
1000
500
$^{207}Pb/^{206}Pb$
$^{238}U/^{206}Pb$
TLN26
Allanite
age = 40.52 ± 2.30 Ma (n=12),
MSWD = 2
C
D
age = 30.61± 0.52 Ma (n=6),
MSWD = 1.4
TLN26
Xenotime
400
100
40
TLN30
Allanite
age = 49.42 ± 4.89 Ma (n=16),
MSWD = 0.44
E
4000

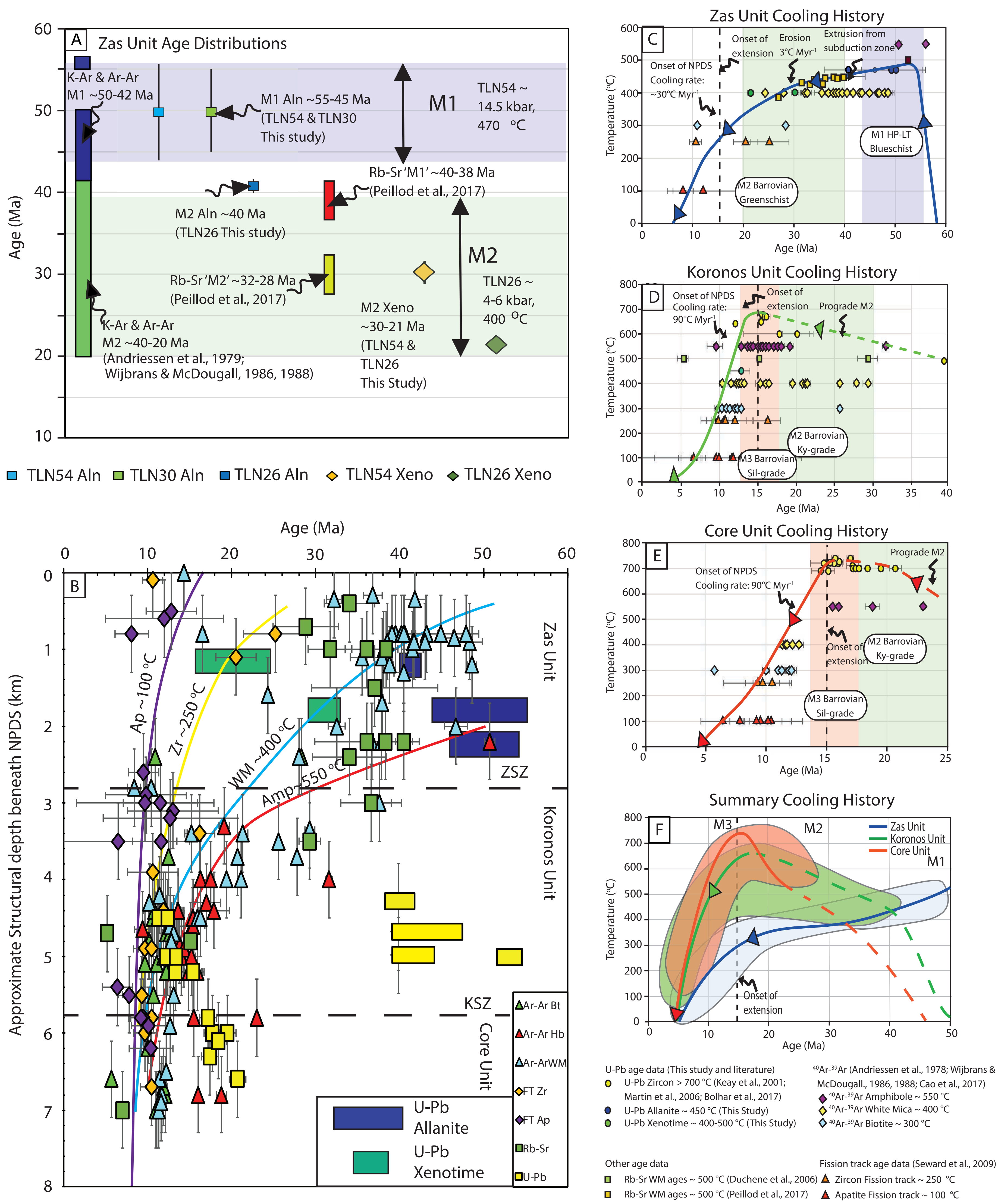

Zas Unit Age Distributions
K-Ar & Ar-Ar M1 ~50-42 Ma
M1 Aln ~55-45 Ma (TLN54 & TLN30 This study)
M1
TLN54 ~ 14.5 kbar, 470 °C
Rb-Sr 'M1' ~40-38 Ma (Peillod et al., 2017)
M2 Aln ~40 Ma (TLN26 This study)
Rb-Sr 'M2' ~32-28 Ma (Peillod et al., 2017)
M2
TLN26 ~ 4-6 kbar, 400 °C
M2 Xeno ~30-21 Ma (TLN54 & TLN26 This Study)
K-Ar & Ar-Ar M2 ~40-20 Ma (Andriessen et al., 1979; Wijbrans & McDougall, 1986, 1988)
Age (Ma)
TLN54 Aln
TLN30 Aln
TLN26 Aln
TLN54 Xeno
TLN26 Xeno
Approximate Structural depth beneath NPDS (km)
Ap ~100 °C
Zr ~250 °C
WM ~400 °C
Amp ~550 °C
Zas Unit
ZSZ
Koronos Unit
KSZ
Core Unit
Ar-Ar Bt
Ar-Ar Hb
Ar-ArWM
FT Zr
FT Ap
Rb-Sr
U-Pb
U-Pb Allanite
U-Pb Xenotime
Zas Unit Cooling History
Temperature (°C)
Onset of NPDS Cooling rate: ~30°C Myr-1
Onset of extension
Erosion 3°C Myr-1
Extrusion from subduction zone
M1 HP-LT Blueschist
M2 Barrovian Greenschist
Koronos Unit Cooling History
Onset of NPDS Cooling rate: 90°C Myr-1
Onset of extension
Prograde M2
M2 Barrovian Ky-grade
M3 Barrovian Sil-grade
Core Unit Cooling History
Onset of NPDS Cooling rate: 90°C Myr-1
Prograde M2
Onset of extension
M2 Barrovian Ky-grade
M3 Barrovian Sil-grade
Summary Cooling History
M3
M2
M1
Zas Unit
Koronos Unit
Core Unit
Onset of extension
U-Pb age data (This study and literature)
U-Pb Zircon > 700 °C (Keay et al., 2001; Martin et al., 2006; Bolhar et al., 2017)
U-Pb Allanite ~ 450 °C (This Study)
U-Pb Xenotime ~ 400-500 °C (This Study)
40Ar-39Ar (Andriessen et al., 1978; Wijbrans & McDougall., 1986, 1988; Cao et al., 2017)
40Ar-39Ar Amphibole ~ 550 °C
40Ar-39Ar White Mica ~ 400 °C
40Ar-39Ar Biotite ~ 300 °C
Other age data
Rb-Sr WM ages ~ 500 °C (Duchene et al., 2006)
Rb-Sr WM ages ~ 500 °C (Peillod et al., 2017)
Lu-Hf Grt (Syros) (Lagos et al., 2007)
Fission track age data (Seward et al., 2009)
Zircon Fission track ~ 250 °C
Apatite Fission track ~ 100 °C

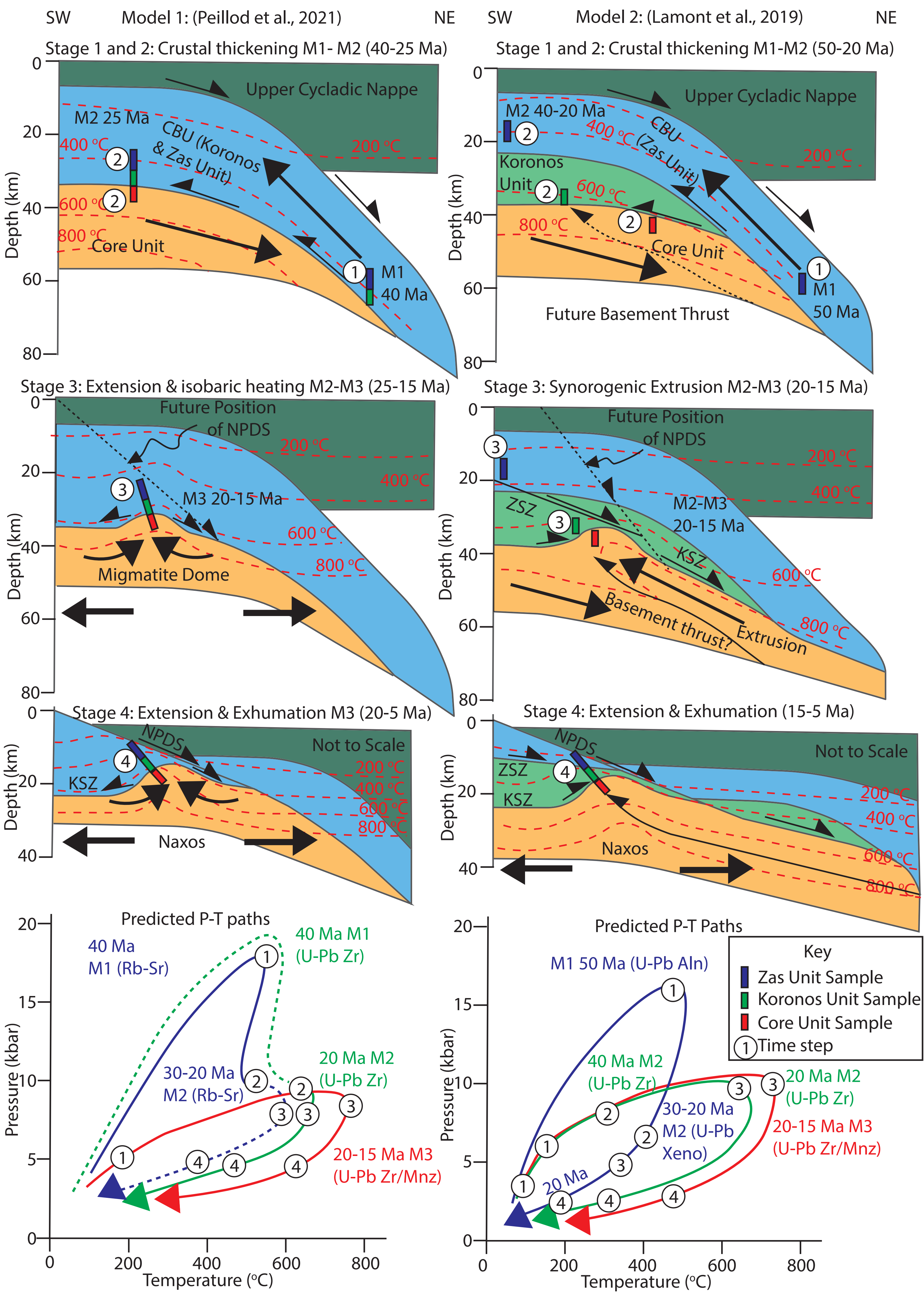

SW
Model 1: (Peillod et al., 2021)
NE
SW
Model 2: (Lamont et al., 2019)
NE
Stage 1 and 2: Crustal thickening M1- M2 (40-25 Ma)
Upper Cycladic Nappe
M2 25 Ma
CBU (Koronos & Zas Unit)
400 °C
200 °C
600 °C
800 °C
Core Unit
M1 40 Ma
Depth (km)
Stage 1 and 2: Crustal thickening M1-M2 (50-20 Ma)
M2 40-20 Ma
CBU (Zas Unit)
Koronos Unit
M1 50 Ma
Future Basement Thrust
Stage 3: Extension & isobaric heating M2-M3 (25-15 Ma)
Future Position of NPDS
M3 20-15 Ma
Migmatite Dome
Stage 3: Synorogenic Extrusion M2-M3 (20-15 Ma)
ZSZ
KSZ
M2-M3 20-15 Ma
Basement thrust?
Extrusion
Stage 4: Extension & Exhumation M3 (20-5 Ma)
NPDS
Not to Scale
Naxos
Stage 4: Extension & Exhumation (15-5 Ma)
Predicted P-T paths
40 Ma M1 (Rb-Sr)
40 Ma M1 (U-Pb Zr)
30-20 Ma M2 (Rb-Sr)
20 Ma M2 (U-Pb Zr)
20-15 Ma M3 (U-Pb Zr/Mnz)
Pressure (kbar)
Temperature (°C)
Predicted P-T Paths
M1 50 Ma (U-Pb Aln)
40 Ma M2 (U-Pb Zr)
30-20 Ma M2 (U-Pb Xeno)
20 Ma
Key
Zas Unit Sample
Koronos Unit Sample
Core Unit Sample
Time step

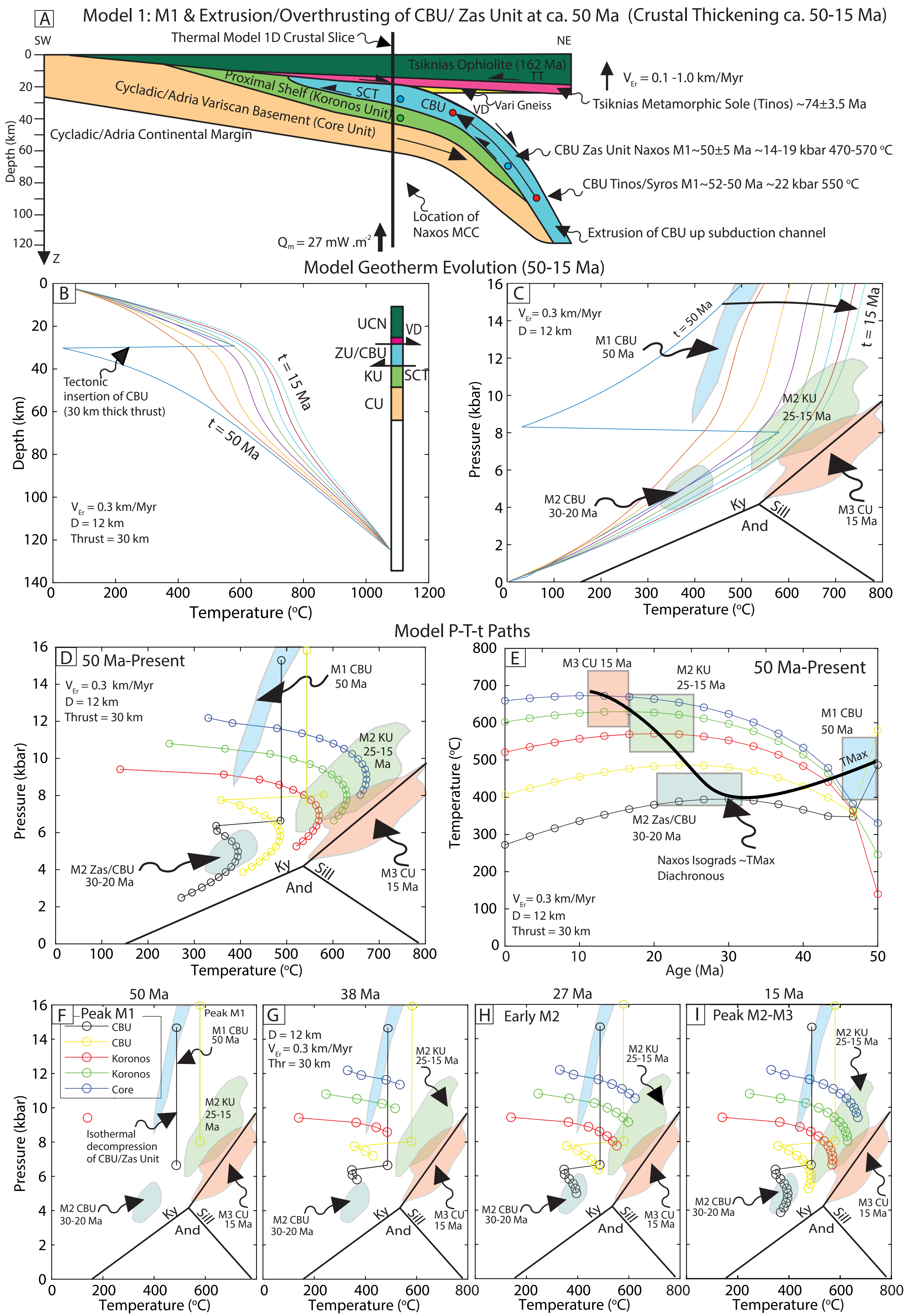

A
Model 1: M1 & Extrusion/Overthrusting of CBU/ Zas Unit at ca. 50 Ma (Crustal Thickening ca. 50-15 Ma)
SW
NE
Thermal Model 1D Crustal Slice
Tsiknias Ophiolite (162 Ma)
TT
Proximal Shelf (Koronos Unit)
SCT
CBU
VD
Vari Gneiss
Cycladic/Adria Variscan Basement (Core Unit)
Cycladic/Adria Continental Margin
V_Er = 0.1 -1.0 km/Myr
Tsiknias Metamorphic Sole (Tinos) ~74±3.5 Ma
CBU Zas Unit Naxos M1~50±5 Ma ~14-19 kbar 470-570 °C
CBU Tinos/Syros M1~52-50 Ma ~22 kbar 550 °C
Extrusion of CBU up subduction channel
Location of Naxos MCC
Q_m = 27 mW .m^-2
Depth (km)
Z
Model Geotherm Evolution (50-15 Ma)
B
UCN
VD
ZU/CBU
KU
SCT
CU
t = 15 Ma
t = 50 Ma
Tectonic insertion of CBU (30 km thick thrust)
V_Er = 0.3 km/Myr
D = 12 km
Thrust = 30 km
Depth (km)
Temperature (°C)
C
V_Er = 0.3 km/Myr
D = 12 km
M1 CBU 50 Ma
t = 50 Ma
t = 15 Ma
M2 KU 25-15 Ma
M2 CBU 30-20 Ma
M3 CU 15 Ma
Ky
Sill
And
Pressure (kbar)
Temperature (°C)
Model P-T-t Paths
D
50 Ma-Present
V_Er = 0.3 km/Myr
D = 12 km
Thrust = 30 km
M1 CBU 50 Ma
M2 KU 25-15 Ma
M2 Zas/CBU 30-20 Ma
M3 CU 15 Ma
Ky
Sill
And
Pressure (kbar)
Temperature (°C)
E
M3 CU 15 Ma
M2 KU 25-15 Ma
50 Ma-Present
M1 CBU 50 Ma
TMax
M2 Zas/CBU 30-20 Ma
Naxos Isograds ~TMax Diachronous
V_Er = 0.3 km/Myr
D = 12 km
Thrust = 30 km
Temperature (°C)
Age (Ma)
50 Ma
38 Ma
27 Ma
15 Ma
F
Peak M1
CBU
CBU
Koronos
Koronos
Core
M1 CBU 50 Ma
M2 KU 25-15 Ma
Isothermal decompression of CBU/Zas Unit
M2 CBU 30-20 Ma
M3 CU 15 Ma
G
D = 12 km
V_Er = 0.3 km/Myr
Thr = 30 km
H
Early M2
I
Peak M2-M3
Pressure (kbar)
Temperature (°C)

Model 1: Instantaneous overthrust (50-15 Ma) parameter space

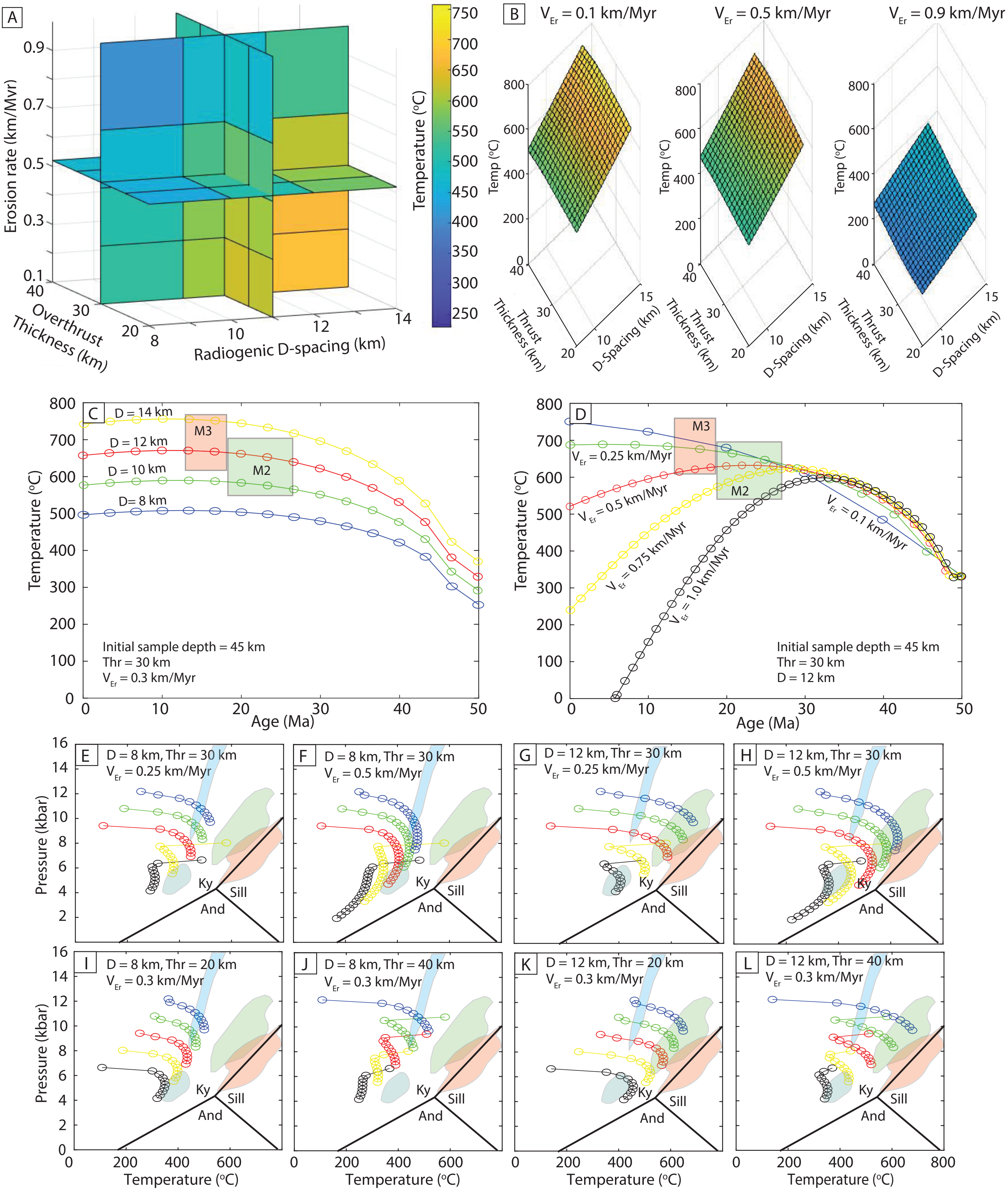

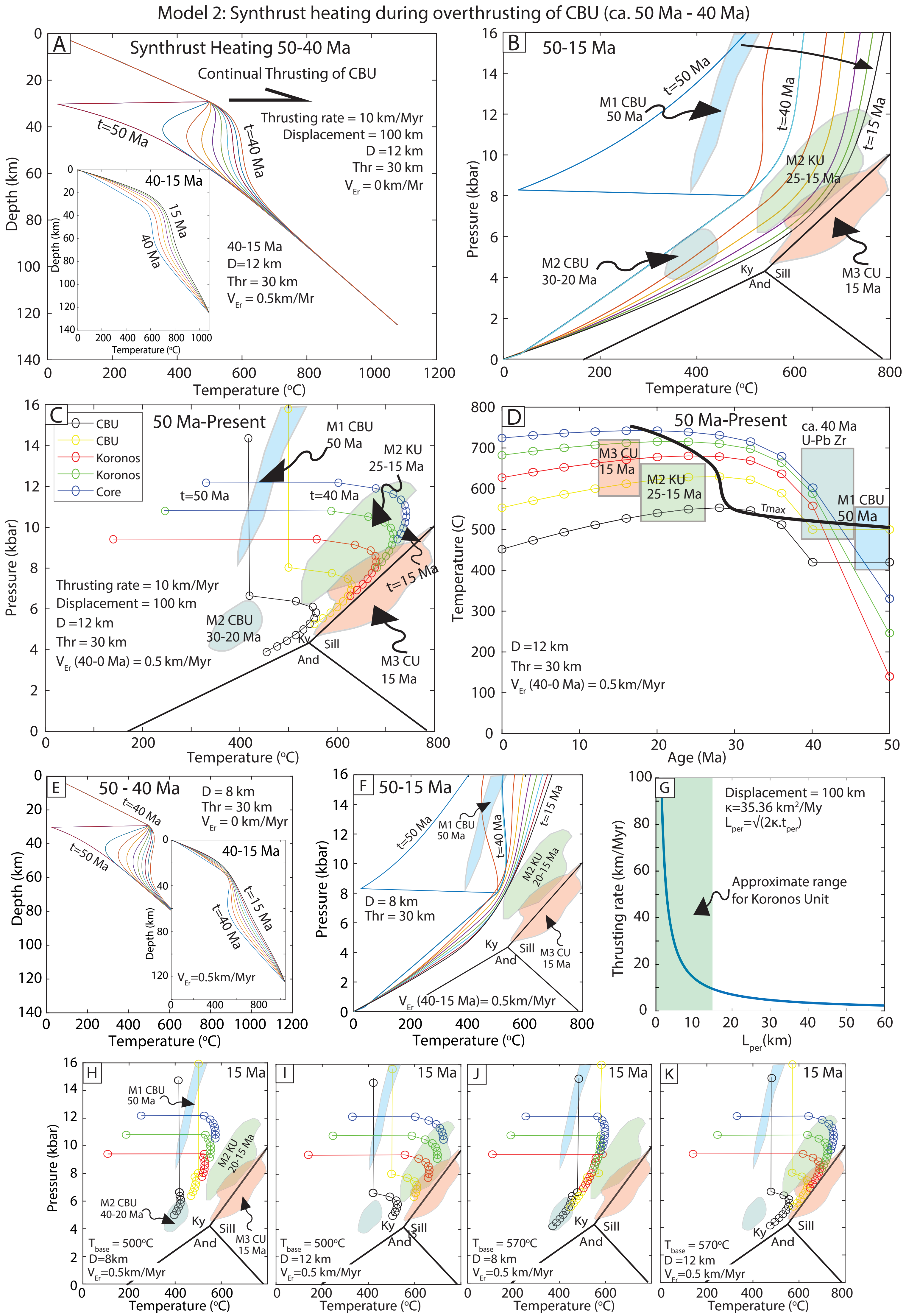

Model 2: Synthrust heating during overthrusting of CBU (ca. 50 Ma - 40 Ma)
A
Synthrust Heating 50-40 Ma
Continual Thrusting of CBU
Thrusting rate = 10 km/Myr
Displacement = 100 km
D = 12 km
Thr = 30 km
V_Er = 0 km/Mr
t=50 Ma
t=40 Ma
40-15 Ma
15 Ma
40 Ma
40-15 Ma
D=12 km
Thr = 30 km
V_Er = 0.5km/Mr
Depth (km)
Temperature (°C)
B
50-15 Ma
t=50 Ma
M1 CBU
50 Ma
t=40 Ma
t=15 Ma
M2 KU
25-15 Ma
M2 CBU
30-20 Ma
M3 CU
15 Ma
Ky
Sill
And
Pressure (kbar)
Temperature (°C)
C
50 Ma-Present
CBU
CBU
Koronos
Koronos
Core
M1 CBU
50 Ma
M2 KU
25-15 Ma
t=50 Ma
t=40 Ma
t=15 Ma
Thrusting rate = 10 km/Myr
Displacement = 100 km
D =12 km
Thr = 30 km
V_Er (40-0 Ma) = 0.5 km/Myr
M2 CBU
30-20 Ma
M3 CU
15 Ma
Ky
Sill
And
Pressure (kbar)
Temperature (°C)
D
50 Ma-Present
ca. 40 Ma
U-Pb Zr
M3 CU
15 Ma
M2 KU
25-15 Ma
M1 CBU
50 Ma
Tmax
D =12 km
Thr = 30 km
V_Er (40-0 Ma) = 0.5 km/Myr
Temperature (C)
Age (Ma)
E
50 - 40 Ma
D = 8 km
Thr = 30 km
V_Er = 0 km/Myr
t=40 Ma
t=50 Ma
40-15 Ma
t=15 Ma
t=40 Ma
V_Er=0.5km/Myr
Depth (km)
Temperature (°C)
F
50-15 Ma
t=50 Ma
M1 CBU
50 Ma
t=40 Ma
t=15 Ma
M2 KU
20-15 Ma
D = 8 km
Thr = 30 km
Ky
Sill
And
M3 CU
15 Ma
V_Er (40-15 Ma)= 0.5km/Myr
Pressure (kbar)
Temperature (°C)
G
Displacement = 100 km
κ=35.36 km²/My
L_per=√(2κ.t_per)
Approximate range
for Koronos Unit
Thrusting rate (km/Myr)
L_per (km)
H
15 Ma
M1 CBU
50 Ma
M2 KU
20-15 Ma
M2 CBU
40-20 Ma
Ky
Sill
And
M3 CU
15 Ma
T_base = 500°C
D=8km
V_Er=0.5km/Myr
I
15 Ma
Ky
Sill
And
T_base = 500°C
D =12 km
V_Er=0.5 km/Myr
J
15 Ma
Ky
Sill
And
T_base = 570°C
D =8 km
V_Er=0.5 km/Myr
K
15 Ma
Ky
Sill
And
T_base = 570°C
D =12 km
V_Er=0.5 km/Myr
Pressure (kbar)
Temperature (°C)

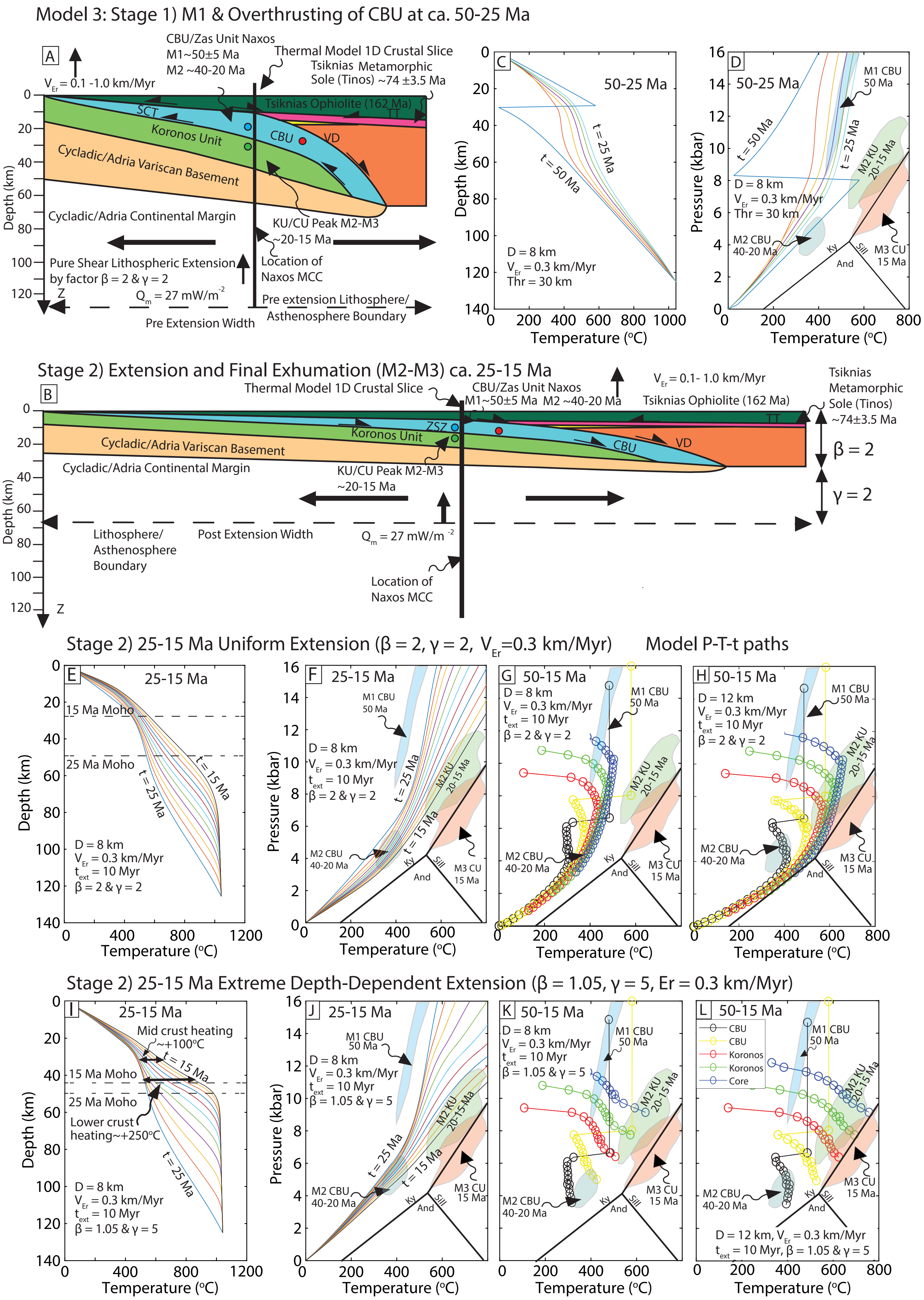

Model 3: Stage 1) M1 & Overthrusting of CBU at ca. 50-25 Ma
Stage 2) Extension and Final Exhumation (M2-M3) ca. 25-15 Ma
Stage 2) 25-15 Ma Uniform Extension (β = 2, γ = 2, V_Er=0.3 km/Myr)
Model P-T-t paths
Stage 2) 25-15 Ma Extreme Depth-Dependent Extension (β = 1.05, γ = 5, Er = 0.3 km/Myr)
Thermal Model 1D Crustal Slice
CBU/Zas Unit Naxos
M1~50±5 Ma
M2 ~40-20 Ma
Tsiknias Metamorphic Sole (Tinos) ~74 ±3.5 Ma
Tsiknias Ophiolite (162 Ma)
Koronos Unit
Cycladic/Adria Variscan Basement
Cycladic/Adria Continental Margin
KU/CU Peak M2-M3 ~20-15 Ma
Pure Shear Lithospheric Extension by factor β = 2 & γ = 2
Location of Naxos MCC
Pre Extension Width
Pre extension Lithosphere/ Asthenosphere Boundary
Post Extension Width
Lithosphere/ Asthenosphere Boundary
Depth (km)
Pressure (kbar)
Temperature (°C)
Mid crust heating ~+100°C
Lower crust heating~+250°C
15 Ma Moho
25 Ma Moho

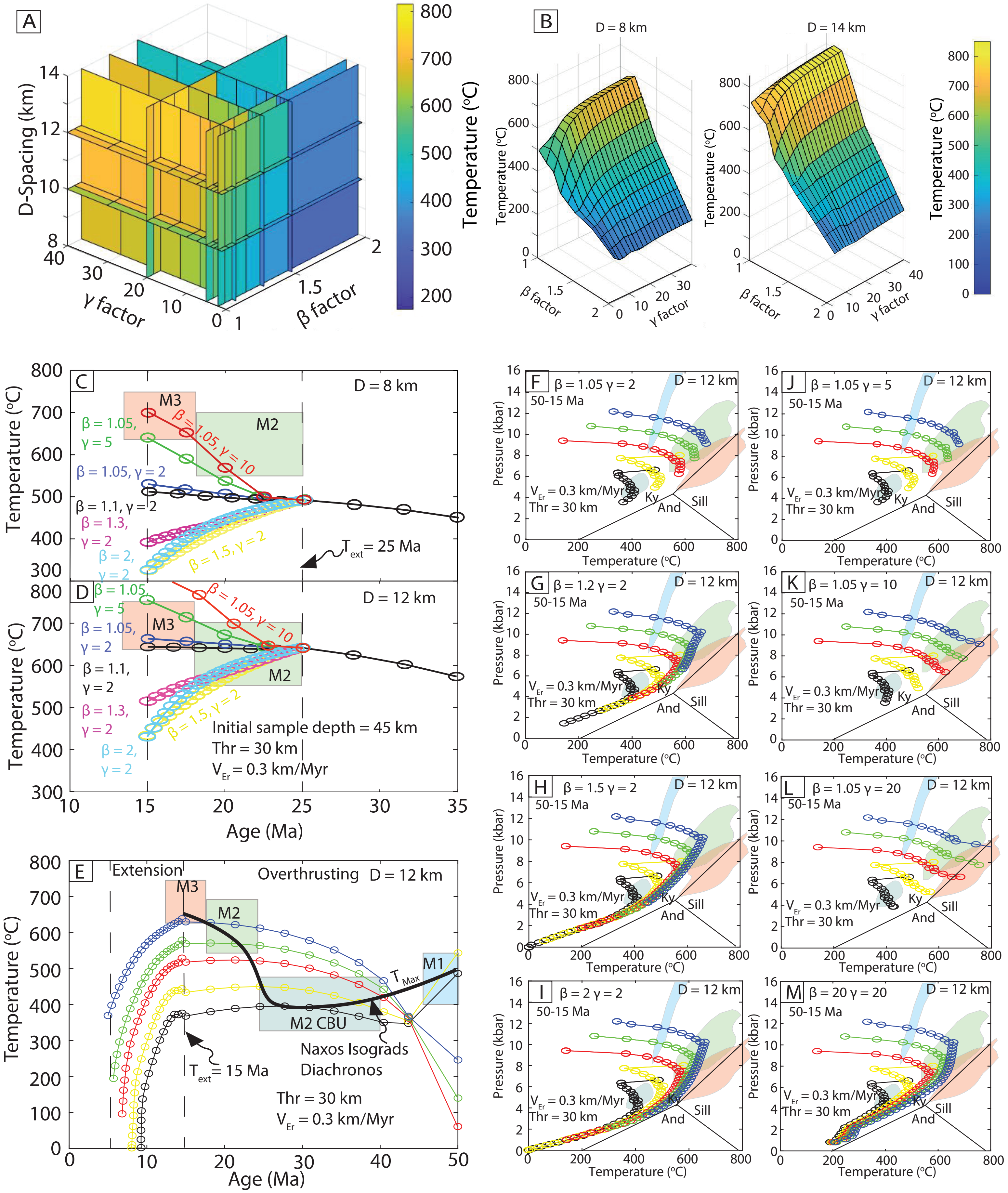

A
B
C
D
E
F
G
H
I
J
K
L
M
D = 8 km
D = 14 km
D = 12 km
M3
M2
M1
M2 CBU
Extension
Overthrusting
Naxos Isograds
Diachronos
Initial sample depth = 45 km
Thr = 30 km
V_{Er} = 0.3 km/Myr
T_{ext} = 25 Ma
T_{ext} = 15 Ma
T_{Max}
50-15 Ma
Ky
And
Sill
D-Spacing (km)
γ factor
β factor
Temperature (°C)
Age (Ma)
Pressure (kbar)

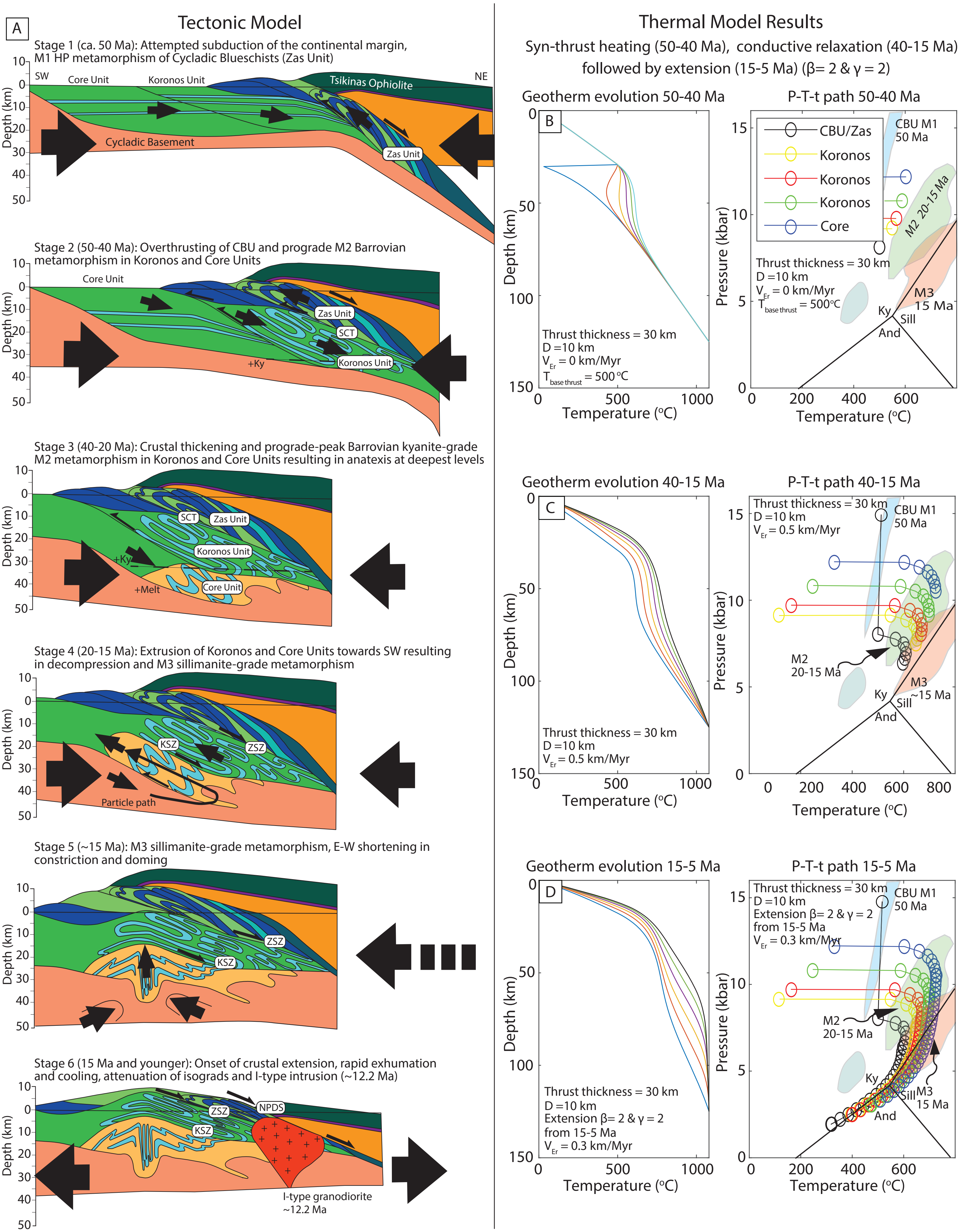

A
Tectonic Model
Stage 1 (ca. 50 Ma): Attempted subduction of the continental margin, M1 HP metamorphism of Cycladic Blueschists (Zas Unit)
SW
NE
Core Unit
Koronos Unit
Tsikinas Ophiolite
Cycladic Basement
Zas Unit
Depth (km)
Stage 2 (50-40 Ma): Overthrusting of CBU and prograde M2 Barrovian metamorphism in Koronos and Core Units
Zas Unit
SCT
Koronos Unit
+Ky
Stage 3 (40-20 Ma): Crustal thickening and prograde-peak Barrovian kyanite-grade M2 metamorphism in Koronos and Core Units resulting in anatexis at deepest levels
SCT
Zas Unit
Koronos Unit
+Ky
+Melt
Core Unit
Stage 4 (20-15 Ma): Extrusion of Koronos and Core Units towards SW resulting in decompression and M3 sillimanite-grade metamorphism
KSZ
ZSZ
Particle path
Stage 5 (~15 Ma): M3 sillimanite-grade metamorphism, E-W shortening in constriction and doming
ZSZ
KSZ
Stage 6 (15 Ma and younger): Onset of crustal extension, rapid exhumation and cooling, attenuation of isograds and I-type intrusion (~12.2 Ma)
ZSZ
NPDS
KSZ
I-type granodiorite
~12.2 Ma
Thermal Model Results
Syn-thrust heating (50-40 Ma), conductive relaxation (40-15 Ma)
followed by extension (15-5 Ma) (β= 2 & γ = 2)
Geotherm evolution 50-40 Ma
P-T-t path 50-40 Ma
B
Depth (km)
Temperature (°C)
Pressure (kbar)
CBU/Zas
Koronos
Koronos
Koronos
Core
CBU M1
50 Ma
M2 20-15 Ma
M3
15 Ma
Ky
Sill
And
Thrust thickness = 30 km
D =10 km
V_Er = 0 km/Myr
T_base thrust = 500 °C
Geotherm evolution 40-15 Ma
P-T-t path 40-15 Ma
C
Thrust thickness = 30 km
D =10 km
V_Er = 0.5 km/Myr
CBU M1
50 Ma
M2
20-15 Ma
M3
~15 Ma
Geotherm evolution 15-5 Ma
P-T-t path 15-5 Ma
D
Thrust thickness = 30 km
D =10 km
Extension β= 2 & γ = 2
from 15-5 Ma
V_Er = 0.3 km/Myr
CBU M1
50 Ma
M2
20-15 Ma
M3
15 Ma

Table 1: Summary of Naxos Geochronology and Thermobarometry

Tectono-Stratigraphic Unit	Sample	GPS Lat/Long	Method and Dated Phase
Zas Unit	TLN54	N37.036781 E25.493024	U-(Th)-Pb Allanite U-(Th)-Pb Xenotime
Zas Unit	TLN26	N36.935434 E25.475521	U-(Th)-Pb Allanite U-(Th)-Pb Xenotime
Zas Unit	TLN30	N37.098329 E25.557419	U-(Th)-Pb Allanite
Literature Data			
Zas Unit	-	-	Rb-Sr White Mica, Ar-Ar and K-Ar
Koronos Unit	-	-	U-Pb Zircon and Rb-Sr
Core Unit	-	-	U-Pb Zircon
I-type Granodiorite	-	-	U-Pb Zircon
S-type Granites	-	-	U-Pb Zircon and Rb-Sr

Age (Ma)	2SE (Ma)	MSWD	Phases Present	Pressure (kbar)
50.35 21.70	5.16/5.47 0.59/1.31	0.88 0.73	Gln-Ph-Rt-Chl-Qz-Czo/Ep	14.5± 0.5 (M1) 12.6 ± 0.8 (M1)
40.52 30.61	2.30/2.72 0.39/0.52	2 1.4	Ph-Pg-Rt-Sph-Chl-Qz-Fsp	11.6 ± 2.2 (M1-M2) -
49.42	4.69/5.02	0.43	Czo/Ep-Qz-Ph-Ms-Bt-Sph-Chl-Cal	-

ca. 40.5-38.3 (M1 Rb-Sr); ca. 48-42 (M1 Ar-Ar/K-Ar); ca. 32-27 (M2)	Phg-Pg-Qz-Chl-Rt-Czo/Ep±Gln±Grt	15.5-19 (M1); >12 (M1); 3.5 (M2)
ca. 68-34 (? U-Pb), ca. 47-38 (M1/M2? U-Pb); ca. 28-15 (M2 Rb-Sr), ca. 18-14 (M2 U-Pb)	Grt-Ky-Bt-Ms-Pl-Qz-Rt-Ilm±Sill	8-11 (M2)
ca. 24-14 (M2/M3); ca. 20.7-16.8 (M2/M3)	Grt-Sill±Kfs±Ky-Bt-Ms-Pl-Qz-Rt-Ilm	5-10 (M2-M3)
ca. 12.2	Hb-Bt-Pl-Kfs-Qz-Sph	-
ca. 16-12.3 (U-Pb); ca. 14.3-11 (Rb-Sr)	Bt-Ms-Pl-Kfs-Qz±Grt±Turm	-

Temperature (C)	Thermobarometry Method
470 ± 30 (M1) 483 ± 12 (M1)	THERMOCALC Pseudosection, THERMOCALC AV-PT
483 ± 35 (M1-M2) -	THERMOCALC AV-PT -
-	-

570-590 (M1); 470 ± 50 (M1); 400 (M2)	THERMOCALC AV-PT
600-700 (M2)	THERMOCALC Pseudosection, AV-PT, GASP
690-730 (M2-M3)	THERMOCALC Pseudosection, AV-PT, GASP
-	-
-	-

Additional Notes	References
Deformed with S1 fabric, Peak M1 assemblage. Aln aligned with S1 fabric.	This Study; Lamont et al., 2019
Deformed by S2 and S3 fabrics, Aln aligned with retrograde M2 assemblage.	This Study; Lamont et al., 2019
Deformed by S3 fabrics and M2 assemblage that overprints relict M1 phases. Aln in cores of Czo.	This Study
Distinct tectonometamorphic cycle to structuraaly deeper units, limited M2 overprint.	Peillod et al., 2017; Peillod et al., 2021; Avigad, 1998
Prograde clockwise P-T loop through Ky field, followed by near isothermal decompression.	Martin et al., 2006; Keay et al., 2001; Bolhar et al., 2017; Lamont et al., 2019
Prograde clockwise P-T loop through Ky field and water saturated melting followed by near isothermal decompression through muscovite dehydration melting reaction to Sill field.	Keay et al., 2001; Vanderhaugue et al., 2018; Lamont et al., 2019
-	Keay et al., 2001
-	Keay et al., 2001; Lamont et al., (in review); Ring et al., 2018; (Vanderhaugue et al., 2018)